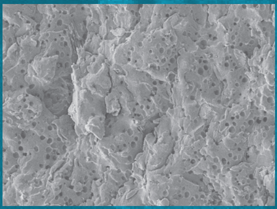

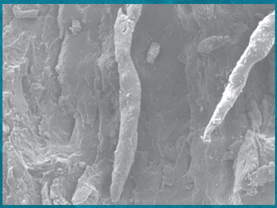

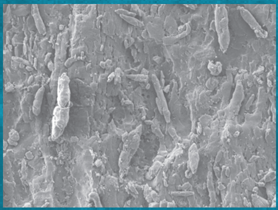

Mixed-Mode Fatigue Disbond on Metallic Bonded Joints

Daniel Bürger

Mixed-Mode Fatigue Disbond
on
Metallic Bonded Joints

Mixed-Mode Fatigue Disbond on Metallic Bonded Joints

Proefschrift

ter verkrijging van de graad van doctor
aan de Technische Universiteit Delft,
op gezag van de Rector Magnificus prof. ir. K.C.A.M. Luyben,
voorzitter van het College voor Promoties,
in het openbaar te verdedigen op vrijdag 25 februari 2015 om 15.00 uur

door

Daniel BÜRGER
Master of Science in Aeronautical Engineering
geboren te Brazilië

Dit proefschrift is goedgekeurd door de promotor:

Prof. dr. ir. R. Benedictus

Copromotor Dr. C. D. Rans

Samenstelling promotiecommissie:

Rector Magnificus,	Voorzitter
Prof. dr. ir. R. Benedictus,	Technische Universiteit Delft, promotor
Dr. C. D. Rans,	Technische Universiteit Delft, copromotor
Prof. M. P. Brandão,	Inst. Tecn. de Aeronáutica, Brazil
Prof. dr. W. Van Paepegem,	Ghent University, Belgium
Prof. dr. I.M. Richardson ,	Technische Universiteit Delft
Prof. dr. ir. R. Marissen,	Technische Universiteit Delft
Dipl.-Ing, T. Kruse,	Airbus Hamburg

ISBN: 978-94-6295-092-4

Keywords: disbond, damage tolerance, fatigue, mixed-mode

Cover Design by Proefschriftmaken.nl Uitgeverij BOXPress, ‘s-Hertogenbosch
Published by Uitgeverij BOXPress, ‘s-Hertogenbosch

Summary

“Mixed-Mode fatigue disbond on metallic bonded joints”

by Daniel Bürger

Aerospace structures have been long dealing with the safety versus weight issue. Lighter airplanes are cheaper to operate, however, they may face a safety issue because of the reduced fatigue life. Consequently, a heavier/safer structure is designed. Adhesive bonding is a joining technique that offers potential for improvement in the fatigue behavior of a structure, resulting in reduced weight. However, predicting the fatigue behavior of a bonded joint for its use in a damage tolerance design philosophy still remains a problem with no satisfactory solution. Often, the joint is subjected to a combination of peeling and shearing stresses. Hence, one of the most important factors influencing the fatigue behavior of an adhesively bonded joint is the Mode Ratio.

The objective of this investigation was to study of the Mode Ratio on the fatigue behavior of a bonded joint. First, the fatigue disbond mechanisms were investigated throughout the entire Mode Ratio range and compared to fatigue delamination mechanisms. After the mechanisms were identified, a parameter related to the mechanisms was chosen as similitude in the Paris relation and the Mixed-Mode fatigue disbond model was developed. Later, the model was evaluated on a different adhesive and on a condition of variable Mode Ratio.

The fatigue disbond mechanisms study identified the local principal stress as the driving force for the micro-crack formation and growth, and the Mode Ratio was identified as the controlling parameter for coalescence between the micro-cracks. Based on these findings, a parameter directly related to the principal stress was proposed as a similitude parameter. Additionally, a linear interpolation between Mode I and Mode II parameters of the Paris relation was proposed to predict the Mixed-Mode fatigue behavior. Thus, the model predicts the fatigue behavior for the entire Mode Ratio range using only pure Mode I and pure Mode II as inputs. The evaluation of this model revealed that it presents good predictions for Mode Ratios in the range of 0% to 50% and conservative predictions in the range of 50% to 100%. The model also seems to be valid in a variable Mode Ratio condition.

The limitations and shortcomings of the model along with the limitations of using a damage tolerance philosophy on adhesive bonding were discussed. Despite these issues, the model is an improvement over the models available in the literature because it captures some of the phenomena involved in the Mixed-Mode fatigue disbond. Additionally, the model also reduces the amount of empirical data required for its implementation.

Samenvatting

“Mixed-Mode vermoeiingsloslating van gelijmde metaalverbindingen”

door Daniel Bürger

Luchtvaartconstructies hebben al lang te maken met de kwestie veiligheid versus gewicht. Lichtere vliegtuigen zijn goedkoper in het gebruik, maar worden mogelijk geconfronteerd met veiligheidsproblemen door het verkorte vermoeiingsleven. Als gevolg wordt er een zwaardere / veiligere constructie ontworpen. Lijmen is een verbindingstechniek die potentieel een verbetering in het vermoeiingsgedrag van een constructie oplevert, resulterend in een lager gewicht. Echter, de voorspelling van het vermoeiingsgedrag van een gelijmde verbinding voor het gebruik in een schade tolerantie ontwerpfilosofie blijf een probleem zonder afdoende oplossing. Vaak is de verbinding onderhevig aan een combinatie van pel- en schuifspanningen. Aldus is één van de belangrijkste factoren die het vermoeiingsgedrag van een gelijmde verbinding bepalen de *mode ratio*.

Het doel van dit onderzoek is het bestuderen van het effect van de *mode ratio* op het vermoeiingsgedrag van een gelijmde verbinding. Eerst werden vermoeiingsloslatingsmechanismen onderzocht over het gehele *mode ratio* bereik, en vergeleken met vermoeiingsdelaminatiemechanismen. Nadat de mechanismen waren geïdentificeerd werd een parameter gerelateerd aan de mechanismen gekozen als gelijkheidsparameter in de Paris vergelijking, en werd het mixed-mode vermoeiingsloslatingsmodel ontwikkeld. Later werd het model geëvalueerd op een andere lijm en op de conditie van variabele *mode ratio*.

De studie naar de vermoeiingsloslatingsmechanismen identificeerde de lokale hoofdspanning als de drijvende kracht voor de microscheurformatie en groei en de *mode ratio* werd geïdentificeerd als de bepalende parameter voor samensmelting tussen de microscheuren. Gebaseerd op deze bevindingen werd een parameter direct gerelateerd aan de hoofdspanning gekozen als een gelijkheidsparameter. Daarnaast werd een lineaire interpolatie tussen de *mode* I en *mode* II parameters van de Paris vergelijking voorgesteld om het *mixed-mode* vermoeiingsgedrag te voorspellen. Aldus kan het model het vermoeiingsgedrag voorspellen voor het gehele *mode ratio* bereik, gebruikmakende van slechts puur *mode* I en puur *mode* II als invoer. De evaluatie van dit model toonde dat het goede voorspellingen levert voor *mode ratios* in het bereik van 0% tot 50% en conservatieve voorspellingen in het bereik van 50% tot 100%. Het model lijkt ook valide te zijn in het geval van variabele *mode ratio*.

De beperkingen en tekortkomingen van het model, alsook de beperkingen van het gebruik van een schade tolerantie filosofie voor gelijmde verbinden zijn besproken. Ondanks deze punten is het model een verbetering ten opzichte van de beschikbare modellen in de literatuur, omdat het een aantal van de fenomenen vangt die betrokken zijn bij *mixed-mode* vermoeiingsloslating. Bovendien vermindert het model de hoeveelheid empirische data die benodigd is voor de implementatie.

Contents

Nomenclature

Acronyms

4ENF	Four point End Notched Flexure
ADCB	Asymmetric Double Cantilever Beam
CA	Constant Amplitude
CAA	Chromic Acid Anodized
CGR	Crack Growth Rate
CLS	Cracked Lap Shear
CTS	Compact Tension Shear
DCB	Double Cantilever Beam
ELS	End-Loaded Split
ENF	End Notched Flexure
FCG	Fatigue Crack Growth
FDG	Fatigue Disbond Growth
FE	Finite Element
FEM	Finite Element Model
HS	Hart-Smith Model
MM	Mixed-Mode
MMB	Mixed-Mode Bending
MR	Mode Ratio
SEM	Scanning Electron Microscope
SERR	Strain Energy Release Rate
SLJ	Single Lap Joint
TDCB	Tapered Double Cantilever Beam
VA	Variable Amplitude
VCCT	Virtual Crack Closure Technique

List of Symbols

a	disbond length
A_1	slope of the plot a/t vs $C^{1/3}$
c	Paris relation coefficient
c’	log of the Paris relation coefficient

C	lever arm length
C_g	distance between lever arm center of gravity and the specimen center
Comp	compliance - δ/P
$\frac{da}{dN}$	disbond growth increment per cycle
e	error between the experimental observation and the prediction
E	adherend Young's modulus
f(x)	function to be fitted to experimental observations
G_I	Mode I SERR
G_{II}	Mode II SERR
G_{total}	total SERR
G_{max}	maximum SERR
G_{I-max}	maximum Mode I SERR
G_{I-min}	minimum Mode I SERR
G_{II-max}	maximum Mode II SERR
G_{II-min}	minimum Mode II SERR
L	half-span length
m	Paris relation exponent
MR	mode ratio - G_{II}/G_{total}
n	number of experimental points
P	load
P_g	lever arm weight
R	load ratio
Resi	Matrix with the residue (Eq. 3.29)
S	sum of the weighted squared errors (Eq. 3.4)
t	adherend thickness
X	matrix with the x_i (Eq. 3.15)
x_i	experimental observation x - variable
w	specimen width
w_i	weight relative to the ith experimental observation
Y	matrix with the y_i (Eq. 3.15)
y_i	experimental observation y - variable
Z	matrix with the partial derivatives $z_i(x_i)$ (Eq. 3.28)
$z_i(x)$	partial derivative of the function f(x) with respect to the β_i
β	estimated coefficient vector
$\hat{\beta}$	increment vector (Eq. 3.30)
β_i	ith estimated coefficient of the fitted function
ΔG	$G_{max} - G_{min}$
$\Delta\sqrt{G}$	$(\sqrt{G_{I-max}} - \sqrt{G_{I-min}})^2 + (\sqrt{G_{II-max}} - \sqrt{G_{II-min}})^2$
χ	disbond length correction parameter
$\Box^i$	variable $\Box$ at the ith iteration

List of Tables

List of Figures

1 Introduction

1.1 Fatigue Failure

Fatigue is a phenomenon where a single load far below the critical strength of a structure is responsible for a small amount of damage on the structure. The repetition of this load over a high number of cycles results in the complete failure of the structure due to damage accumulation [1]. The repeated loads (such as atmospheric turbulence, take off, landing, maneuvers, etc) acting on an aircraft makes its structure particularly susceptible to fatigue failures. Therefore, fatigue failures are a major concern of aerospace structural engineers, specially because of the disastrous consequences of a structural failure, such as the loss of the aircraft and, eventually, the loss of lives.

Fatigue failures on aircrafts may be prevented using three design philosophies: safe life, fail safe and damage tolerance. In the safe life philosophy, a part is designed to avoid the development of fatigue failures during its planned life. Afterwards, the part should be replaced. The fail safe philosophy demands that after the appearance of a crack the remaining structure must be able the retain the required residual strength until the repair of the structure, i.e., a part may fail but the structure will still withstand the loads. The damage tolerance philosophy supposes a damage in the material and calculates inspections intervals to replace the part before the damage grows to a critical size.

Until the 1950's aircrafts were designed using the safe life philosophy. However, using this design the aircraft parts must be replaced after the designed life, disregarding the condition of the part. With the increasing prices of aircrafts, this design philosophy has proved expensive. In the late 1970's the concept of damage tolerance was introduced. It allows for a longer use of the parts if coupled with inspections to assure the structural integrity of the part. Currently, the damage tolerance philosophy is preferred, unless inspections are not possible or if the crack can grow to a critical size in a short interval. In such cases, the safe life or the fail safe philosophy are applied.

Fatigue failures are known to initiate at material defects (porosity, inclusions, etc) or at structural discontinuities, where the defect or discontinuity is responsible for a stress concentration effect. Material defects can, if larger than a certain size, be avoided through quality inspection techniques. However, discontinuities are common in the structure as they are used to join elements, save weight and optimize the structure. Thus, the discontinuities on structures are considered potential areas for failures and demand higher attention on design and maintenance.

One of the most fatigue dangerous type of discontinuity on a structure is the one encountered on joints. Usually, two elements are connected through a mechanical fastener (rivet or bolt) and this region presents a high stress concentration effect and it can severely reduce the fatigue life of the structure.

1.2 Joining Techniques

Currently, the most common joining technique used to connect metallic elements on an aircraft structure is mechanical fasteners. There are alternatives, such as adhesive bonding or welding. However, on aircraft primary structures, the majority of the elements are connected with mechanical fasteners [2].

The use of adhesive bonding can present a good alternative to mechanical fasteners. The absence of notches and the larger area the load is transfered from one element to another reduces significantly the stress concentration on the joint. Consequently, adhesively bonded joints can present a better fatigue behavior (Fig. 1.1).

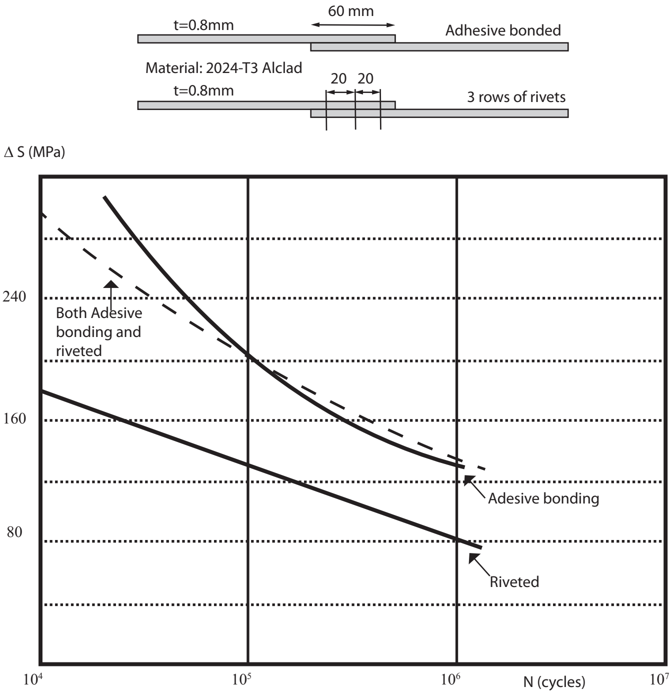

Figure 1.1: *Comparison between the S-N curves (R=0.1) of a riveted, bonded and riveted and bonded joint for similar geometries. Adapted from [3], cited by [1].*

1.2.1 Adhesive bonding limitations

The use of adhesive bonding in metallic primary aircraft structures is still limited. The limitations come partially from the lack of confidence in the long term behavior of adhesive bonding and, as consequence, partially from safety regulations.

Safety regulations do not cite explicitly adhesive bonding on metallic parts [4]. However, they do cite adhesive bonding on composite parts (FAR 23.573 (a)(5) and Advisory Circular 20 - 107B - FAA). On this item, the strength of a bonded composite primary structure must be assured by (i) the maximum disbond length must be limited by design features, (ii) proof testing each article, or (iii) repeated and reliable non-destructive inspection techniques must be establish to ensure the joint strength.

The first option proposed would result in the use of mechanical fasteners and, for design and inspection purposes, the advantages of the bonding process are partially ignored. For High Load Transfer Joitns, the joint is designed and inspected as if there is no adhesive bonding. Aircraft manufactures usually adopt this solution (commonly known as chicken rivets) and benefit from structures with a smoother load path. However the benefit is limited as the structure is designed and the inspections intervals are determined disregarding the adhesive bonding. For Low Load Transfer Joints, the bondline is taken into account on the structural calculation, and the mechanical fasteners are used to limit accidental weak bonds.

The second option is impractical as it would require the test of every joint manufactured. Last, the third option is the one needed for a damage tolerance design for bonded joints. Up to date, there is no reliable inspection technique that can assure the strength of a bonded joint. There are advances in the field, specially using ultrasonic scan, acoustic emission, infrared thermography, etc. However, the detection of weak bonds still poses as one of the main challenges for the development of a reliable inspection technique. Additionally to inspection techniques, the damage tolerance design requires reliable disbond growth prediction models to determine inspection intervals. This thesis will focus only on the development of a reliable disbond growth model.

The failure on a bonded joint usually occurs as a consequence of both Mode I (peeling) and Mode II (sliding shear) loads (Fig. 1.2). Mode III (tearing shear) usually does not happen on joints. The literature present several models attempting to predict the failure under a combination of Mode I and Mode II - denoted as Mixed-Mode (MM) - fatigue loads [5]. However, there are still severe limitations to the models available and the most successful ones, adapted from MM delamination [6, 7], are models that fit experimental data without any input from the failure mechanisms observed. Therefore, the use of a damage tolerance design on metallic bonded joints requires the development of a robust disbond growth prediction model substantiated by failure mechanisms.

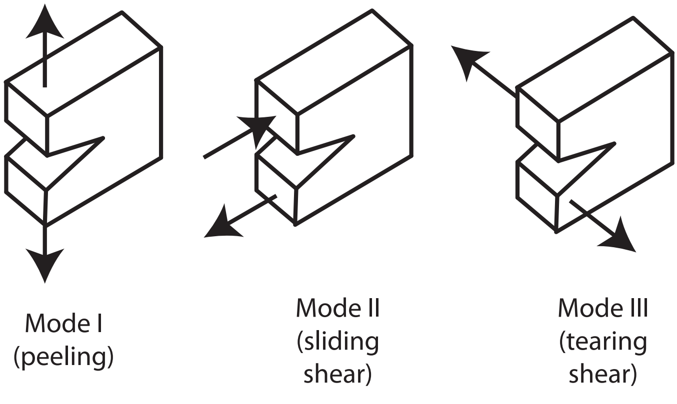

Figure 1.2: *Crack opening modes.*

1.3 Project Scope

Adhesive bonding has long been considered a potential candidate to substitute mechanical fasteners on aircraft structural metallic joints due to its better fatigue behavior. However, the lack of robust prediction models capable of predicting the Mixed-Mode fatigue disbond poses still as one of the obstacles that must be overcome before the widespread use of adhesive bonding for primary structures. Currently, the best MM disbond are based just on fitting experimental data, and the literature does not present any robust model based on the failure mechanisms. As a result,

> The research main objective is to develop a damage tolerance model based on the failure mechanisms to predict Mixed-Mode disbond in a metallic bonded joint.

In order to achieve the research goal, the following steps will be taken:

1. Review about adhesive failure, focusing on MM fatigue loading (Chapter 2).
2. Carry out an experimental study (Chapter 3) to produce a MM fatigue disbond data set and to produce fracture surfaces for posterior failure mechanism investigation.
3. Analyze the fracture surfaces to identify the MM failure mechanisms and how they develop at different mode ratios (chapter 4).
4. Develop a damage tolerance model based on the failure mechanisms observed in the previous Chapter (chapter 5).
5. Evaluate the model on the data set produced and on data sets obtained in the literature and discuss the implications of the model assumptions (chapter 5).

After the model is developed, it will be evaluated in a joint specimen with a variable Mode Ratio, in Chapter 6. And, the final conclusions of this work are presented in Chapter 7.

References

[1] J. Schijve. *Fatigue of Structures and Materials.* Kluwer Academic, Dordrecht, Boston, 2004.

[2] A. Higgins. Adhesive bonding of aircraft structures. *International Journal of Adhesion & Adhesives*, 20:367–376, 2000.

[3] A. Hartman and Nationaal Lucht en Ruimtevaartlaboratorium. *Fatigue Tests on Single Lap Joints in Clad 2024 T3 Aluminium Alloy Manufactured by a Combination of Riveting and Adhesive Bonding.* NTIS, 1966.

[4] J.S. Tomblin, United States. Federal Aviation Administration. Office of Aviation Research, National Institute for Aviation Research (U.S.), and William J. Hughes Technical Center (U.S.). *Assessment of Industry Practices for Aircraft Bonded Joints and Structures.* DOT/FAA/AR. U.S. Department of Transportation, Federal Aviation Administration, Office of Aviation Research, 2005.

[5] J. A. Pascoe, R. C. Alderliesten, and R. Benedictus. Methods for the prediction of fatigue delamination growth in composites and adhesive bonds - A critical review. *Engineering Fracture Mechanics*, 112-113:72–96, 2013.

[6] M. Kenane and M.L. Benzeggagh. Mixed-mode delamination fracture toughness of unidirectional glass/epoxy composites under fatigue loading. *Composites Science and Technology*, 57(5):597–605, 1997.

[7] N. Blanco, E.K. Gamstedt, L.E. Asp, and J. Costa. Mixed-mode delamination growth in carbon-fibre composite laminates under cyclic loading. *International Journal of Solids and Structures*, 41(15):4219–4235, 2004.

2 Literature Review

2.1 Introduction

Adhesive bonding has long been considered a potential substitute for mechanical fasteners on aircraft structural joints [1]. The main advantages of adhesive bonding are usually: reduced weight, higher fatigue resistance, sealing capabilities, reduced manufacturing costs [2], and, for dissimilar adherents, it avoids galvanic corrosion [3] and it can reduce thermal stresses [4]. However, the lack of confidence in the long term response of the adhesive joint still poses limitations to a wider use of adhesive bonding on aircraft structural joints [5].

2.1.1 Adhesive Joints: life time prediction

Several factors are known to affect the behavior of an adhesive joint over its life time: manufacturing defects (air entrapment, poor adhesion, poor surface preparation), environment (temperature, humidity, chemicals), and loading conditions (mode ratio, static or fatigue, variable amplitude and stress ratio among others). Coupled with the aforementioned factors is the adhesive itself, as different adhesives can behave differently for each of the factors.

Manufacturing defects can, to some extent, be prevented using processes and quality control. However, loading and environment conditions are application requirements and must be fullfilled. Therefore, the effect of these conditions on the adhesive failure is the subject of several studies.

Environmental effects

Environmental conditions affect the failure by changing the adhesive properties or by modifying the adhesive/adherend interface, usually reducing the adhesive service life.

The temperature affects bonded joint in two different ways: thermal stresses and property change. The thermal stresses arise from different thermal expansion coefficients and they can diminish the failure load of the bond line [6]. However, the most relevant effect comes from the change in the mechanical properties. This effect is deeply connected with the ductility/brittleness of the adhesive. Usually at a lower temperature the adhesive becomes more brittle and more stiff [7] and at a higher temperature it becomes more ductile and less stiff [7]. As a result, brittle adhesives are more sensitive to defects at low temperatures and ductile adhesives have a significant reduction in their properties at higher temperatures [4, 7, 8].

Another important environmental condition to be observed is the presence of water. Water can affect the failure of adhesive joints in two different ways: deterioration of the bulk adhesive and degradation of the interface [6]. The bulk properties are affected because of plasticization [9–11], swelling [12, 13], and degradation [11, 14, 15] of the adhesive. The adhesive/adherend interface is affected as it is usually the faster way of water to diffuse into the adhesive [4, 8]. Thus, the fracture has a higher chance to develop on the interface [15, 16].

Last, the remaining environmental conditions are combined into a subject usually referred to as chemical resistance and it deals with the adhesive response to several fluids and liquids the adhesive may be in contact with [6]. The most important fluids in the aerospace industry includes aviation fuel and its additives, de-icing and hydraulic fluid. Structural epoxies can present a small loss in mechanical properties when exposed to pure aviation fuel [17] but some of the fuel additives may degrade the adhesive reducing its durability [17]. Hydraulic fluid has behavior similar to fuel [18], because of their chemical similarities. The adhesive failure properties are affected by both fuel and hydraulic fluid due to swelling and plasticization of the adhesive [18]. De-icing fluid reduces the service life of an adhesive by a similar mechanism but the reduction is smaller [18].

One must remember, however, that a different combination of adhesive/chemical can result in different behavior. Additionally, the combination of chemicals with temperature, high stress levels, water or other chemicals can accelerate the degradation mechanisms due to environmental conditions [6]. As a result, before its use, the adhesive must be tested in conditions similar to the service life.

Loading effects

Similarly to environmental conditions, the loading conditions are project requirements and they must be fullfilled. In adhesives, if the load is higher than a certain level, the failure process starts with the nucleation of micro-voids ahead of the crack tip to accommodate the local stresses [19, 20]. Afterwards, with a increasing load, they grow and coalesce forming a crack. Under fatigue loading, the main parameters affecting the failure are the stress ratio ($R = \sigma_{min}/\sigma_{max}$), the Mode Ratio ($MR = G_{II}/G_{total}$, where G refers to the Strain Energy Release Rate - SERR) and the load spectra (constant or variable amplitude).

The effect of R for adhesive bonding depends on the parameter chosen to represent the load. In metals, the parameter usually adopted is the stress intensity factor range, which is proportional to the stress amplitude ($\sigma_{max} - \sigma_{min}$). If this parameter is kept constant, an increase in R will result in a decrease in the fatigue life. However, the parameters most used to represent disbond grow are G_{max} and $G_{max} - G_{min}$, which are not linearly related to the stress amplitude. The results may seem counter-intuitive [21], i.e., an increase in R will result in an increase in the fatigue life. However, if the data is represented with a paramenter similar to stress amplitude is used, the results are similar to metals [16, 21].

The load spectra refers to the loads the structure will experience in service [22]. For design purposes, the fatigue damage is obtained in a Constant Amplitude (CA) test and later adapted with a Variable Amplitude (VA) theory, also supported by experiments. The Miner-rule is the most common theory to adapt a VA spectrum in CA results. The Miner-rule adds the contribution of each cycle ignoring any interaction between them [22]. Based on this rule, a material is said to present damage acceleration or retardation if the failure occurs faster or slower. Adhesives are reported to present damage acceleration in VA spectrum [23–26]. The mechanism proposed for this acceleration is that an overload induces more damage over an larger area ahead of the crack tip. As a result, the next cycles will load a weaker material and, thus, produce a larger damage in comparison with CA load [24].

The MR refers to the deformation mode the load imposes to the adhesive. The deformation modes are peeling (Mode I), sliding shear (Mode II) and tearing shear (Mode III). In adhesive joints Mode III load is minimal and it can be ignored [27]. Due to the adhesive lower resistance to Mode I loading, joint design attempts to minimize the Mode I component and load the adhesive mainly in Mode II. However, a Mode I component can be observed in most joints. This results in a Mixed-Mode (MM) condition for most of joint configurations. Additionally, as the failure process starts and evolves, the loading conditions over the adhesive can change resulting in a variable MR during the failure process. The literature presents few MM disbond models. However, due to the similarity in the failure mechanisms [28], composite delamination models are often used to predict disbond (e.g. [29–31]). Thus, the next section will present an overview of the models for disbond and for delamination available in the literature.

2.2 Mixed-Mode models overview

In 2004, Blanco *et al* [32, 33] did a literature review about MM delamination where they evaluated MM delamination models [34–41] using MM data available in the literature [42, 43]. From the models evaluated, the only one using only pure Mode I and Pure mode II fatigue crack growth data was proposed by Gustafson and Hojo [35] but it had a poor agreement with the experimental results [33] and its predictions were consistently non-conservative. The best predictions were obtained by Kardomateas *et al* [38] and Kenane and Benzeggagh [39].

Gustafson and Hojo [35] proposed a model where Mode I and Mode II would contribute independently to the total crack growth (Eq. 2.1). The model was evaluated on unidirectional T300/914 Carbon Graphite/epoxy laminates. Mode I coefficients were obtained using Double Cantilever Beam (DCB) and Mode II coefficients were obtained through regression on a Cracked Lap Shear (CLS). The MR on the CLS specimen varied in the range of 69% to 73%. Later, the authors highlighted the importance of further tests covering a larger MR range to support the use of Eq. 2.1.

$$\frac{da}{dN} = C_I.(\Delta G_I)^{m_I} + C_{II}.(\Delta G_{II})^{m_{II}} \tag{2.1}$$

Kardomateas *et al* [38] proposed a model to predict delamination under buckling. In the model, the values of SERR were normalized by the fracture toughness (Eq. 2.2). As G_c values may not be available for all MR, the authors suggested the model proposed by Hutchinson and Suo [44] (Eq. 2.3) to determine it.

$$\tilde{G} = \frac{G}{G_c} \tag{2.2}$$

$$G_c(MR) = \frac{G_{Ic}}{1 + (\lambda - 1).MR} \qquad\qquad \lambda = \frac{G_{Ic}}{G_{IIc}} \tag{2.3}$$

Thereafter, the MM is accounted for with a linear variation of the coefficients C and m in the Paris relation (Eq. 2.4 and 2.5).

$$C(MR) = C_I + (C_{II} - C_I).MR \tag{2.4}$$

$$m(MR) = m_I + (m_{II} - m_I).MR \tag{2.5}$$

The crack growth rate is obtained with:

$$\frac{da}{dN} = C(MR).\frac{\Delta\tilde{G}^{m(MR)}}{1 - \tilde{G}_{max}} \tag{2.6}$$

The model was evaluated on graphite-epoxy (T50 6k ERL 1939-3) and the buckling configurations resulted in MR from 63% to 100% (pure Mode II). The authors compared the number of cycles to failure and the results showed good agreement with the experiments.

Kenane and Benzeggagh [39] developed a semi-empirical criterion to predict C and m in the Paris relation for different MR. The criterion is based on a power law and assumes the form:

$$m = m_I + (m_{II} - m_I)\left(\frac{G_{II}}{G_{Total}}\right)^{m_m} \tag{2.7}$$

$$ln(C) = ln(C_{II}) + [ln(C_I) - ln(C_{II})]\left(1 - \frac{G_{II}}{G_{Total}}\right)^{m_C} \tag{2.8}$$

Later, the crack growth rate is obtained using:

$$\frac{da}{dN} = C.\Delta G^m \tag{2.9}$$

The authors had a complete set of MM data, with a total of eight MR to evaluate the model. They performed the tests on quasi-unidirectional E-glass fiber/epoxy and used the DCB test for Mode I, the End-Loaded Split (ELS) for Mode II and the Mixed-Mode Bending (MMB) test for MM. Instead of evaluating the crack growth rate, the authors evaluated the predictions for C and m and the model obtained good agreement with the experimental values. Despite the good agreement of Kenane and Benzeggagh model with experiments [32, 39], the imposition of a monotonic variation to the Paris relation coefficients is a major shortcoming of this model.

After evaluating the MM models, Blanco *et al* [32, 33] proposed a non-monotonic model, using a quadratic function, to predict the MM behavior (Eq. 2.10, 2.11 and 2.12).

$$m(MR) = m_1 + m_2.MR + m_3.MR^2 \tag{2.10}$$

$$Log(C(MR)) = c_1 + c_2.MR + c_3.MR^2 \tag{2.11}$$

$$\frac{da}{dN} = C(MR).(\Delta G)^{m(MR)} \tag{2.12}$$

The authors evaluated the model with data from the literature [42] with good agreement with experiments. Later, the authors evaluated the model in a condition of variable MR with poor agreement between the predictions and the experimental data [33].

After the review of Blanco *et al* [32, 33], some models were proposed to predict MM fatigue failure [45–48].

Cheuk *et al* [45] proposed a model where an equivalent SERR range would be used. The ΔG_{eq} is defined in eq. 2.13. The authors evaluated the model with in a composite to metal double lap joint specimen using the adhesive FM-73 to bond boron/epoxy to aluminum. Only two MR were compared (MR=0% and MR=87%) but the use of ΔG_{eq} improved the predictions.

$$\Delta G_{eq} = \Delta G_I + \frac{G_{Ic}}{G_{IIc}} \Delta G_{II} \tag{2.13}$$

Similarly to Cheuk *et al*, Quaresimin and Ricotta [46] also proposed the use of an equivalent SERR (Eq. 2.14), after applied to the Paris relation (Eq. 2.15). The model was evaluated on Single Lap Joints (SLJ) [49] composed of Carbon/epoxy adherends (Seal Texipreg ® CC206, T300 twill 2 x 2 carbon fiber fabric/ET442 toughened epoxy matrix) bonded with a two-part epoxy adhesive (9323B/A - 3M) [50]. The SLJ were manufactured with three different overlap lengths and two different corner geometries. Using the G_{eq} the authors successfully collapsed the Crack Growth Rate (CGR) data of the different specimens (different overlap length and different corner geometries).

$$G_{eq} = G_I + MR.G_{II} \tag{2.14}$$

$$\frac{da}{dN} = C.(\Delta G_{eq})^m \tag{2.15}$$

Carraro *et al* [47] also proposed a model based on an equivalent G. The authors observed that in a plot of constant CGR in the $\Delta G_I - \Delta G_{II}$ plane, a set of constant CGR data could be fitted with two straight lines (Fig. 2.1).

Thus, G_{eq} can be defined as:

$$\begin{cases} MR < 50\% \rightarrow \Delta G_{eq} = \Delta G_I \\ MR > 50\% \rightarrow \Delta G_{eq} = \dfrac{1}{s+1}(s.\Delta G_I + \Delta G_{II}) \end{cases} \tag{2.16}$$

Where s is the slope of the constant CGR line defined in Fig. 2.1. The authors assume s to be independent of the CGR. As a result, the model assumes the exponents of the Paris relation for Pure Mode I and Pure Mode II to be equal.

$$s = \frac{\Delta G_{II,CGR}}{\Delta G_{I,CGR}} - 1 \tag{2.17}$$

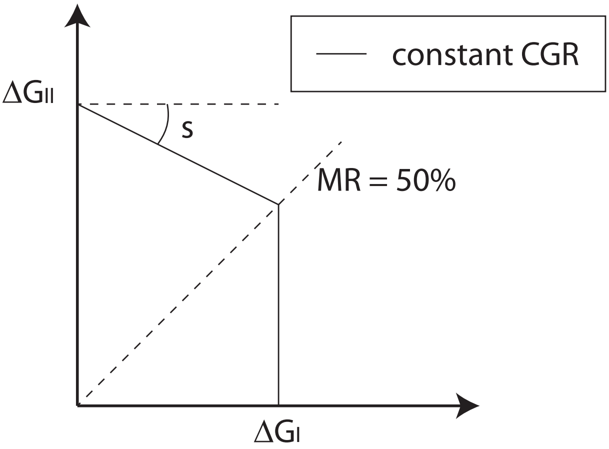

Figure 2.1: *Bi-linear model proposed by Carraro et al [47].*

$$\left.\frac{da}{dN}\right)_{ModeI} = \left.\frac{da}{dN}\right)_{ModeII} \tag{2.18}$$

$$C_I.(\Delta G_{I,CGR})^{m_I} = C_{II}.(\Delta G_{II,CGR})^{m_{II}} \tag{2.19}$$

$$\frac{(\Delta G_{II,CGR})^{m_{II}}}{(\Delta G_{I,CGR})^{m_I}} = \frac{C_I}{C_{II}} \tag{2.20}$$

assuming $m_I = m_{II} = m$:

$$\frac{\Delta G_{II}}{\Delta G_I} = \left(\frac{C_I}{C_{II}}\right)^{1/m} \tag{2.21}$$

Applying Eq. 2.21 in 2.17:

$$s = \left(\frac{C_I}{C_{II}}\right)^{1/m} - 1 \tag{2.22}$$

The authors evaluated the model using carbon/epoxy adherends (Seal Texi-preg ® CC206, T300 twill 2 x 2 carbon fiber fabric/ET442 toughened epoxy matrix) bonded with a two-part epoxy adhesive (9323B/A - 3M). The specimens produced were tested using the DCB test for pure Mode I, End Notch Flexure (ENF) test for pure Mode II, and MMB for MM. For MM, the authors evaluated four MR (MR=15%, 36%, 52% and 75%). Using the G_{eq} defined in Eq. 2.16 the authors obtained a collapse in the CGR for all the MR evaluated.

Later, the authors modified the model to include a parameter related to the principal stress in the process zone (S) [48]. The authors observed a change in the failure mechanisms. If Mode I load dominates, the failure occurs at the interface. Alternatively, if the Mode II dominates, the failure occurs within the adhesive as a consequence of the principal stress. Therefore, they postulated that the driving force of fatigue crack propagation is:

$$\begin{cases} MR < MR^* \rightarrow G_I \\ MR > MR^* \rightarrow S \end{cases} \tag{2.23}$$

Where S is defined as the average of the principal stress in the process zone. The process zone is defined as a rectangle ahead of the crack tip with dimensions of $t_{adhesive}$ by $3.t_{adhesive}$. The authors obtained the parameter S through FE simulations. They observed that S is linearly related to $\sqrt{G_{total}}$ and it also depends on the MR (Eq. 2.24). Observing the fracture mechanisms, the authors defined MR^* as 50%, similarly to the their previous model.

$$S = k(MR).\sqrt{G_{total}} \tag{2.24}$$

Later, the authors obtained a parameter equivalent to S written in terms or SERR. Thus, the final model can be describe as:

$$\begin{cases} MR < 50\% \rightarrow \Delta G_{eq} = \Delta G_I \\ MR > 50\% \rightarrow \Delta G_{eq} = (\Delta G_I + \Delta G_{II}) \left[\dfrac{k(MR)}{k(100\%)} \right]^2 \end{cases} \tag{2.25}$$

This second model was evaluated with data available in the literature [47, 49] and it successfully collapses the data from different MR.

2.3 Models Discussion

In the models listed in the previous section, only the model proposed by Carraro *et al* [48] attempts to introduce a parameter directly related to the failure mechanisms: the parameter S (Eq. 2.24), related to the principal stress in the process zone. However, this parameter is used to describe FCG only for MR higher than 50%. Additionally, one can not obtain the parameter S analytically, for it requires the use of FE simulations.

The majority of the models ignored the failure mechanisms and proposed an equation based on data analysis to describe the MM FCG. The complexity of the failure mechanisms [32, 51–54] is the reason why models ignore them.

2.3.1 Paris relation coefficients dependence

Kenane and Benzeggagh adopted a power law to describe the Paris relation coefficients as a function of MR and, as such, it presents a monotonic behavior. However, Blanco *et al* [32] presented data which requires the function to be non-monotonic. Blanco *et al* solved this issue by using a quadratic function. However, both models neglect the strong dependence between the Paris coefficients and the scatter commonly present in FCG curves which can be part of the reason for coefficients non-monotonic behavior.

As an example, Hafiz *et al* presented MM disbond data for 5 MRs (0%, 18%, 42%, 56% and 87%). According to the authors, the Paris relation exponent varied non-monotonically between 2 and 7 (see Fig. 2.2). However, observing the FCG curves for the different MRs one can not see such difference in the slope of the points (see Fig. 2.3). This indicates that the curve fitting methodology used to obtain the Paris relation coefficients may have an influence on the result, likely enhancing the non-monotonic behavior. A similar behavior can be seen in Blanco *et al* [32], where the FCG data [43] presents similar slopes but the values differ considerably ($m_{0\%} = 5.1$, $m_{50\%} = 6.3$ and $m_{100\%} = 4.4$).

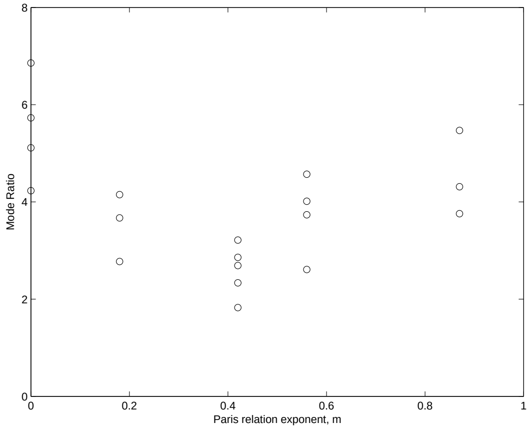

Figure 2.2: *Variation of fatigue crack propagation exponent for FM73 adhesive under different Mode mixities evaluated by Hafiz et al [31].*

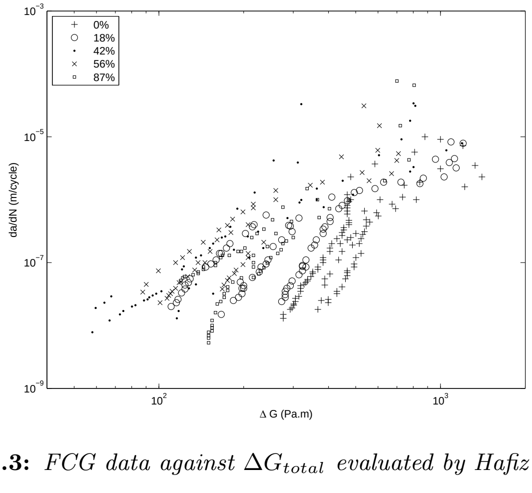

Figure 2.3: *FCG data against ΔG_{total} evaluated by Hafiz et al [31].*

2.3.2 Simultaneously disbond and delamination

As presented in the previous section, most MM fatigue models were developed for MM composite delamination and only a few were developed for MM disbond [45–48]. However, the models were evaluated only on composite materials, where the crack can occur on the bond line or on the adherend itself as delamination. Some researchers have reported delamination on the layers close to the bond line and difficulties to obtain only disbond [47, 55].

Most authors considered the failure as either delamination or disbond, disregarding the differences between both. Cheuk *et al* [45] bonded boron/epoxy to aluminum and they reported the crack growing in the epoxy region and not in the adhesive. The typical fracture surface presented a mix between bare fibers, indicating poor fiber/matrix adhesion, and matrix. Quaresimin and Ricotta [50] reported the crack eventually oscillating between the adhesive/adherend interface and the adherend first layer.

Carraro *et al* [47, 48] reported delamination growing parallel to the disbond and they considered the crack tip as the farthest from the disbond and the delamination tip. The authors disregard the measurements for the CGR if the delamination and the disbond occurred simultaneously. However, they did include delamination measurements when the crack moved from the interface (disbond) to the adherend (delamination) on resin rich areas. In addition, the authors used a compliance model [56] and corrected it with FE simulations to obtain the SERR. However, they did not include the additional cracks in the adherends in the FE simulations.

2.3.3 Data analysis problems

Currently, the most used models are Kenane and Benzeggagh [39] and Blanco *et al* [32]. Both models assume the Paris relation coefficients follow a particular function with the MR and fit the coefficients to this function. Both models require tests at least three different MRs, so the function coefficients can be determined.

However, the authors of both models use more than three MRs in the model evaluation (Kenane and Benzeggagh used 8 MRs and Blanco *et al* used 6 MRs). As both models fit are fitting models, one would expect that the more inputs in the model, the better they predict. Hence, the good predictions presented by both models.

However, if less points are used to fit the function, the accuracy of the function to describe the phenomenon becomes more important. When Blanco's *et al* model was evaluated using only three MRs inputs in a condition of variable MR [33], the agreement between the predictions and the experimental data was poor. This indicates the quadratic function proposed may not be the best solution.

2.4 Conclusion

Adhesive bonding has the potential to replace mechanical fasteners on the aircraft joints but the industry still does not have a robust model to predict disbond under fatigue loading. This chapter presented an overview of MM fatigue delamination/disbond models. It also discussed the problems associate with the models development and evaluation.

The main problems observed on the models' development were the lack of physical basis of the models and the strong dependency on the Paris relation coefficients, which is ignored by the models. Additionally, the models were evaluated on composite materials with reports of delamination growing parallel to the disbond and/or the failure oscillating between the bond line and the composite matrix.

References

[1] Willard D. Bascom and Robert L. Cottington. Air entrapment in the use of structural adhesive films. *The Journal of Adhesion*, 4(3):193–209, 1972.

[2] W.S. Johnson, L.M. Butkus, and R.V. Valentin. Applications of fracture mechanics to the durability of bonded composite joints. Technical report, U.S. Department of Transportation - Federal Aviation Administration, 1998.

[3] E. Lertora, C. Gambaro, C. Mandolfino, and M. Pedemonte. Environmental effects on methacrylate adhesive. *Welding International*, 28(5):372–379, 2014.

[4] A. Baldan. Review adhesively-bonded joints in metallic alloys, polymers and composite materials: Mechanical and environmental durability performance. *Journal of Materials Science*, 39(15):4729–4797, 2004.

[5] D. A. Jablonski. Fatigue crack growth in structural adhesives. *Journal of Adhesion*, 11(2):125–143, 1980.

[6] D. Dillard. *Advances in Structural Adhesive Bonding*. Woodhead Publishing Series in Welding and Other Joining Technologies. Elsevier Science, 2010.

[7] L. F. M. da Silva and R. D. Adams. Joint strength predictions for adhesive joints to be used over a wide temperature range. *International Journal of Adhesion and Adhesives*, 27(5):362–379, 2007.

[8] A. C. Garg. Interlaminar and intralaminar fracture surface morphology in graphite/epoxy laminates. *Engineering Fracture Mechanics*, 23(6):1031–1050, 1986.

[9] M. R. Bowditch. The durability of adhesive joints in the presence of water. *International Journal of Adhesion and Adhesives*, 16(2):73–79, 1996.

[10] N. Su, R. I. Mackie, and W. J. Harvey. The effects of ageing and environment on the fatigue life of adhesive joints. *International Journal of Adhesion and Adhesives*, 12(2):85–93, 1992.

[11] J. W. Wylde and J. K. Spelt. Measurement of adhesive joint fracture properties as a function of environmental degradation. *International Journal of Adhesion and Adhesives*, 18(4):237–246, 1998.

[12] J. P. Sargent and K. H. G. Ashbee. On the occurrence of osmosis during water uptake by adhesively bonded titanium joints. *Journal of Physics D: Applied Physics*, 14(10):1933–1938, 1981.

[13] K. T. Tan, C. C. White, D. L. Hunston, C. Clerici, K. L. Steffens, J. Goldman, and B. D. Vogt. Fundamentals of adhesion failure for a model adhesive (PMMA/Glass) joint in humid environments. *Journal of Adhesion*, 84(4):339–367, 2008.

[14] G. Z. Xiao and M. E. R. Shanahan. Water absorption and desorption in an epoxy resin with degradation. *Journal of Polymer Science, Part B: Polymer Physics*, 35(16):2659–2670, 1997.

[15] W. K. Loh, A. D. Crocombe, M. M. A. Wahab, J. F. Watts, and I. A. Ashcroft. The effect of moisture on the failure locus and fracture energy of an epoxy-steel interface. *Journal of Adhesion Science and Technology*, 16(11):1407–1429, 2002.

[16] M. Hojo, K. Tanaka, C.G.Gustafson, and R. Hayashi. Fracture mechanics for delamination fatigue crack propagation of crfp in air and in water. *Key Engineering Materials*, 37:149–160, 1989.

[17] A. Rider, E. Yeo, Defence Science, and Technology Organisation (Australia). Platforms Sciences Laboratory. The chemical resistance of epoxy adhesive joints exposed to aviation fuel and its additives. Technical report, 2005.

[18] G. Doyle and R. A. Pethrick. Environmental effects on the ageing of epoxy adhesive joints. *International Journal of Adhesion and Adhesives*, 29(1):77–90, 2009.

[19] R. A. Kline and F. H. Chang. Composite failure surface analysis. *Journal of Composite Materials*, 14:315–324, 1980.

[20] S. Singh and E. Greenhalgh. Micromechanics of interlaminar fracture in carbon fibre reinforced plastics at multidirectional ply interfaces under static and cyclic loading. *Plastics, Rubber and Composites Processing and Applications*, 27(5):220–226, 1998.

[21] C.D. Rans, R. Alderliesten, and R. Benedictus. Misinterpreting the results: How similitude can improve our understanding of fatigue delamination growth. *Composites Science and Technology*, 71(2):230–238, 2011.

[22] J. Schijve. *Fatigue of Structures and Materials.* Kluwer Academic, Dordrecht, Boston, 2004.

[23] I.A. Ashcroft. A simple model to predict crack growth in bonded joints and laminates under variable-amplitude fatigue. *Journal of Strain Analysis of Engineering Design*, 39(6):707–716, 2004.

[24] E.A. Nolting, P.R. Underhill, and D.L. DuQuesnay. Variable amplitude fatigue of bonded aluminum joints. *International Journal of Fatigue*, 30(1):178–187, 2008.

[25] V. Shenoy, I.A. Ashcroft, G.W. Critchlow, A.D. Crocombe, and M.M. Abdel Wahab. An evaluation of strength wearout models for the lifetime prediction of adhesive joints subjected to varible amplitude fatigue. *International Journal of Adhesion & Adhesives*, 29(6):639–649, 2009.

[26] V. Shenoy, I.A. Ashcroft, G.W. Critchlow, and A.D. Crocombe. Fracture mechanics and damage mechanics based fatigue lifetime prediction of adhesively bonded joints subjected to variable amplitude fatigue. *Engineering Fracture Mechanics*, 77(7):1073–1090, 2010.

[27] S. K. Panigrahi and B. Pradhan. Three dimensional failure analysis and damage propagation behavior of adhesively bonded single lap joint in laminate FRP composites. *Journal of Reinforced Plastics and Composites*, 26(2):183–201, 2007.

[28] J. A. Pascoe, R. C. Alderliesten, and R. Benedictus. Methods for the prediction of fatigue delamination growth in composites and adhesive bonds - A critical review. *Engineering Fracture Mechanics*, 112-113:72–96, 2013.

[29] M. M. Abdel Wahab, I. A. Ashcroft, A. D. Crocombe, and P. A. Smith. Numerical prediction of fatigue crack propagation lifetime in adhesively bonded structures. *International Journal of Fatigue*, 24(6):705–709, 2002.

[30] H. Khoramishad, A. D. Crocombe, K. B. Katnam, and I. A. Ashcroft. Predicting fatigue damage in adhesively bonded joints using a cohesive zone model. *International Journal of Fatigue*, 32(7):1146–1158, 2010.

[31] T.A. Hafiz, M.M. Abdel-Wahab, A.D. Crocombe, and P.A. Smith. Mixed-mode fatigue crack growth in FM73 bonded joints. *International Journal of Adhesion and Adhesives*, 40(0):188 – 196, 2013.

[32] N. Blanco, E.K. Gamstedt, L.E. Asp, and J. Costa. Mixed-mode delamination growth in carbon-fibre composite laminates under cyclic loading. *International Journal of Solids and Structures*, 41(15):4219–4235, 2004.

[33] Norbert Blanco Villaverde. *Variable mixed-mode delamination in composite laminates under fatigue conditions: testing & analysis.* PhD thesis, Universitat de Girona, 2004.

[34] R.L. Ramkumar and J.D. Whitcomb. Characterization of mode I and mixed-mode delamination growth in T300/5208 graphite/epoxy. pages 315–335. American Society for Testing and Materials, Philadelphia, 1985.

[35] C.G.Gustafson and M. Hojo. Delamination fatigue crack growth in unidirectional graphite/epoxy laminates. *Journal of Reinforced Plastics and Composites*, 6(1):36–52, 1987.

[36] A.J. Russel and K.N. Street. Predicting interlaminar fatigue crack rates in compressively loaded laminates. In *Delamination and Debonding of Materials ASTM STP 1012*, pages 162–178. American Society for Testing Materials, 1989.

[37] C. Dahlen and G.S.Springer. Delamination growth in composites under cyclic loads. *Journal of Composite Materials*, 28(8):732–781, 1994.

[38] G.A. Kardomateas, A.A. Pelegri, and B. Malik. Growth of internal delamination under cyclic compression in composite plates. *Journal of the Mechanics and Physics of Solids*, 43(6):847–868, 1995.

[39] M. Kenane and M.L. Benzeggagh. Mixed-mode delamination fracture toughness of unidirectional glass/epoxy composites under fatigue loading. *Composites Science and Technology*, 57(5):597–605, 1997.

[40] J. Schön. A model of fatigue delamination in composites. *Composites Science and Technology*, 60(4):553–558, 2000.

[41] J. Andersons, M. Hojo, and S.Oschiai. Model of delamination propagation in brittle-matrix composites under cyclic loading. *Journal of Reinforced Plastics and Composites*, 20(5):431–450, 2001.

[42] Tanaka H. and Tanaka K. Mixed-mode growth of interlaminar cracks in carbon/epoxy laminates under cyclic loading. In *Proceedings of the 10th International Conference on Composite Materials 1*, pages 181–189, Whistler (Canada), 1995.

[43] L. E. Asp, A. Sjgren, and E. S. Greenhalgh. Delamination growth and thresholds in a carbon/epoxy composite under fatigue loading. *Journal of Composites Technology and Research*, 23(2):55–68, 2001.

[44] Z. Suo and J. W. Hutchinson. Interface crack between two elastic layers. *International Journal of Fracture*, 43(1):1–18, 1990.

[45] P. T. Cheuk, L. Tong, C. H. Wang, A. Baker, and P. Chalkley. Fatigue crack growth in adhesively bonded composite-metal double-lap joints. *Composite Structures*, 57(1-4):109–115, 2002.

[46] M. Quaresimin and M. Ricotta. Stress intensity factors and strain energy release rates in single lap bonded joints in composite materials. *Composites Science and Technology*, 66(5):647–656, 2006.

[47] P. A. Carraro, G. Meneghetti, M. Quaresimin, and M. Ricotta. Crack propagation analysis in composite bonded joints under mixed-mode (I+II) static and fatigue loading: Experimental investigation and phenomenological modelling. *Journal of Adhesion Science and Technology*, 27(11):1179–1196, 2013.

[48] P. A. Carraro, G. Meneghetti, M. Quaresimin, and M. Ricotta. Crack propagation analysis in composite bonded joints under mixed-mode (I + II) static and fatigue loading: A damage-based model. *Journal of Adhesion Science and Technology*, 27(13):1393–1406, 2013.

[49] M. Quaresimin and M. Ricotta. Life prediction of bonded joints in composite materials. *International Journal of Fatigue*, 28(10 SPEC. ISS.):1166–1176, 2006.

[50] M. Quaresimin and M. Ricotta. Fatigue behaviour and damage evolution of single lap bonded joints in composite material. *Composites Science and Technology*, 66(2):176–187, 2006.

[51] S. Zhao, M. Gadke, and R. Prinz. Mixed-mode delamination behavior of carbon/epoxy composites. *Journal of Reinforced Plastics and Composites*, 14(8):804–826, 1995.

[52] F. Heutling, H. E. Franz, and K. Friedrich. Microfractographic analysis of delamination growth in fatigue loaded - carbon fibre/thermosetting matrix composites. *Materialwissenschaft und Werkstofftechnik*, 29(5):239–253, 1998.

[53] M. Kenane, S. Benmedakhene, and Z. Azari. Fracture and fatigue study of unidirectional glass/epoxy laminate under different mode of loading. *Fatigue & Fracture of Engineering Materials & Structures*, 33(5):284–293, 2010.

[54] D. Bürger, C. D. Rans, and R. Benedictus. Characterization of mixed-mode fatigue failure on metallic bonded joints. In *ICAF 2013 Symposium - Proceedings of the 27th Symposium of the International Committee on Aeronautical Fatigue*, pages 751–760, 2013.

[55] Z. Wan, T. Teng, and C. Li. Fatigue and fracture of adhesively bonded composite joints under mixed mode I/II loading. Technical report, National Research Council Canada, 2013.

[56] Z. Liu, R. F. Gibson, and G. M. Newaz. Improved analytical models for mixed-mode bending tests of adhesively bonded joints. *Journal of Adhesion*, 78(3):245–268, 2002.

3 Test Results

3.1 Introduction

The development and evaluation of a Mixed-Mode (MM) fatigue disbond model requires experimental results. The two major expected outcomes from the experiments are the fracture surfaces and the Fatigue Disbond Growth (FDG) data. The fracture surfaces will be analyzed in search of failure mechanisms, which will later support the development of a MM fatigue disbond model. Afterwards, part of the FDG data will serve as model inputs (namely pure Mode I and pure Mode II data) and part will serve for model evaluation (MM data).

3.2 Tests review

The disbond study can be done with several test setups, such as T-peel test [1] or floating roller peel test [2]. However, these tests are used to assess the failure load and/or the failure type (cohesive or interfacial) [3]. Hence, researchers resort to delamination tests for fatigue disbond growth rate evaluation.

So far, there have been efforts to produce a standard method to evaluate the fatigue delamination resistance [4–6]. However these efforts are still in an early stage and the researchers have not reached a consensus yet. As a result, the most used test setups to asses the delamination growth rate behavior will be briefly addressed.

3.2.1 Mode I

For Mode I loading, the most important test setups are the (i) Double Cantilever Beam (DCB) [7–12] and the (ii) Tapered DCB (TDCB) [13–19]. The main difference between these test setups is how the Strain Energy Release Rate (SERR) changes with an increasing crack length. On the DCB specimens the SERR depends only on loading parameters (e.g. force) and on the delamination length, as the other geometric variables (thickness and width) remain constant. On the TDCB specimens, one can design the specimen, with a variable width or thickness. Consequently, as the delamination increases, the SERR changes according to a desired function.

So far, no setup has been standardized for fatigue disbond growth study under Mode I loading [20]. However, the DCB is already used in the standards for Mode I interlaminar fracture toughness [21] and Mode I fatigue delamination growth onset [22] of composites and it is being considered for a fatigue delamination resistance standard

[5]. As a result, the DCB (Fig. 3.1) test is the preferred for Mode I delamination [20] and disbond studies.

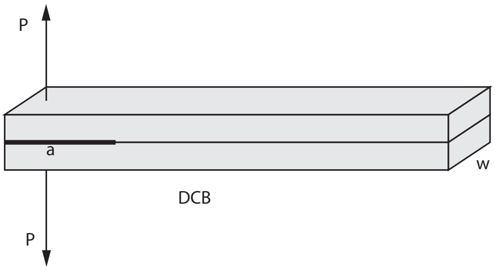

Figure 3.1: *DCB test setup.*

3.2.2 Mode II

The End Notched Flexure (ENF) (Fig. 3.2) test is the most employed test for Mode II fatigue loading [8, 12]. This test relies on the generation of a state of pure shear along the neutral line of a beam in bending. However, problems such as unstable delamination growth (for static failure) and friction between the adherends still raise questions about the results significance. A variation of this test, the four point ENF (Fig. 3.3), can solve the delamination growth instability but it still requires more knowledge before a wider use [20].

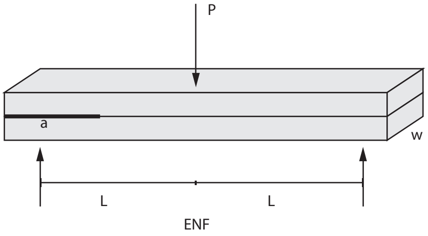

Figure 3.2: *ENF test setup.*

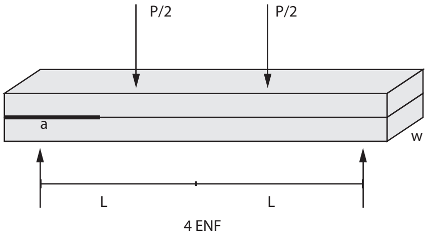

Figure 3.3: *4ENF test setup.*

Among the main problems of the ENF test one can cite [6]: (i) the data analysis is mainly done using beam theory, without correction factors; (ii) the slip of the specimen during the fatigue loading due to the asymmetrical bending stiffness of the specimen; (iii) if a restraining device is used to correct the slip, then it can potentially affect the results; (iv) the compressive stress the adhesive layer is subjected to might have an influence on the fatigue behavior; (v) there is still no study evaluating the effect of the different test parameters on the fatigue behavior.

Additionally to the ENF, the End Loaded Split (ELS), Fig. 3.4, test is also being considered for a Mode II fatigue delamination resistance standard [6]. However, there were unexplained differences between the results from the ENF and ELS tests.

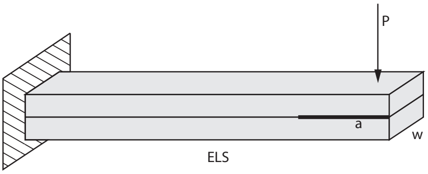

Figure 3.4: *ELS test setup.*

3.2.3 Mixed-Mode

The study of MM loading present more options, such as Mixed-Mode Bending (MMB) test [12], Cracked Lap Shear (CLS) [8, 9, 23, 24], Compact Tension Shear (CTS) [25], asymmetric DCB (asymmetric loading or adherends) [11, 24], and Single Lap Joint (SLJ) [10, 17, 26–30]. Most of these test setups (CLS, asymmetric DCB and SLJ) present limitations on the Mode Ratio (MR) range that can be evaluated; thus, the study of the complete MR range requires the MMB (Fig. 3.5) or the CTS. As the MMB is the standard for MM interlaminar fracture toughness of composite materials [31], it is also the most used test for MM fatigue delamination studies [20]. Additionally, at a particular arrangement of the MMB setup, the test is equivalent to a ENF test, i.e., it can test pure Mode II.

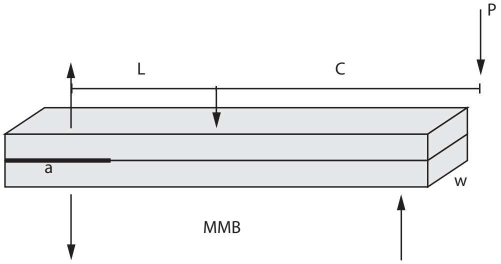

Figure 3.5: *MMB test setup.*

3.2.4 Selected Tests

As a result of the literature review, the DCB (for pure Mode I) and the MMB (for MM and pure Mode II) were selected as the most suitable test setup to evaluate the fatigue disbond behavior on a metal-to-metal bonded interface.

3.3 Experimental Procedure

An experimental study was carried out to characterize the MM fatigue disbond behavior on metal-to-metal interfaces. The adhesive employed was FM-94.

3.3.1 Description of test series

In order to evaluate the MM fatigue disbond behavior the experiments will be divided into four sets: (i) pure Mode I and II, (ii) MM - FDG, (iii) MM - fracture surfaces and (iv) unsupported. The goal of the pure Mode I and II is to provide input values for the development of a MM fatigue disbond model and to produce fracture surfaces for the study of the failure mechanisms under pure Mode I and II loading. The objective of the MM - FDG is to generate data to test and evaluate the MM fatigue disbond model. The goal of the third set, MM - fracture surfaces, is to produce fracture surfaces over a wide MR range, so the differences in the failure mechanisms can be observed. The first three sets of experiments were performed on a supported adhesive. Supported adhesives are adhesives in a film form that incorporate a carrier. The carrier helps to avoid thickness deviations on the adhesive after cure and it can also allow for the adhesive to be easily handle, cut and positioned [32]. In order to assess the potential influence of the support system on the observed fracture behavior, the last set of tests compares the behavior of supported and unsupported adhesives. As the majority of tests refer to supported adhesive, unless clearly stated the supported adhesive should be assumed. A summary of the sets of experiments performed with their respective goal, MR, and number of specimens is provided below.

Set of experiments: **Pure Mode I and II**

Goal: produce FDG data for MM fatigue disbond model input and fracture surfaces for failure mechanims study.

Mode ratio: 0% and 100%.

*Number of specimens:*3

Set of experiments: **MM - FDG**

Goal: produce FDG data to test and evaluate the MM fatigue disbond model

Mode ratio: 25%, 50% and 75%.

*Number of specimens:*3

Set of experiments: **MM - fracture surface**

Goal: produce fracture surfaces to study the MM failure mechanisms and support the development of a MM fatigue disbond model.

Mode ratio: 20%, 30%, 40%, 50%, 60%, 70%, 80% and 90%.

*Number of specimens:*1

Set of experiments: **unsupported**

Goal: produce FDG data and fracture surfaces to evaluate the effect of the supporting system on the MM fatigue disbond behavior.

Mode ratio: 0%, 50% and 100%.

*Number of specimens:*3

3.3.2 Test setup and Data Collection

The tests performed were based on the DCB [21] and on the MMB [31] standards (see Fig. 3.6). The Mode II test was performed at a particular arrangement of the MMB setup. In the condition where C (lever length) is equal to L/3 (half-span length), the Mode I contribution is equal to zero; thus, the test is in pure Mode II.

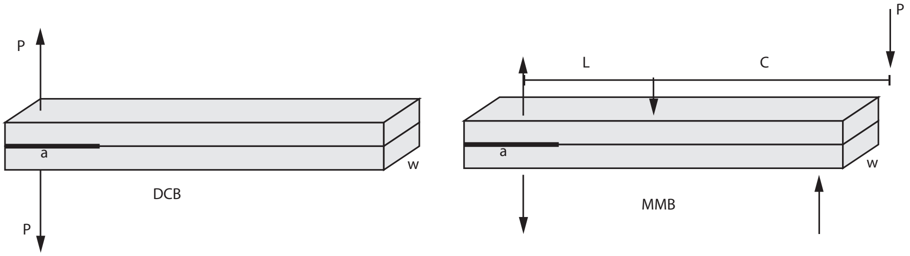

Figure 3.6: *Test details.*

Disbond growth was monitored visually by observing the location of the disbond tip at the side of the specimen. After a certain number of cycles the test was stopped, a picture was taken and the test was continued. Subsequently, the pictures were analyzed and the crack tip determined. A thin layer of white paint was added to the side of the specimen prior to testing to improve the contrast between the specimen and disbond, aiding in visual detection. The disbond growth rate was calculated using the Incremental Polynomial Method [33] with seven successive data points and a second order polynomial equation. After the fatigue test, the specimens were dismantled, coated with gold and observed in the SEM with magnification from 50x to 10.000x.

A minimum of three specimens was tested in each of the MRs of the pure Mode I and II, the MM - FDG and the unsupported sets in order to produce reliable Paris relation coefficients. And only one specimen was tested in the set MM - fracture surface as this set only intends to produce fracture surfaces for failure mechanisms evaluation. For this set of tests the fatigue disbond was allowed to grow for 1 cm and then the MR was changed.

3.3.3 Specimen Geometry and Fabrication Details

Aluminum (2024-T3) adherends, with 6mm thickness were used. The aluminum sheets were cleaned with acetone, followed by a NaOH bath for 5 minutes, and then Chromic Acid Anodized (CAA) for 40 minutes at 40^{o}C. After the CAA, the primer BR 127, supplied by Cytec®, was applied on the aluminum sheets to preserve the surface treatment. Afterwards, the aluminum sheets were stored from 1 to 15 months. According to the primer and adhesive data sheet [34], primed adherends can be stored for long periods without degradation of the final bonding. Prior to stacking, a thin film of Teflon (50mm width and 0.06mm thick) was positioned close to the edge of the metal sheets to create a initial disbond. The bond plates were prepared with one adhesive layer and no extra technique, apart from the fabric carrier on the respective set of experiments, was used to control the thickness.

The adhesive employed was FM-94, supplied by Cytec and it was supplied in a supported (with a fabric carrier) and unsupported version with a nominal thickness of

250μm. The cure cycle followed the supplier instruction [34] and consists of: heating up to 120^{o}C at 2^{o}C/min; holding at 120^{o}C for 60 minutes with a pressure of 0.4MPa; cool down to 30^{o}C at 4^{o}C/min. After cure, the bonded plate was machined in the final dimensions of the samples in Fig. 3.7. The specimens were stored at 20 - 25^{o}C, relative humidity of 50-70%, for one to six months before testing and prior to testing the total sample thickness was measured. Piano hinges were fastened to the adherends for the specimen loading (see Fig. 3.7).

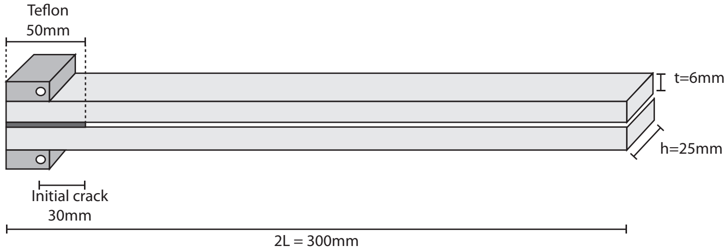

Figure 3.7: *Specimen details.*

3.3.4 Test details

During fatigue testing, the maximum and minimum displacement were kept constant to avoid unstable disbond growth. The behaviors of the G_{max} vs disbond length in a fatigue test with constant displacement on a DCB and on a MMB specimen are depicted in Fig. 3.8 and 3.9, respectively.

The failure on an epoxy occurs as a consequence of the coalescence of micro-cracks ahead of the crack tip [35]. Consequently, in a fatigue test the previous loads have an important effect on the failure, as they are responsible for the damage level ahead of the crack tip. A larger load should impose more damage and damage a larger region ahead of the crack tip. Thus, if a lower load follows a larger load, it can present a faster disbond growth rate than expected, as the material is more damaged than expected because of the previous higher load. This is the basic mechanism for the damage accelerative load interaction observed on bonded joints under variable amplitude loading [36]. As a result, on the MMB setup, the test was limited to the region where $\frac{dG}{da} \geq 0$ (Fig. 3.9). The same approach was not applied to the DCB test (Fig. 3.8) because of the other standards based on this test setup [21, 22], which contain correction factors that limit the error of the test setup.

The load ratio was set as R=0.1 and the frequency was 5 Hz. The fatigue tests were conducted in the region II of the disbond growth rate, usually described by the Paris relation or a variant of it. Prior to the fatigue loading, Mode I loading was applied to increase the disbond length. This procedure guarantees a sharp crack tip and reduces the influence of the Teflon film.

3.3.5 Data Reduction

For the Mode I data reduction, the three methods (Modified Beam theory, Compliance Calibration and Modified Compliance Calibration) presented in the standard [21]

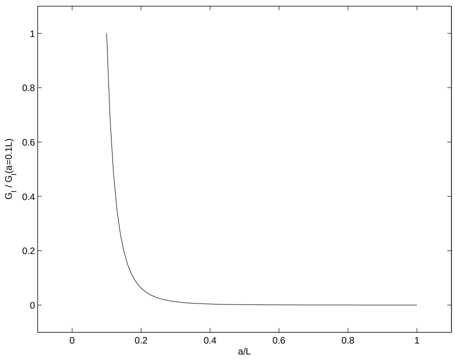

Figure 3.8: *G_{max} as a function of disbond length for a constant displacement DCB test.*

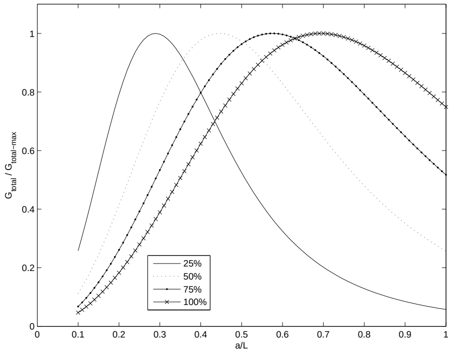

Figure 3.9: *G_{max} as a function of disbond length for a constant displacement MMB test.*

showed similar results and the Modified Compliance Calibration Method (Eq. 3.1) was chosen to reduce the data.

$$G_I = \frac{3P^2 Comp^{2/3}}{2A_1 wt} \tag{3.1}$$

For the MM and Mode II data reduction, the equations proposed (Eq. 3.2 and 3.3) in the standard [31] were used, as they take into account delamination/disbond length corrections and the lever arm weight. The disbond length correction parameter χ was calculated according to the standard [31], using the properties of the adherend (Aluminum).

$$G_I = \frac{12[P(3C-L)+P_g(3C_g-L)]^2}{16w^2t^3L^2E}(a+\chi t)^2 \tag{3.2}$$

$$G_{II} = \frac{9[P(C+L)+P_g(C_g+L)]^2}{16w^2t^3L^2E}(a+0.42\chi t)^2 \tag{3.3}$$

3.4 Test results

The total average thickness of the samples was 12.24±0.03 mm for the supported adhesive and 12.25±0.03 mm for the unsupported adhesive. The fatigue results of the first (pure Mode I and II), second (MM - FCG), third (MM - fracture surfaces) and the forth set of tests (unsupported) are presented in Fig. 3.10, 3.11, 3.12 and 3.13, respectively.

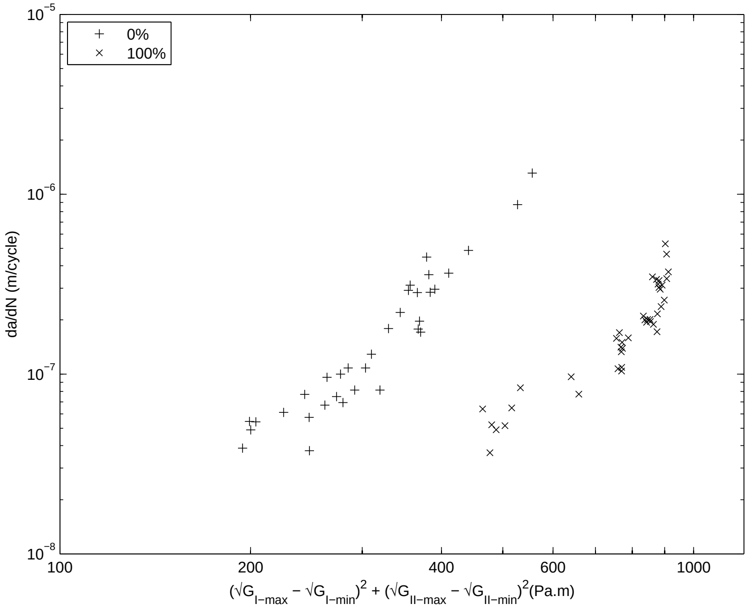

Figure 3.10: *Fatigue disbond growth behavior. Pure Mode I and II.*

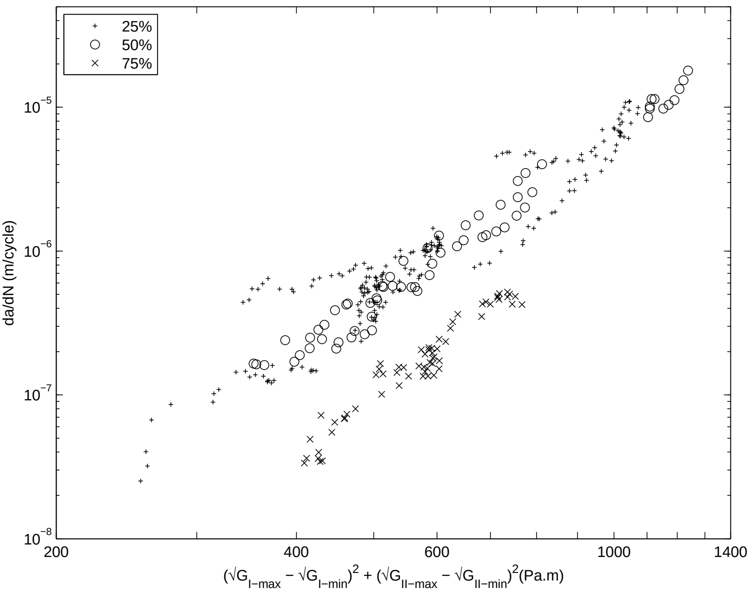

Figure 3.11: *Fatigue disbond growth behavior. Mixed-Mode - FCG.*

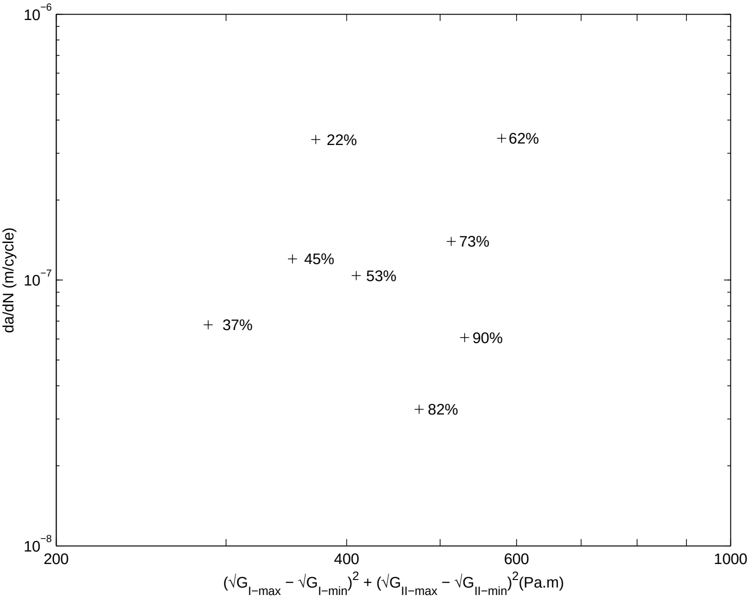

Figure 3.12: *Fatigue disbond growth behavior. MM - fracture surfaces set. The numbers in the figure indicate the MR.*

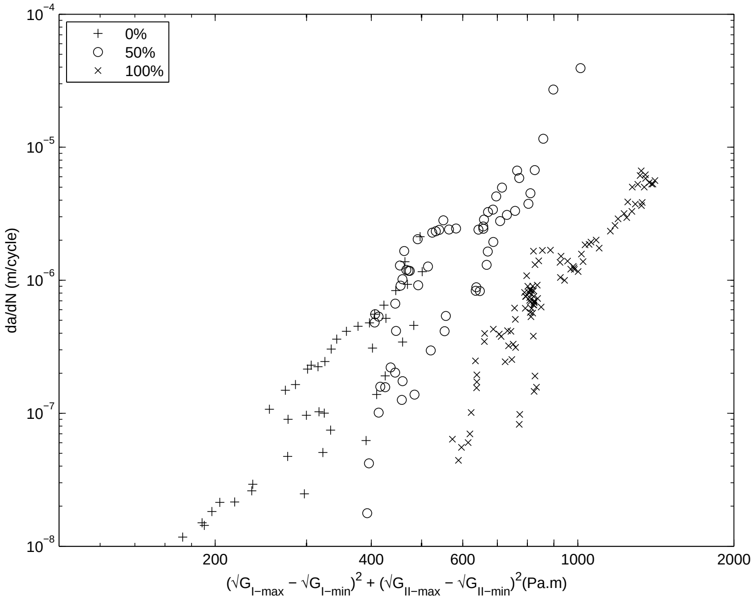

Figure 3.13: *Fatigue disbond growth behavior. Unsupported set (unsupported adhesive).*

3.5 Paris Relation Coefficients

Similarly to metals, experimental observations suggest that FDG follows a Paris relation written as a function of the SERR [37]. However, these observations are not supported by any physical evidence [38]. As a result, a number of modifications to the Paris relation has been implemented to deal with different problems such as stress ratio, MR, and others [38].

Particularly for the MM problem, a number of functions have been proposed. The most used functions are G_{max} and $\Delta G = G_{max} - G_{min}$ [37]. However the G_{max} formulation ignores the cyclic load amplitude and the ΔG depends on both cyclic load amplitude and mean, as demonstrated by [37]. Alternatively, the new definition of $\Delta\sqrt{G} = (\sqrt{G_{I-max}} - \sqrt{G_{I-min}})^2 + (\sqrt{G_{II-max}} - \sqrt{G_{II-min}})^2$ proposed by [37] depends only on the cyclic load amplitude. Thus, the later was chosen for the calculation of the Paris relation parameters.

3.5.1 Regression Analysis Review

Obtaining the FDG curve for different MR is the first step towards a MM model evaluation. The second step is to derive the Paris relation coefficients to introduce them in the model. This procedure is done by supposing a function that fits the experimental data and varying the parameters of this function to minimize a controlling parameter, usually the sum of squared errors (least squares - Eq. 3.4 with $w_i = 1$) or the sum of squared errors multiplied by a factor (weighted least squares - Eq. 3.4) [39].

$$S = \sum_{i=1}^{n} w_i [y_i - f(x_i)]^2 \tag{3.4}$$

Where x_i and y_i are the experimental points and w_i are the weights.

If the function chosen is simple, such as a linear function, this approach yields an analytical solution. One can differentiate the parameter S with respect to the two parameters of the function $f(x) = \beta_0 + \beta_1 x$ and solve the system of equations $\frac{\partial S}{\partial \beta_i} = 0$ to find the coefficients β_i correspondent to the minimum value of S:

$$S = \sum_{i=1}^{n} [y_i - (\beta_0 + \beta_1 x_i)]^2 \tag{3.5}$$

$$\begin{cases} \dfrac{\partial S}{\partial \beta_0} = -2\displaystyle\sum_{i=1}^{n}(y_i - \beta_0 - \beta_1 x_i) = 0 \\ \dfrac{\partial S}{\partial \beta_1} = -2\displaystyle\sum_{i=1}^{n}(y_i - \beta_0 - \beta_1 x_i)x_i = 0 \end{cases} \tag{3.6}$$

$$\begin{cases} \sum(y_i - \beta_0 - \beta_1 x_i) = 0 \\ \sum(y_i - \beta_0 - \beta_1 x_i)x_i = 0 \end{cases} \tag{3.7}$$

$$\begin{cases} n\beta_0 + (\sum x_i)\beta_1 = \sum y_i \\ (\sum x_i)\beta_0 + (\sum x_i^2)\beta_1 = \sum y_i x_i \end{cases} \tag{3.8}$$

Thus,

$$\beta_1 = \frac{\sum x_i . \sum y_i - n. \sum x_i . y_i}{(\sum x_i)^2 - n. \sum x_i^2} \qquad \beta_0 = \frac{\sum y_i - \beta_1 \sum x_i}{n} \tag{3.9}$$

However, the Paris relation is a power law. Thus, an analytical solution is not possible. One can solve this problem by linearizing the function or by using an iteration method to find the coefficients. Commercial spreadsheets softwares (e.g. Excel - Microsoft, Calc - OpenOffice) linearize the power law function to determine the coefficients.

$$f(x) = c.x^m \tag{3.10}$$

$$log(f(x)) = log(c.x^m) \tag{3.11}$$

$$log(f(x)) = log(c) + m.log(x)) \tag{3.12}$$

$$f'(x) = c' + m.x' \tag{3.13}$$

In the sequence, the coefficients c' and m can be easily obtained [39]:

$$\beta = \begin{bmatrix} c' & m \end{bmatrix} T = (X^T.X)^{-1}.(X^T.Y) \tag{3.14}$$

Where X and Y are given by the matrices containing the experimental points (x_i, y_i):

$$X = \begin{bmatrix} 1 & x_1 \\ 1 & x_2 \\ \vdots & \vdots \\ 1 & x_n \end{bmatrix} \qquad Y = \begin{bmatrix} y_1 \\ y_2 \\ \vdots \\ y_n \end{bmatrix} \tag{3.15}$$

However, by linearizing the power law function, one would minimize not the sum of the squared error but the sum of the squared error of the log (Eq. 3.16). This introduces an artificial weight (Eq. 3.17).

$$S' = \sum_{i=1}^{n} [log(y_i) - log(f(x_i))]^2 \tag{3.16}$$

$$w_i = \frac{[log(y_i) - log(f(x_i))]^2}{[y_i - f(x_i)]^2} \tag{3.17}$$

If the error (e) is assumed to be proportional to value observed y_i, the weight becomes:

$$w_i = \frac{[log(y_i) - log(y_i(1+e))]^2}{[y_i - y_i(1+e)]^2} = \frac{1}{y_i^2}\left(\frac{log(1+e)}{e}\right)^2 \tag{3.18}$$

As,

$$\lim_{e \to 0} \frac{log(1+e)}{e} = 1 \tag{3.19}$$

$$\lim_{e \to 0} w_i = \frac{1}{y_i^2} \tag{3.20}$$

Thus, if $y_i >> y_j$ then $w_i << w_j$, i.e., linearizing the power law function results in an artificial high weight for the smaller values of y_i. One way of solving this issue is applying a weight to correct this artificial weight. For the power law function, the most used weight is the factor y_i. Then, the parameter which is minimized becomes:

$$S = \sum_{i=1}^{n} y_i^2 [log(y_i) - log(f(x_i))]^2 \tag{3.21}$$

And the coefficients c_1' and c_2 can be obtained:

$$\begin{bmatrix} c_1' & c_2 \end{bmatrix}^T = ((W.X)^T.(W.X))^{-1}.((W.X)^T.(W.Y)) \tag{3.22}$$

Where:

$$W = \begin{bmatrix} y_1 & 0 & ... & 0 \\ 0 & y_2 & ... & 0 \\ \vdots & \vdots & \ddots & \vdots \\ 0 & 0 & \dots & y_n \end{bmatrix} \tag{3.23}$$

Both methods described above attempt to reduce the distance between the experimental points obtained and the power function. However, Eqs. 3.16 and 3.21 show that in fact they don't reduce the distance between the experimental points and the power function but are an approximation of it.

An alternative to linearize the equation is to use an iteration method to minimize the least squares [39]. The details of this method are described elsewhere [39]. For the power law function the algorithm is described below. First the power function ($f(x)$) and its derivatives with respect to each coefficient ($z_i(x)$) must be defined.

$$f(x) = C.(\Delta\sqrt{G})^m \tag{3.24}$$

$$z_1(x) = \frac{\partial f(x)}{\partial C} = (\Delta\sqrt{G})^m \tag{3.25}$$

$$z_2(x) = \frac{\partial f(x)}{\partial m} = C.(\Delta\sqrt{G})^m.ln(\Delta\sqrt{G}) \tag{3.26}$$

Later an initial value for the coefficients is chosen.

$$\beta^0 = \begin{bmatrix} C^0 & m^0 \end{bmatrix}^T \tag{3.27}$$

And the matrices Z and $Resi$ are calculated:

$$Z^0 = \begin{bmatrix} z_1(x_1) & z_2(x_1) \\ z_1(x_2) & z_2(x_2) \\ \vdots & \vdots \\ z_1(x_n) & z_2(x_n) \end{bmatrix} \tag{3.28}$$

$$Resi^0 = \begin{bmatrix} y_1 - f(x_1) & \\ y_2 - f(x_2) & \\ \vdots & \vdots \\ y_n - f(x_n) & \end{bmatrix} \tag{3.29}$$

Thus, we can obtain the matrix $\hat{\beta}^0$

$$\hat{\beta}^0 = (Z^{0T}.Z^0)^{-1}.Z^{0T}.Resi^0 \tag{3.30}$$

Then, a new set of coefficients is obtained and the process is repeated until convergence.

$$\beta^1 = \begin{bmatrix} C^1 & m^1 \end{bmatrix}^T = \begin{bmatrix} C^0 & m^0 \end{bmatrix}^T + \hat{\beta}^0 \tag{3.31}$$

3.5.2 Coefficients Comparison

The three methods described above were employed to obtain the Paris Relation coefficients. A summary of the coefficients is presented in tables 3.1, 3.2 and 3.3.

Table 3.1: *Fit coefficients for the different fitting methods for the Pure Mode I and II set of experiments.*

method	0%		100%	
	C	m	C	m
Linear	$1.51\ 10^{-15}$	3.20	$1.14\ 10^{-15}$	2.83
Weighted	$1.86\ 10^{-16}$	3.58	$5.59\ 10^{-20}$	4.33
Iteration	$5.26\ 10^{-17}$	3.78	$2.23\ 10^{-24}$	5.81

Table 3.2: *Fit coefficients for the different fitting methods for the MM - FCG set of experiments.*

method	25%		50%		75%	
	C	m	C	m	C	m
Linear	$2.96\ 10^{-19}$	3.44	$2.16\ 10^{-17}$	3.82	$2.46\ 10^{-19}$	4.29
Weighted	$2.12\ 10^{-15}$	3.18	$2.17\ 10^{-17}$	3.83	$4.55\ 10^{-18}$	3.85
Iteration	$1.57\ 10^{-17}$	3.88	$1.12\ 10^{-17}$	3.92	$2.16\ 10^{-18}$	3.96

Table 3.3: *Fit coefficients for the different fitting methods for the unsupported set of experiments (unsupported adhesive).*

method	0%		50%		100%	
	C	m	C	m	C	m
Linear	$3.21\ 10^{-18}$	4.25	$2.62\ 10^{-20}$	4.96	$2.06\ 10^{-20}$	4.61
Weighted	$5.99\ 10^{-20}$	4.99	$7.60\ 10^{-22}$	5.57	$1.24\ 10^{-17}$	3.72
Iteration	$1.01\ 10^{-21}$	5.60	$4.03\ 10^{-26}$	6.99	$1.17\ 10^{-18}$	4.03

Observing tables 3.1, 3.2 and 3.3, one can notice the large difference between the values obtained through the different methods. As an example, for the $MR = 0\%$ the maximum difference in the coefficient m is 15%. Even so, the curves obtained with the three methods describe reasonably well the experimental points (Fig. 3.14).

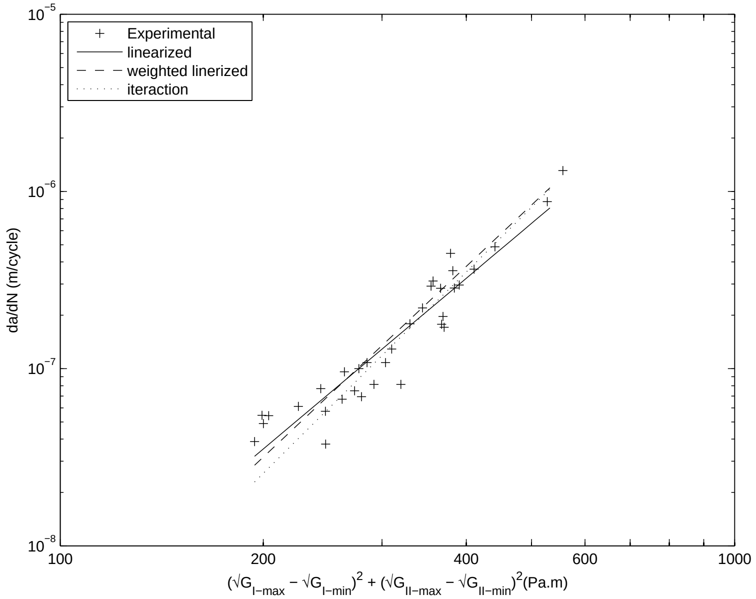

Figure 3.14: *Fatigue crack growth behavior. Mode I unsupported and the Paris relation obtained through the different regression methods.*

3.6 Predictions with available MM models

This section will present predictions of two MM models for the experimental data presented. The first model chosen was the one from Gustafson and Hojo [40] modified to incorporate the correction proposed by Rans *et al* [37] (eq. 3.32). This model is a superposition of Mode I and II contributions and as such uses only pure Mode I and pure Mode II experimental data as input.

$$\frac{da}{dN} = c_I.[(\sqrt{G_{Imax}} - \sqrt{G_{Imin}})^2]^{m_I} + c_{II}.[(\sqrt{G_{IImax}} - \sqrt{G_{IImin}})^2]^{m_{II}} \quad (3.32)$$

The second model chosen was Blanco *et al* [41] (eq. 3.33), currently one of the most used models. Blanco's model fits experimental data at different mode ratios. This model requires at least three MRs to solve the Eq. 3.33.

$$\begin{cases} \frac{da}{dN} = c_x(G_{max} - G_{min})^{m_x} \\ log(c_x) = c_1 + c_2MR + c_3MR^2 \\ m_x = m_1 + m_2MR + m_3MR^2 \end{cases} \quad (3.33)$$

In Blanco's model [41], usually, the pure Mode I and pure Mode II coefficients are the first to be obtained (first set of experiments). Consequently, the model requires one extra MR as input. The second set of experiments (MM - FDG) contains three MRs (25%, 50% and 75%), so each MR can have two predictions, one from each of the remaining MRs. E.g., for MR=25%, the first prediction used as inputs the data from MR=0%, 50% and 100%; and the second prediction used as inputs the data from MR=0%, 75% and 100%.

As, Blanco's model [41] was developed in terms of $\Delta G = G_{max} - G_{min}$, it requires a new Paris relation coefficients. The new coefficients, obtained with the iteration method, are presented in Tab. 3.4.

Table 3.4: *Paris relation coefficients for input on Blanco's model.*

MR	C	m
0%	$2.52\ 10^{-19}$	4.52
25%	$3.62\ 10^{-18}$	3.98
50%	$2.84\ 10^{-20}$	4.67
75%	$6.03\ 10^{-17}$	3.33
100%	$2.59\ 10^{-21}$	4.65

The coefficients predicted by Blanco's model are presented in Tab. 3.5.

Table 3.5: *Paris relation coefficients output from Blanco's model. The output from the model was generated using three inputs, namely: 0%, 100% and one of the extra MRs available.*

		Model output	
MR evaluated	input MRs	C	m
25%	0%-50%-100%	$8.66\ 10^{-20}$	4.62
	0%-75%-100%	$9.62\ 10^{-16}$	3.20
50%	0%-25%-100%	$4.03\ 10^{-18}$	3.82
	0%-75%-100%	$6.68\ 10^{-15}$	2.79
75%	0%-25%-100%	$2.91\ 10^{-19}$	4.07
	0%-50%-100%	$8.22\ 10^{-21}$	4.68

The predictions from both models can be seen on Fig. 3.15, 3.16 and 3.17. From these figures one can observe that the linear superposition only predicted the MM behavior accurately for MR=25%. For MR=50% and 75% it predicts disbond growth rates one order of magnitude slower than the experimental observations.

The predictions from Blanco's model present a better agreement with the experimental results, specially for MR=25% and 75%. However, the predictions are better if the extra MR used as input is MR=50% (Fig. 3.15 and 3.17). If the extra MR used as input is MR=25%, the predictions are non-conservative, specially the prediction for MR=50%. If the extra MR is MR=75%, the predictions are reasonable, except for the faster disbond growth region on the prediction for MR=50%.

Altogether, the linear superposition model [40] modified by the correction of [37] yields poor and non-conservative predictions. And the model of Blanco *et al* [41] presents better predictions but often the results are non-conservative.

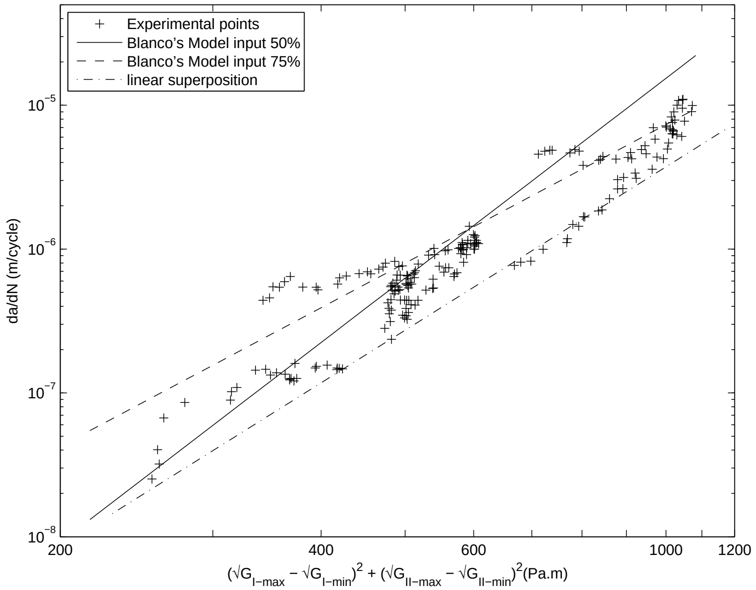

Figure 3.15: *MM Fatigue disbond growth behavior and the predictions with Blanco's [41] and superposition [37] models for MR=25%.*

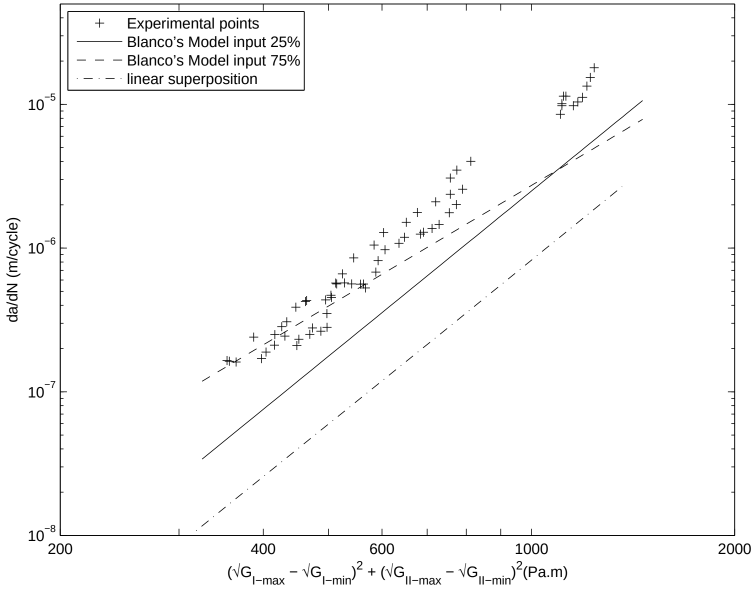

Figure 3.16: *MM Fatigue disbond growth behavior and the predictions with Blanco's [41] and superposition [37] models for MR=50%.*

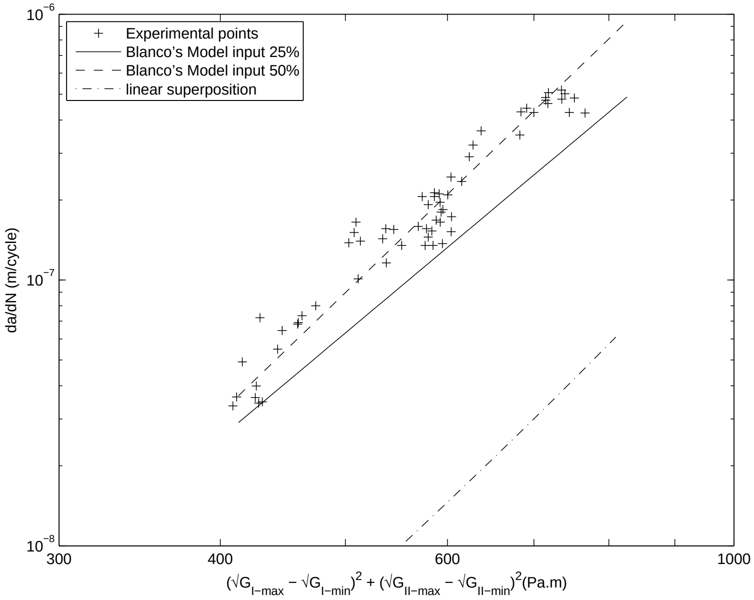

Figure 3.17: *MM Fatigue disbond growth behavior and the predictions with Blanco's [41] and superposition [37] models for MR=75%.*

3.7 Conclusions

This chapter has presented the details of the experimental program carried out to assess the MM fatigue disbond behavior. From these results, one can conclude that superimposing pure Mode I and pure Mode II contributions to predict the MM behavior is not possible and some form of interaction must be taking place. Additionally, the most used model in the literature [41] to predict MM disbond can yield non-conservative predictions. As a result, the next chapter will analyze the failure mechanisms of the MM fatigue disbond to support the development of a new MM fatigue disbond model.

References

[1] Standard test method for peel resistance of adhesives (T-Peel test), 2008.

[2] Standard test method for floating roller peel resistance of adhesives, 2010.

[3] S. T. De Freitas and J. Sinke. Adhesion properties of bonded composite-to-aluminium joints using peel tests. *Journal of Adhesion*, 90(5-6):511–525, 2014.

[4] R. Jones, S. Stelzer, and A. J. Brunner. Mode I, II and mixed mode I/II delamination growth in composites. *Composite Structures*, 110(1):317–324, 2014.

[5] A. J. Brunner, N. Murphy, and G. Pinter. Development of a standardized procedure for the characterization of interlaminar delamination propagation in ad-

vanced composites under fatigue mode I loading conditions. *Engineering Fracture Mechanics*, 76(18):2678–2689, 2009.

[6] A. J. Brunner, S. Stelzer, G. Pinter, and G. P. Terrasi. Mode II fatigue delamination resistance of advanced fiber-reinforced polymer-matrix laminates: Towards the development of a standardized test procedure. *International Journal of Fatigue*, 50:57–62, 2013.

[7] A.J. Kinloch and S.O. Osiyemi. Predicting the fatigue life of adhesively-bonded joints. *Journal of Adhesion*, 43(1-2):79–90, 1993.

[8] M. Dessurealt and J.K.Spelt. Observations of fatigue crack initiation and propagation in an epoxy adhesive. *International Journal of Adhesion & Adhesives*, 17(3):183–195, 1997.

[9] W.S. Johnson, L.M. Butkus, and R.V. Valentin. Applications of fracture mechanics to the durability of bonded composite joints. Technical report, U.S. Department of Transportation - Federal Aviation Administration, 1998.

[10] I.A. Ashcroft, V. Shenoy, G.W. Critcholow, and A.D. Crocombe. A comparison of the prediction of fatigue damage and crack growth in adhesively bonded joints using fracture mechanics and damage mechanics progressive damage methods. *The Journal of Adhesion*, 86(12):1203–1230, 2010.

[11] T.A. Hafiz, M.M. Abdel-Wahab, A.D. Crocombe, and P.A. Smith. Mixed-mode fatigue crack growth in FM73 bonded joints. *International Journal of Adhesion and Adhesives*, 40(0):188 – 196, 2013.

[12] P. A. Carraro, G. Meneghetti, M. Quaresimin, and M. Ricotta. Crack propagation analysis in composite bonded joints under mixed-mode (I+II) static and fatigue loading: Experimental investigation and phenomenological modelling. *Journal of Adhesion Science and Technology*, 27(11):1179–1196, 2013.

[13] D. A. Jablonski. Fatigue crack growth in structural adhesives. *Journal of Adhesion*, 11(2):125–143, 1980.

[14] M. Fernando, W.W. Harjoprayitno, and A.J.Kinloch. A fracture mechanics study of the influence of moisture on the fatigue behaviour of adhesively bonded aluminium-alloy joints. *International Journal of Adhesion & Adhesives*, 16(2):113–119, 1996.

[15] J.K. Jethwa and A.J.Kinloch. The fatigue and durability behaviour of automotive adhesives. part i: Fracture mechanics tests. *Journal of Adhesion*, 61(1-4):71–95, 1997.

[16] A. J. Curley, H. Hadavinia, A. J. Kinloch, and A. C. Taylor. Predicting the service-life of adhesively-bonded joints. *International Journal of Fracture*, 103(1):41–69, 2000.

[17] H. Hadavinia, A. J. Kinloch, M. S. G. Little, and A. C. Taylor. The prediction of crack growth in bonded joints under cyclic-fatigue loading I. Experimental studies. *International Journal of Adhesion and Adhesives*, 23(6):449–461, 2003.

[18] J. Jia and J.F. Davalos. Study of load ratio for mode-I fatigue fracture of wood-FRP-bonded interfaces. *Journal of Composite Materials*, 38(14):1211–1230, 2004.

[19] M.-L. Abel, A.N.N. Adams, A.J. Kinloch, S.J. Shaw, and J.F. Watts. The effects of surface pretreatment on the cyclic-fatigue characteristics of bonded aluminium-alloy joints. *International Journal of Adhesion & Adhesives*, 26(1-2):50–61, 2006.

[20] A.J. Brunner, B.R.K. Blackman, and P. Davies. A status report on delamination resistance testing of polymer-matrix composites. *Engineering Fracture Mechanics*, 75(9):2779–2794, 2008.

[21] Standard test method for Mode I interlaminar fracture toughness of unidirectional fiber-reinforced polymer matrix composites, 2007.

[22] Standard test method for Mode I fatigue delamination growth onset of unidirectional fiber-reinforced polymer matrix composites, 1997.

[23] X. X. Xu, A. D. Crocombe, and P. A. Smith. Mixed-mode fatigue and fracture behaviour of joints bonded with either filled or filled and toughened adhesive. *International Journal of Fatigue*, 17(4):279–286, 1995.

[24] N.D. Datla, M. Papini, J.A. Schroeder, and J.K Spelt. Modified DCB and CLS specimens for mixed-mode fatigue testing of adhesively bonded thin sheets. *International Journal of Adhesion & Adhesives*, 30(6):439–447, 2010.

[25] A. Pirondi and G. Nicoletto. Mixed-mode I/II fatigue crack growth in adhesive joints. *Engineering Fracture Mechanics*, 73(16):2557–2568, 2006.

[26] M. W. Rushforth, P. Bowen, E. McAlpine, X. Zhou, and G. E. Thompson. The effect of surface pretreatment and moisture on the fatigue performance of adhesively-bonded aluminium. *Journal of Materials Processing Technology*, 153-154(1-3):359–365, 2004.

[27] P.R. Underhill and D.L. DuQuesnay. The dependence of the fatigue life of adhesive joints on surface preparation. *International Journal of Adhesion & Adhesives*, 26(1-2):62–66, 2006.

[28] M. Quaresimin and M. Ricotta. Fatigue behaviour and damage evolution of single lap bonded joints in composite material. *Composites Science and Technology*, 66(2):176–187, 2006.

[29] H. Khoramishad, A. D. Crocombe, K. B. Katnam, and I. A. Ashcroft. Predicting fatigue damage in adhesively bonded joints using a cohesive zone model. *International Journal of Fatigue*, 32(7):1146–1158, 2010.

[30] Y. . Jen and C. . Ko. Evaluation of fatigue life of adhesively bonded aluminum single-lap joints using interfacial parameters. *International Journal of Fatigue*, 32(2):330–340, 2010.

[31] Standard test method for mixed Mode I-Mode II interlaminar fracture toughness of unidirectional fiber reinforced polymer matrix composites, 2006.

[32] L. F. M. Da Silva, R. D. Adams, and M. Gibbs. Manufacture of adhesive joints and bulk specimens with high-temperature adhesives. *International Journal of Adhesion and Adhesives*, 24(1):69–83, 2004.

[33] Standard test method for measurement of fatigue crack growth rates, 2000.

[34] Cytec Engineered Materials. *FM 94 Adhesive Film - Technical Data Sheet*, 2010.

[35] R. A. Kline and F. H. Chang. Composite failure surface analysis. *Journal of Composite Materials*, 14:315–324, 1980.

[36] V. Shenoy, I.A. Ashcroft, G.W. Critchlow, and A.D. Crocombe. Fracture mechanics and damage mechanics based fatigue lifetime prediction of adhesively bonded joints subjected to variable amplitude fatigue. *Engineering Fracture Mechanics*, 77(7):1073–1090, 2010.

[37] C.D. Rans, R. Alderliesten, and R. Benedictus. Misinterpreting the results: How similitude can improve our understanding of fatigue delamination growth. *Composites Science and Technology*, 71(2):230–238, 2011.

[38] J. A. Pascoe, R. C. Alderliesten, and R. Benedictus. Methods for the prediction of fatigue delamination growth in composites and adhesive bonds - A critical review. *Engineering Fracture Mechanics*, 112-113:72–96, 2013.

[39] D.C. Montgomery, E.A. Peck, and G.G. Vining. *Introduction to linear regression analysis*. Wiley series in probability and statistics: Texts, references, and pocketbooks section. Wiley, 2001.

[40] C.G.Gustafson and M. Hojo. Delamination fatigue crack growth in unidirectional graphite/epoxy laminates. *Journal of Reinforced Plastics and Composites*, 6(1):36–52, 1987.

[41] N. Blanco, E.K. Gamstedt, L.E. Asp, and J. Costa. Mixed-mode delamination growth in carbon-fibre composite laminates under cyclic loading. *International Journal of Solids and Structures*, 41(15):4219–4235, 2004.

4 Fatigue Disbond Fracture Mechanisms

4.1 Introduction

The Mixed-Mode (MM) fatigue disbond has been addressed by many researchers [1–6]. However, how the failure process occurs is yet not clear. As discussed in Chapter 3, the analysis of the failure process can support the development of a more robust MM model, leading to a model less dependent on experimental inputs.

This chapter investigates the failure mechanisms of fatigue disbond under MM conditions and how these mechanisms change with the Mode Ratio (MR). First, a brief review of failure mechanisms on composite materials delamination is provided. Later, these mechanisms are compared with the experimental observations in MM fatigue disbond and the disbond mechanisms are described.

4.2 Generalized Fracture Description

A failure under cyclic load usually follows the sequence: nucleation of a small crack, growth of this crack and final failure. For metallic materials, the nucleation consists of cyclic plastic deformation, i.e., dislocations on the crystalline structure of a material's grain. As the micro-cracks extend, they tend to grow perpendicularly to the loading direction. When the crack reaches a critical size, the final failure occurs [7].

Similarly to metals, an adhesive failure follows the sequence: micro-cracks nucleation, growth and coalescence. However, due to the absence of crystals the dislocation process does not occur. Instead, the loading process leads to a complex scenario of plastic deformation which includes the stretching, rotation, sliding and disentanglement of the polymeric chains [8]. Later, the increase in the load level results in the break of crosslinks (for thermosets such as epoxy) and/or the polymeric chains, creating a craze [8].

One of the most important differences between metallic and polymeric materials failure is that several micro-cracks nucleate at the same time and they growth simultaneously at different growth rates and directions on polymers [9]. The nucleation of the micro-cracks is the first step of the failure process. A local tensile state [10] creates micro-voids ahead of the crack tip [9]. As the load increases, the micro-voids extend to accommodate the stresses [9] generating micro-cracks. Later, two adjacent micro-cracks coalesce when they have reached a critical size [9]. If the micro-cracks coalesce with the main crack, the result is crack extension.

Due to material inhomogeneities and loading conditions, the micro-cracks can nucleate and grow at different angles, generating different micro-cracks density ahead of the crack tip. The different ways the micro-cracks nucleate and grow result in several coalescence modes, which generate the different features observed in the fractographic analysis. The literature presents few references about the failure mechanisms on a MM fatigue disbond. Thus, the next section will present a review of similar failure mechanisms for a later comparison with the disbond failure mechanisms.

4.3 Composite Delamination Review

Fiber reinforced polymer composites are one of the most promising materials for reducing the structural weight in the aerospace industry [11] and delamination is the most critical failure mode in composites [12]. As such, there is a vast literature dedicated to the delamination problem.

A delamination can be described as the failure between two adjacent plies of a laminated material. Thus, the delamination presents similarities to a disbond, as both deal with the failure of a weaker material (matrix for delamination and adhesive for disbond) that joins two stiffer materials (fiber layers/adherents). The main differences between these phenomena are the absence of fibers (and its consequences as fiber bridging), the thickness of the joining material (usually the adhesive layer is thicker), and the homogeneity of the joining material (usually the adhesive is uniformly distributed while the composite can present resin rich and resin poor areas).

The different ways the load can be applied to the matrix can impose the cracks to open in different ways. The most important kinds of crack opening for joint applications are Mode I (peeling) and Mode II (sliding shear) [7].

4.3.1 Mode I

Quasi-static Mode I fracture is by far the most studied case for composite delamination failures [13]. The Mode I loading results in a tensile load throughout the matrix. This tensile load produces micro-cracks parallel to (or at small angles from) the fiber layers plane. The growth of these micro-cracks and their coalescence produce the features observed in surface fracture analysis. Besides micro-cracks growth and coalescence, fiber bridging also results in additional features. However, as there is no fibers in adhesive bonding, all mechanisms and features related to fibers will be ignore in this review.

The main features observed in Mode I delamination are textured microflow, scarps and river lines [13–15]. The delamination process starts with the formation of crazes due to the movement of polymeric chains [8]. Under a high tensile stress state, a polymer (matrix) develops crazes, resulting in micro-voids formation on the material (see Fig. 4.1) [13].

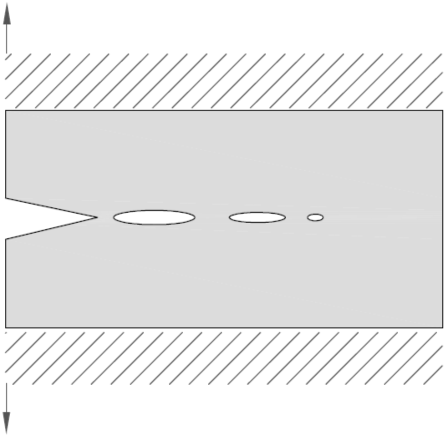

Figure 4.1: *Porosity formation during Mode I crack propagation.*

The next step of the delamination process is the growth of some of the micro-voids created. The textured microflow (see Fig. 4.2), also known as feather pattern, results from this growth. The textured microflow is produced by the local extension of a micro-crack prior to coalescence [14]. As such, it only indicates the local crack growth direction [15] and it can not be related to the global crack growth direction.

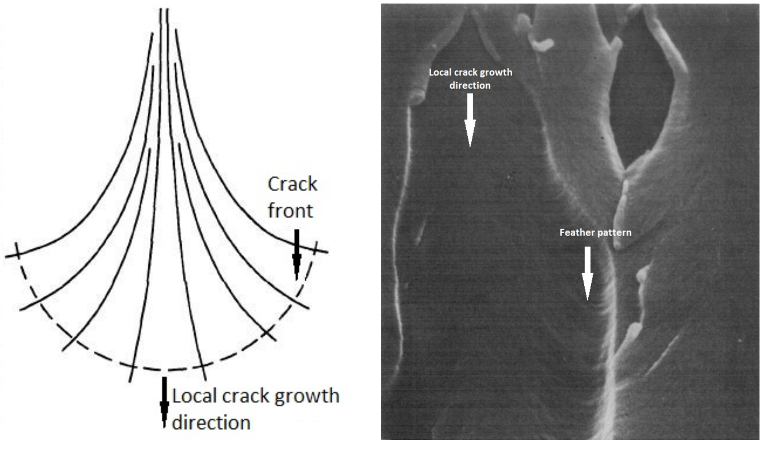

(a) Textured microflow model (b) Textured microflow example

Figure 4.2: *Textured microflow formation in Mode I (adapted from [14]).*

In the sequence of the delamination process, the micro-cracks coalesce generating different features such as scarps or ribbons. Scarps are created by the junction of two adjacent cracks on different planes [14], generating a sharp edge. If, however, the micro-cracks overlap before coalescence they tend to form a ribbon [13].

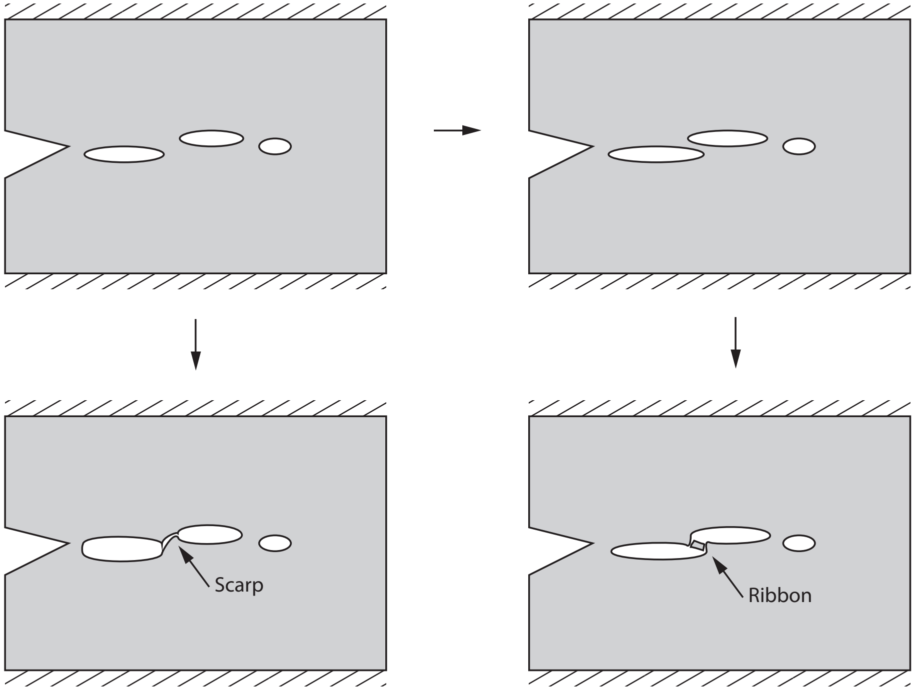

Figure 4.3: *Coalescence of two adjacent micro-cracks and the formation of scarps or ribbons.*

Finally, the coalescence of several micro-cracks tends to form a series of scarps. Under some conditions, these scarps can converge forming river lines. The river lines can be used to determine the global crack growth direction [13, 15], as the failure planes tend to diminish with global crack extension. Consequently, the direction to where the river lines converge indicates the global crack growth direction.

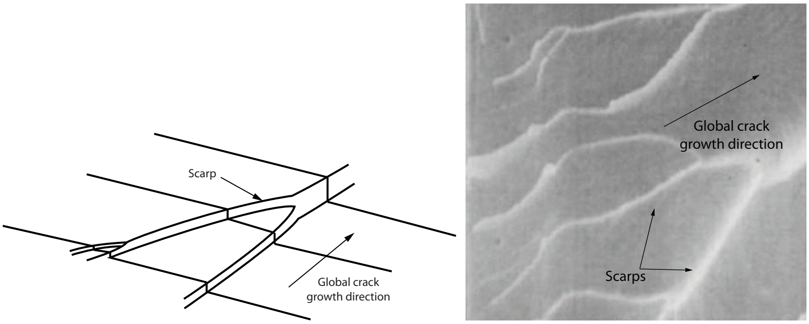

(a) River line formation model, adapted from [13].

(b) River line example, adapted from [14].

Figure 4.4: *River line forms in Mode I as a consequence of the scarps convergence.*

Under fatigue loading, the fracture surfaces present features similar to quasi-static, the main different being the surface roughness. Fatigue delamination presents a smoother fracture surface [9, 10, 15–18]. The reason for the smoother surface is not yet clear. Some researchers [15] suggested that the repetitive contact between the surfaces, which happen in stress ratios close to zero, can modify or destroy some features, resulting in a smoother surface. Other possible explanation is the more efficient crack path under fatigue loading, also resulting in a smoother surface [10, 15].

4.3.2 Mode II

Mode II delamination develops in a similar manner to Mode I. The failure process, for both quasi-static and fatigue loading, starts with the nucleation of micro-cracks ahead of the crack tip. However, the micro-cracks develop not parallel to the fiber layer plane but perpendicular to the principal stress [10, 14, 19], i.e., at an angle of 45^o from the fiber layer plane (see Fig. 4.5). As local Mode I loading generates and grows these micro-cracks, textured microflow can be observed on these regions both in static [13] or fatigue [20] failure.

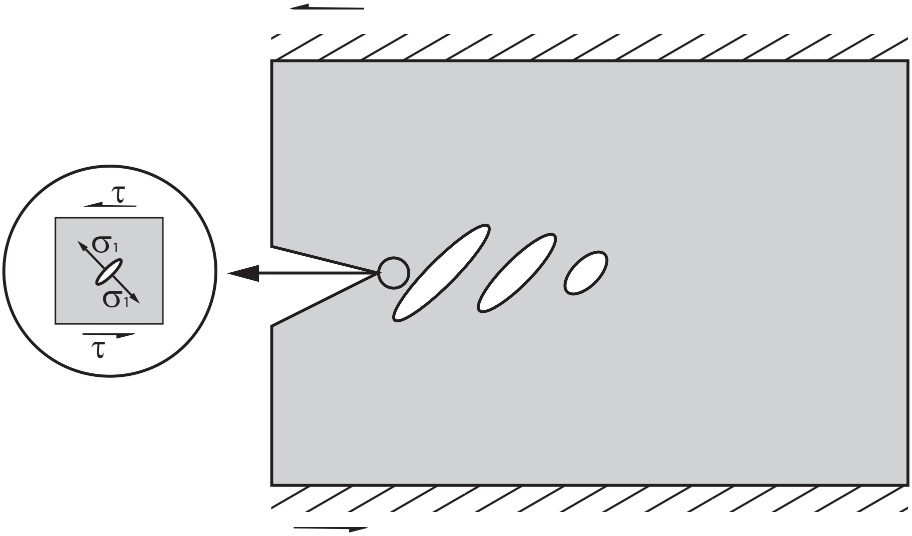

Figure 4.5: *Mode II micro-cracks nucleation and growth under local Mode I loading.*

In the sequence of the failure process, the tilted micro-cracks growth until they reach the limits of the shear band, where the stiffer fibers will deflect the micro-cracks and they will assume an 'S' shape [14]. Next, the micro-cracks coalesce forming the main crack. At this stage, the quasi-static coalescence process differs substantially from the fatigue one. Under quasi-static loading, the micro-cracks coalesce mainly close to one of the adjacent fiber layer, leaving on this layer a series of scallops [13]. On the opposite layer, the fracture surface will be covered by cusps (Fig. 4.6). As for fatigue fractures, the coalescence takes place simultaneously near the two adjacent fiber layers, resulting in a roll of material detached from the matrix [20], called roller.

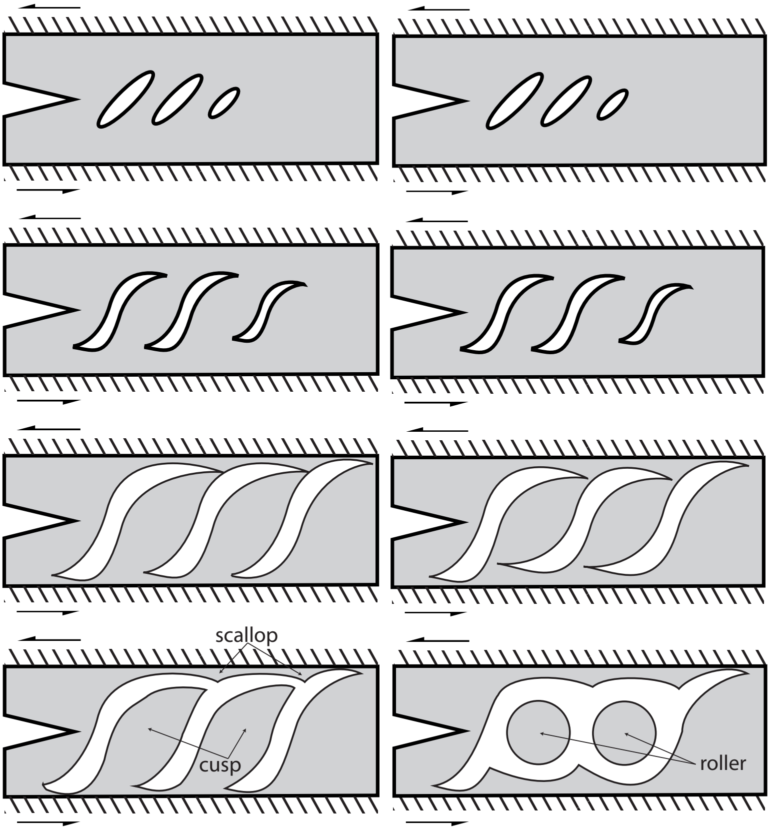

(a) Cusp Model (adapted from [14]) (b) Roller model (adapted from [20])

Figure 4.6: *Roller formation model vs cusp formation model.*

Additionally to rollers, Mode II fatigue delamination surfaces can also present striations [21] and deep striation cracks [17]. However, it is not yet clear if these striations are directly related to a local crack increment per cycle [20], or if they relate to a sudden increment after a number of cycles [13].

Another important feature observed as a result of Mode II quasi-static and fatigue loading is the difference between the fracture surfaces. Usually one of the surfaces presents bare fibers and the opposite surface presents the fibers imprint. This feature is a consequence of the resolved stresses in the matrix layer (Fig. 4.5 and 4.7) [10]. The micro-cracks tend to grow in the direction of the global crack, until the fiber layer deviates the crack and the crack grows in the matrix/fiber vicinity. In an End Notched Flexure (ENF) test, one of the most common for Mode II studies, the delamination grows in the vicinity of the compressive (upper) surface. Then, in an ENF test, the compressive (upper) side presents bare fibers and the tensile (lower) side presents fibers imprints. The nomenclature compressive/tensile will be adopted in this chapter to differentiate both fracture surfaces. However, care must be taken as this nomenclature is valid for ENF and Mixed-Mode Bending Test (MMB) but not for all Mode II and MM specimens.

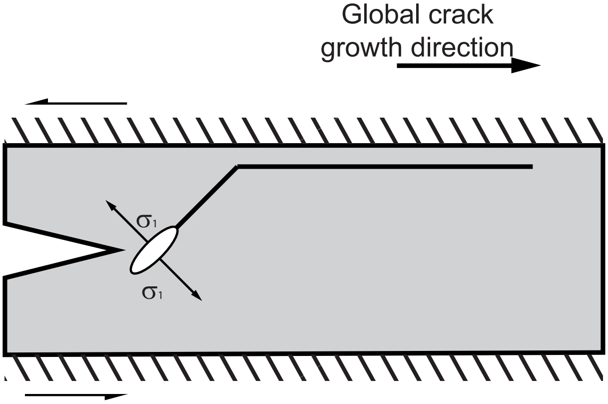

Figure 4.7: *Crack close to the compressive surface.*

4.3.3 Mixed-Mode

The fracture under Mixed-Mode (MM) loading conditions is also characterized by the nucleation and growth of tilted micro-cracks ahead of the crack tip. Similarly to Mode II, the MM loading nucleates tilted micro-cracks, perpendicular to the maximum principal stress [10, 14, 19]. As the Mode II component increases the angle between the micro-cracks and the fibers plane goes from 0° (at pure Mode I) to 45° (at pure Mode II).

Under static loading, the high Mode II fracture surface is similar to a pure Mode II fracture. As the Mode I component increases, the cusps angle becomes smaller [14, 22] until they become shallow steps at high mode I [13]. The shallow steps then become the scarps observed in pure Mode I fracture. This results in the evolution from Mode II to Mode I features observed by several researchers [10, 13, 15, 17, 20, 22–24]. The use of the cusp angle to determine the MR ($MR = \frac{G_{II}}{G_I+G_{II}}$) has been proposed [20] but experimental observations have shown the possibility of post-fracture rotation of the cusp invalidating this relation [13].

Under fatigue loading, the literature presents only a few MR, so a comprehensive analysis is not possible. Still, the MM delamination also exhibits an evolution on the features from pure Mode I to pure Mode II [10, 13, 15, 17, 20, 22, 25, 26]. Cusps can be observed at MR = 25%, at MR=50% one can observe rollers not completely formed and at MR=75% the fracture is already similar to a pure Mode II (MR=100%) [15].

Similarly to pure Mode II, the matching fracture surfaces also present a difference. The Mode II component in the MM deviates the crack path towards the compressive surface in the MMB for both static and fatigue loading [10, 15].

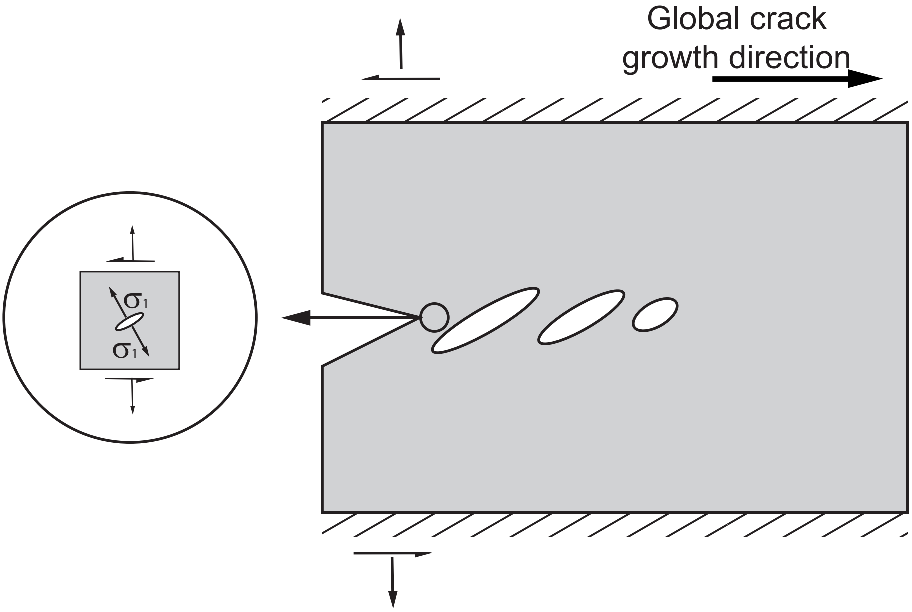

Figure 4.8: *Nucleation and growth of micro-cracks perpendicular to the principal stress.*

4.4 Disbond Growth

4.4.1 Mode I

Similarly to a Mode I delamination, Mode I fatigue disbond on metallic bonded joints is also characterized by the growth and coalescence of micro-cracks ahead of the crack tip. Figure 4.9 shows an example of a fractured surface. One of the most evident feature is the micro-void density in the adhesive. Later comparison with Mode II fatigue disbond (see Fig. 4.11(b)) reveals a smaller micro-void density, indicating the high micro-voids density is not present prior to fracture (as a result of a deficient curing process). Thus, this feature can be considered a strong Mode I characteristic.

Textured microflow (at a higher magnification) and scarps are also observed in Mode I disbond (Fig. 4.9). Ribbons were observed but their incidence was rare. River lines were not observed in any of the Mode I disbond surfaces. One of the probable reasons for the absence of river lines is related to the adhesive thickness. On composites, the matrix layer (where the delamination process occur) is usually thinner than a bond line. As a result, the planes where the micro-cracks develop are closer, resulting in a series of close micro-cracks coalescing and forming river lines. On the other hand, the thicker bond line allows for the micro-cracks to develop at farther planes, generating larger scarps and restraining the occurrence of river lines.

Thus, we can conclude the disbond process occurs following the same sequence as the delamination process: crazing (resulting in micro-voids), micro-cracks growth (resulting in textured micro-flow) and micro-cracks coalescence (resulting in scarps and at a smaller degree in ribbons).

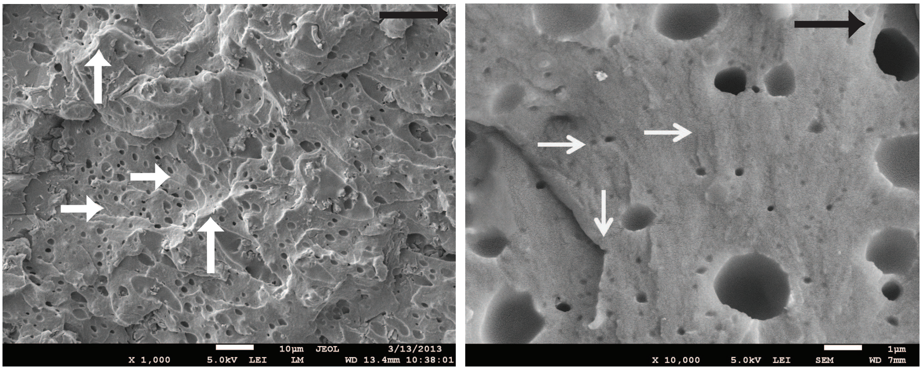

(a) Example of mode I disbond. Vertical white arrows indicate scarps and horizontal white arrows indicate locations with textured microflow.

(b) Detail of mode I disbond. Horizontal white arrows indicate textured microflow in detail and the vertical white arrow indicates a ribbon.

Figure 4.9: *Mode I disbond surface example. Top right black arrow indicates the global crack growth direction.*

4.4.2 Mode II

Mode II fatigue disbond on metallic bonded joints presents most of the Mode II delamination features, such as rollers, deep striation cracks and the crack path close to the compressive surface. Figure 4.10 illustrates the difference between the compressive and the tensile surfaces. In this figure, it is also possible to observe the fabric carrier. The effect of the carrier on the fatigue disbond behavior was evaluated by the author [27] and it will be addressed in the appendix A. Rollers and deep striation cracks can be observed in Fig. 4.11.

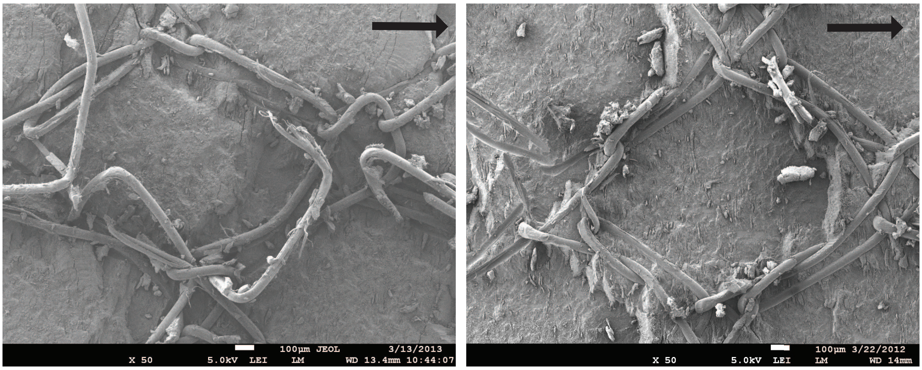

(a) Example of a tensile surface. (b) Example of an compressive surface.

Figure 4.10: *Difference between compressive and tensile surfaces of an ENF specimen (non-matching surfaces). The fracture occurs in the vicinity of the compressive adherend (ENF specimen) resulting in a thick layer of adhesive in the tensile surface.*

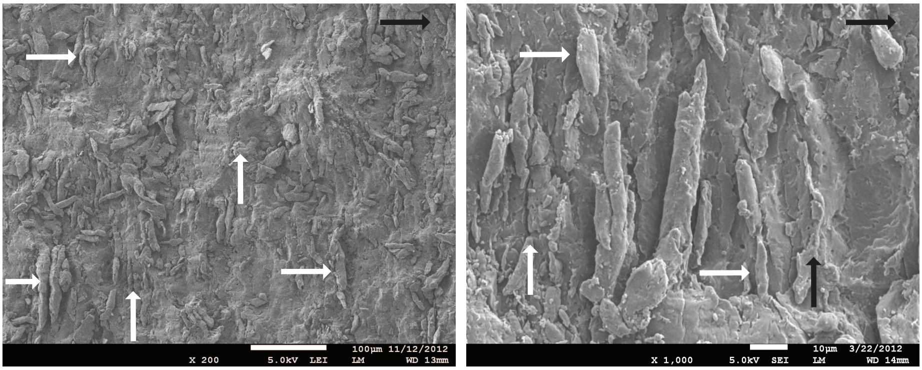

(a) Example of mode II fractography (b) Detail of mode II fractography

Figure 4.11: *Example of tensile surfaces. Mode II features observed: rollers (white horizontal arrows), deep striation cracks (white vertical arrows), scallops (black vertical arrows). The global crack growth direction is indicated by the top right black arrow.*

Observing Fig. 4.10 and 4.11 and comparing the rollers with the rollers formation model [20] (Fig. 4.6) one can observe the roller thickness in adhesive disbond is much smaller (smaller than 10μm) than the expected from the model (approximately the thickness of the shear band, i.e., the bond line thickness, 250μm). Additionally, the rollers formation model [20] would result in symmetrical surfaces, the only difference being the presence of rollers on the tensile surface and its absence on the compressive surface, which is easily disproved by Fig. 4.10. Figures 4.10 and 4.11 indicate the rollers are formed not in the center of the adhesive layer but close to the expected crack path (vicinity of the compressive surface). This indicates a stress concentration effect in the crack tip region that moves the nucleation of micro-cracks from the center of the adhesive layer to the vicinity of the compressive surface.

As a result, a modified mechanism for the roller formation is proposed to account for the stress concentration effect (Fig. 4.12) [27, 28]. The model also explains the deep striation cracks formation as the interception of a tilted micro-crack by the global crack prior to its coalescence into a roller. Adhesive inhomogeneities can cause the micro-cracks to develop at different speeds. So the micro-cracks that develop faster will generate rollers; a part of the micro-cracks will be intercepted by the global crack, generating deep striation cracks; and the slower micro-cracks will likely be hidden under the fracture surface.

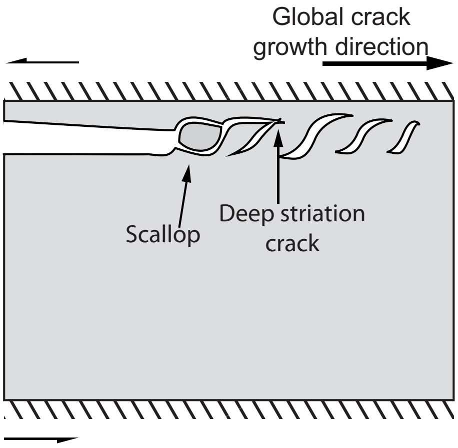

Figure 4.12: *Roller formation model.*

4.4.3 Mixed-Mode

The MM behavior was evaluated from MR=20% to MR=90% in approximately 10% increments. Similarly to pure Mode II fatigue disbond on metallic bonded joints, the crack grew close to the compressive surface for all the MR evaluated. As a result, the tensile surface contains a thick adhesive layer, while the compressive surfaces contains a thin layer of adhesive (Fig. 4.13). Figure 4.13 also shows the presence of the fabric carrier, its effects on the MM fatigue disbond behavior [27] will be addressed in appendix A.

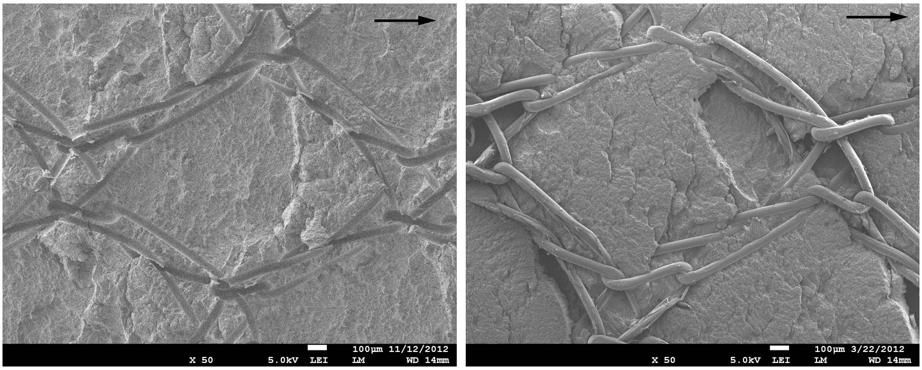

(a) MR=20% compressive surface

(b) MR=40% tensile surface

Figure 4.13: *Examples of crack path on MM loading on non-matching surfaces. Top right arrow indicates the global crack growth direction.*

Mixed-Mode fatigue delamination at high Mode I is characterized by the presence of cusps. However, in fatigue disbond, the tilted micro-cracks do not result in cusps but in tilted layered cracks. At Mode I dominated MRs, the fatigue loading likely nucleates a large number of micro-cracks. A number of them grow and coalesce forming the global crack. Meanwhile, some of the micro-cracks grow and do not coalesce into the global crack but are cut by the global crack generating the tilted layered cracks (Fig. 4.14). Only a few of these micro-cracks are cut by the global crack. As an example, the distance between two adjacent layered cracks range from 20μm to 200 μm, while the distance between two adjacent micro-cracks at pure Mode II (the diameter of a roller) is smaller than 10μm (see Fig. 4.11(b)). This feature is observed in MRs up to 60%.

The tilted micro-cracks which grow and coalesce forming the global crack are responsible for the Mode I features observed. One could argue the surface angle could be measured and the MR deduced from it. Besides the problems of measuring accurately the surface angle, the natural fracture oscillation, caused by defects and non-homogeneities in the adhesive, can overlap the fracture angle. As an example, at MR= 60% the theoretical surface angle is 34° and, in pure Mode I, scarps can present a higher local angle.

Despite the absence of angle measurements, the presence of the tilted layered cracks provides extra-evidence to hypothesis that the local principal stress is the driving force responsible for the micro-crack nucleation and growth [10, 13, 15].

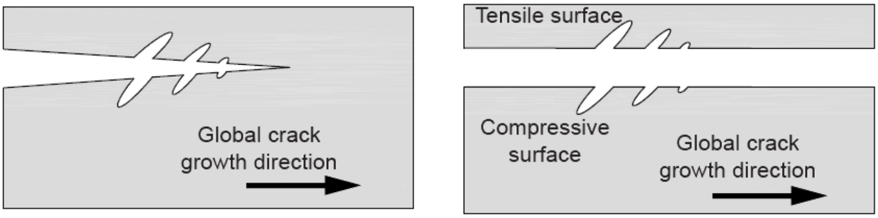

(a) Main crack growing (b) Surfaces separation

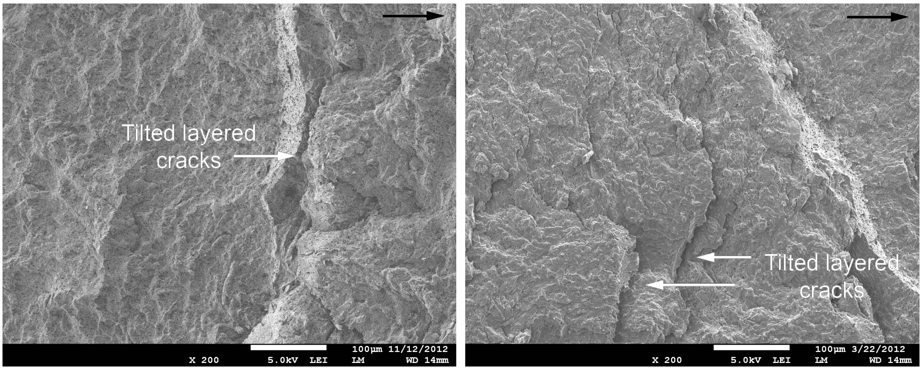

(c) Compressive surface MR=20% (d) Tensile surface MR=40%

Figure 4.14: *Tilted layered cracks model and examples on non-matching surfaces.*

Global Mode I fracture features, such as scarps, can easily be observed in MRs up to 60% (Fig. 4.15(b)). At MR=70% scarps can still be found but their occurrence is rare. From MR=80% and up, there is no evidence of a global Mode I failure, only of local Mode I failure in the scallops (Fig. 4.15(f)). A higher micro-voids density is also related to global Mode I failure. In Fig. 4.15 one can notice the decrease in the micro-void density as the MR increases.

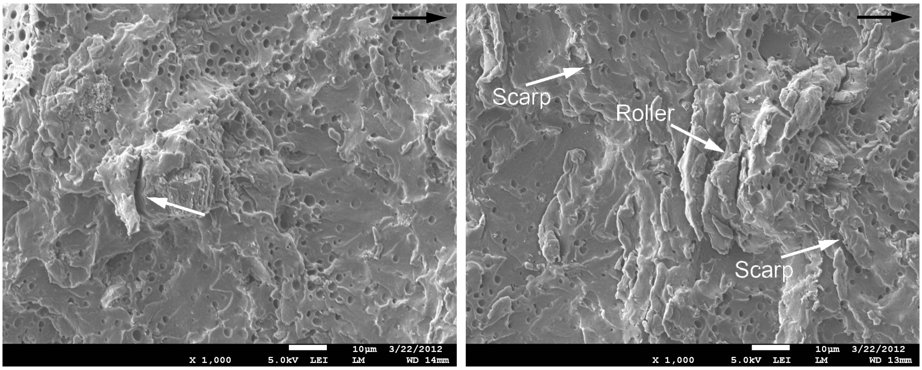

(a) MR=50% - non-detached roller (b) MR=60% - scarps and rollers

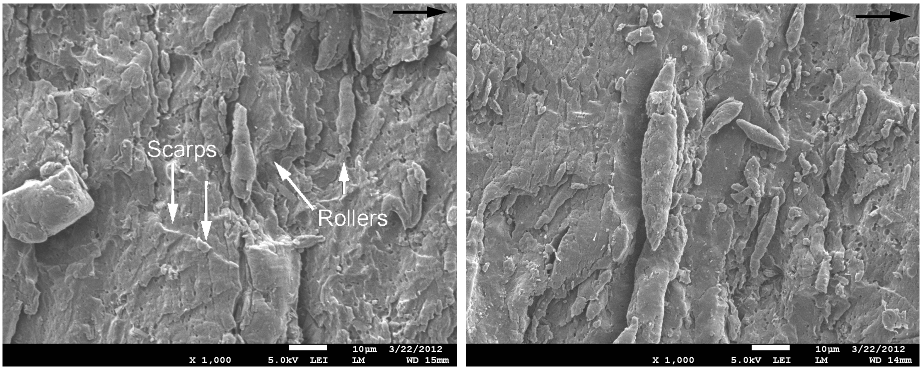

(c) MR=70% - scarps and rollers (d) MR=80%

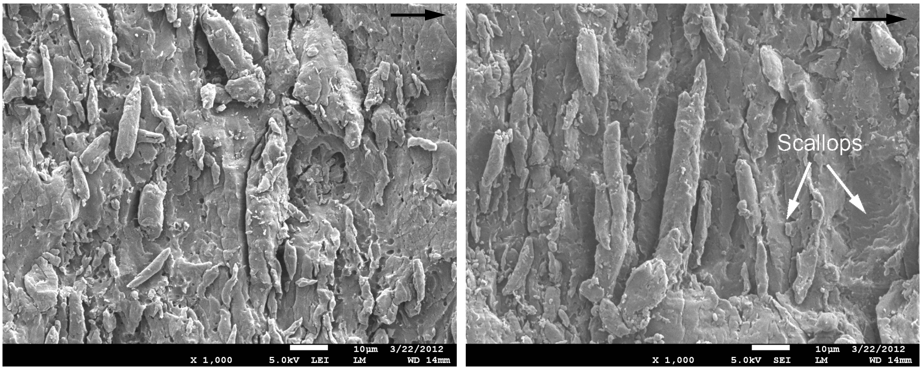

(e) MR=90% (f) MR=100% (Pure Mode II)

Figure 4.15: *Evolution of MM fracture: increasing amount of Rollers and decreasing amount of scarps and porosity with an increasing MR.*

The tilted micro-cracks can coalesce in MM conditions basically in two ways. Under dominated Mode I, the top of one crack will link to the bottom of the next crack, forming a series of aligned scarps with some layered cracks. Under dominated Mode II, the top and bottom of one crack will link, respectively, to the top and bottom of the next, generating rollers (Fig. 4.16).

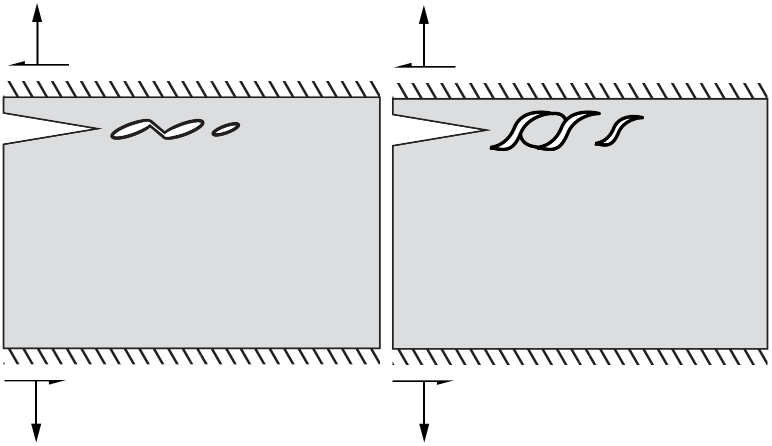

(a) Mode I dominated coalescence (b) Mode II dominated coalescence

Figure 4.16: *Examples of MM coalescence.*

With increasing Mode II, some regions start to present Mode II coalescence. At MR=50%, the first signs of rollers are visible but they are not completely detached from the adhesive (Fig. 4.15(a)). At MR=60%, the first rollers completely detached were observed (Fig. 4.15(b)) but their occurrence was rare and the fracture was still mainly Mode I dominated. At MR=70%, a considerable number of rollers is already seen and the fracture starts to resemble a pure Mode II fracture (Fig. 4.15(c)). At MR=90% (Fig. 4.15(e)) the fracture surface does not present any difference from the pure Mode II (Fig. 4.15(f)). Therefore, the MR controls the coalescence mode and, thus, the energy required for crack extension.

These results are in accordance with the literature [15], which presents a fracture at MR=75% already Mode II dominated but with a fewer rollers than a pure Mode II fracture. In addition, at MR=50% one can observe only not completely formed rollers [15].

4.5 Conclusions

This chapter investigated the Mixed-Mode fatigue disbond failure mechanisms on a metallic bonded joint. The main conclusions obtained are listed below.

- The global crack path is dominated by Mode II loading and even small Mode II contributions (the minimum MR evaluated was 20%) can drive the crack towards the compressive surface.
- The failure mechanisms present an evolution from MR=0% (pure Mode I) to MR=100% (pure Mode II) in the following sequence: presence of scarps (MR=0%), alignment of scarps and occurrence of tilted layered cracks

(MR=20%), non-completely detached rollers (MR=50%), first completely detached rollers and end of tilted layered cracks (MR=60%), rarity of scarps and appearance of a large number of rollers (MR=70%), fracture similar to a pure Mode II (MR=90%).

- The micro-void density observed in the fracture surface decreases with increasing Mode II loading.
- The principal stress, which results in local Mode I loading, controls the beginning of the failure process.
- The MR controls the micro-cracks coalescence mode.

Therefore, the principal stress is the driving force for micro-crack nucleation and growth under MM fatigue loading and the MR controls the micro-cracks coalescence mode, i.e., the amount of energy that is consumed for crack extension. Consequently, a MM fatigue disbond model accounting mainly for these two parameters should be able to yield good estimates.

References

[1] P. T. Cheuk, L. Tong, C. H. Wang, A. Baker, and P. Chalkley. Fatigue crack growth in adhesively bonded composite-metal double-lap joints. *Composite Structures*, 57(1-4):109–115, 2002.

[2] T.T. Khoo and H. Kim. Effect of bondline thickness on mixed-mode fracture of adhesively bonded joints. *Journal of Adhesion*, 87(10):989–1019, 2011.

[3] F. Moroni and A. Pirondi. A procedure for the simulation of fatigue crack growth in adhesively bonded joints based on the cohesive zone model and different mixed-mode propagation criteria. *Engineering Fracture Mechanics*, 78(8):1808–1816, 2011.

[4] I.A. Ashcroft, V. Shenoy, G.W. Critcholow, and A.D. Crocombe. A comparison of the prediction of fatigue damage and crack growth in adhesively bonded joints using fracture mechanics and damage mechanics progressive damage methods. *The Journal of Adhesion*, 86(12):1203–1230, 2010.

[5] N.D. Datla, M. Papini, J.A. Schroeder, and J.K Spelt. Modified DCB and CLS specimens for mixed-mode fatigue testing of adhesively bonded thin sheets. *International Journal of Adhesion & Adhesives*, 30(6):439–447, 2010.

[6] N. Choupani. Interfacial mixed-mode fracture characterization of adhesively bonded joints. *International Journal of Adhesion & Adhesives*, 28(6):267–282, 2008.

[7] J. Schijve. *Fatigue of Structures and Materials.* Kluwer Academic, Dordrecht, Boston, 2004.

[8] A. Mouritz. *Introduction to Aerospace Materials.* Woodhead publishing in materials. Elsevier Science, 2012.

[9] R. A. Kline and F. H. Chang. Composite failure surface analysis. *Journal of Composite Materials*, 14:315–324, 1980.

[10] S. Singh and E. Greenhalgh. Micromechanics of interlaminar fracture in carbon fibre reinforced plastics at multidirectional ply interfaces under static and cyclic loading. *Plastics, Rubber and Composites Processing and Applications*, 27(5):220–226, 1998.

[11] A. Argüelles, J. Viña, A. F. Canteli, and J. Bonhomme. Influence of resin type on the delamination behavior of carbon fiber reinforced composites under mode-II loading. *International Journal of Damage Mechanics*, 20(7):963–978, 2011.

[12] G. Allegri, M. R. Wisnom, and S. R. Hallett. A new semi-empirical law for variable stress-ratio and mixed-mode fatigue delamination growth. *Composites Part A: Applied Science and Manufacturing*, 48(1):192–200, 2013.

[13] E.S. Greenhalgh. *Failure Analysis and Fractography of Polymer Composites*. Woodhead Publishing in materials. Woodhead Publishing, Cambridge - UK, 2009.

[14] D. Purslow. Matrix fractography of fibre-reinforced epoxy composites. *Composites*, 17(4):289–303, 1986.

[15] M. J. Hiley. Fractographic study of static and fatigue failures in polymer composites. *Plastics, Rubber and Composites Processing and Applications*, 28(5):210–227, 1999.

[16] H. Masaki, O. Shojiro, C. . Gustafson, and T. Keisuke. Effect of matrix resin on delamination fatigue crack growth in CFRP laminates. *Engineering Fracture Mechanics*, 49(1):35–47, 1994.

[17] A. Sjögren, L. E. Asp, E. S. Greenhalgh, and M. J. Hiley. Interlaminar crack propagation in CFRP: Effects of temperature and loading conditions on fracture morphology and toughness. In *ASTM Special Technical Publication*, pages 235–252, 2002.

[18] M. Hojo, T. Ando, M. Tanaka, T. Adachi, S. Ochiai, and Y. Endo. Modes I and II interlaminar fracture toughness and fatigue delamination of CF/epoxy laminates with self-same epoxy interleaf. *International Journal of Fatigue*, 28(10):1154–1165, 2006.

[19] R. E. Robertson and V. E. Mindroiu. The stacked lamellar texture on the fracture surfaces of fibre composites. *Journal of Materials Science*, 20(8):2801–2806, 1985.

[20] F. Heutling, H. E. Franz, and K. Friedrich. Microfractographic analysis of delamination growth in fatigue loaded - carbon fibre/thermosetting matrix composites. *Materialwissenschaft und Werkstofftechnik*, 29(5):239–253, 1998.

[21] G. C. Shih and L. J. Ebert. The effect of the fiber/matrix interface on the flexural fatigue performance of unidirectional fiberglass composites. *Composites Science and Technology*, 28(2):137–161, 1987. Cited By (since 1996): 23.

[22] S. Zhao, M. Gadke, and R. Prinz. Mixed-mode delamination behavior of carbon/epoxy composites. *Journal of Reinforced Plastics and Composites*, 14(8):804–826, 1995.

[23] S. Singh and I.K. Partridge. Mixed-mode fracture in an interleaved carbon-fibre/epoxy composite. *Composites Science and Technology*, 55(4):319–327, 1995.

[24] E. S. Greenhalgh and S. Singh. The effect of moisture, matrix and ply orientation on delamination resistance, failure criteria and fracture morphology in CFRP. In *ASTM Special Technical Publication*, pages 221–234, 2002.

[25] L. E. Asp, A. Sjgren, and E. S. Greenhalgh. Delamination growth and thresholds in a carbon/epoxy composite under fatigue loading. *Journal of Composites Technology and Research*, 23(2):55–68, 2001.

[26] N. Blanco, E.K. Gamstedt, L.E. Asp, and J. Costa. Mixed-mode delamination growth in carbon-fibre composite laminates under cyclic loading. *International Journal of Solids and Structures*, 41(15):4219–4235, 2004.

[27] D. Bürger, C. D. Rans, and R. Benedictus. Influence of fabric carrier on the fatigue disbond behavior of metal-to-metal bonded interfaces. *The Journal of Adhesion*, 90(5-6):482–495, 2014.

[28] D. Bürger, C. D. Rans, and R. Benedictus. Characterization of mixed-mode fatigue failure on metallic bonded joints. In *ICAF 2013 Symposium - Proceedings of the 27th Symposium of the International Committee on Aeronautical Fatigue*, pages 751–760, 2013.

5 Model Development

5.1 Introduction

The experimental results presented in Chap. 3 have shown that the available models in the literature can not predict accurately the Mixed-Mode (MM) fatigue disbond based only on pure Mode I and pure Mode II fatigue disbond data. In an attempt to improve the MM predicitons, Chapter 4 presented a study of the MM fatigue disbond mechanisms.

This chapter attempts to understand the influence of the disbond mechanisms identified previously on the macro-crack growth and to develop a new MM fatigue disbond model that considers these influences.

5.2 Disbond Process

Based on the discussion of the previous chapter (Chap. 4), the disbond can be divided into three different mechanisms: micro-crack nucleation, micro-crack growth and micro-crack coalescence. First a local tensile stress state nucleates micro-cracks ahead of the crack tip, followed by a micro-crack extension to accommodate the stresses, and, when they reach a critical size, the micro-cracks coalesce.

The previous chapter has shown evidence, in accordance with the literature, that the two first mechanisms are controlled by the local principal stress, as the micro-cracks nucleate and grow in an plane inclined with respect to the main crack growth direction. The coalescence, however, is controlled by the Mode Ratio (MR). The lower the MR (MR=0 stands for pure Mode I), the more the micro-cracks develop parallel to the main crack growth direction. The higher the MR (MR=1 stands for pure Mode II), the more the micro-cracks develop at a 45^o angle from the main crack growth direction.

The different coalescence modes (see Fig. 5.1) depend directly on the angle the micro-cracks develop. As the micro-cracks angle is controlled by the MR, the area created in the coalescence process is a function of the MR. And, thus, the energy required for coalescence is dominated by the MR. A lower MR implies less area created for joining two adjacent micro-cracks and thus, less energy required in this process. A higher MR implies more area created resulting in more energy required in the process. This explains why the high mode I fatigue disbond occurs at lower load levels than the high mode II fatigue disbond (see Fig. 3.10).

The coalescence can be divided into two process: the coalescence between two micro-cracks, which results in a larger micro-crack ahead of the main crack tip; and the coalescence between a micro-crack and the main crack, which results in an increment of

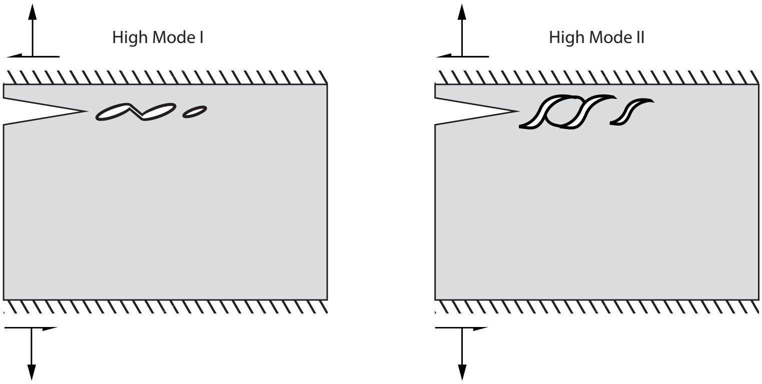

Figure 5.1: *Different coalescence modes. High Mode II coalescence creates a larger fracture surface area.*

the main crack. The combination of the disbond mechanisms (micro-crack nucleation, growth and coalescence) implies in a certain number of cycles with no crack increment (only micro-crack nucleation and growth, and coalescence between micro-cracks) and a sudden crack increment in a specific cycle (coalescence of a micro-crack with the main crack). However, for modeling purposes, the micro-cracks ahead of the crack tip are ignored and an average macro crack increment per cycle is assumed [1–17].

The differences between the modeling assumptions (continuous crack increment per cycle) and the failure mechanisms explained above could result in an inconsistency between the experimental results and the model predictions. However, the average increment per cycle can represent reasonably the global disbond behavior given a sufficient number of cycles. As fatigue is a long term phenomenon, this assumption usually does not affect the models.

The principal stress has been identified as the driving force of two failure mechanisms (micro-crack nucleation and growth), thus, it may be a more appropriate parameter to represent the fatigue crack growth data. Stress calculation in a layered material poses more complications than in an isotropic material. Thereby, an alternative solution is to represent the stress as a function of Strain Energy Release Rate (SERR).

5.3 Principal stress calculation

In order to calculate the principle stress at the crack tip one can first approximate the stress field in the adhesive layer to the stress field in a plate with a crack, calculated by the Westergaard method. Later, with the stress field at the crack tip (σ_x, σ_y and τ_{xy}), the principal stress can be obtained using the Mohr's circle.

The stress field on the crack tip is calculated assuming an infinite sheet subjected to a constant load. Thus, applying equations derived with these assumptions to a disbond phenomenon can present some limitations. Specially in the presence of Mode II loading, the crack does not grow in the center of the adhesive, what would present more similarities with the infinite sheet assumption. Under Mode II loading, the crack grows close to the compressive adherent, where the adherent's higher stiffness is responsible for deflecting the crack. However, at a micro-level, there is evidence that the adherent does not affect the micro-crack nucleation and growth mechanisms (see Chap. 4).

The constant load assumption this infinite sheet is subjected to should not present further implications in a fatigue problem. During fatigue crack growth, at a constant displacement, the crack increment should result in a load decrease. However, the crack increment on one cycle is usually small (fatigue is a long term phenomenon) and so the load decrease is usually small.

The stress field calculated with the Westergaard method for a material with a crack under Mode I loading is given by [18]:

$$\sigma_x = \frac{K_I}{\sqrt{2\pi r}} cos\frac{\theta}{2}\left[1 - sin\frac{\theta}{2}sin\frac{3\theta}{2}\right] + \sigma_{x0} + O(r^{1/2}) \tag{5.1}$$

$$\sigma_y = \frac{K_I}{\sqrt{2\pi r}} cos\frac{\theta}{2}\left[1 + sin\frac{\theta}{2}sin\frac{3\theta}{2}\right] + O(r^{1/2}) \tag{5.2}$$

$$\tau_{xy} = \frac{K_I}{\sqrt{2\pi r}} sin\frac{\theta}{2}cos\frac{\theta}{2}cos\frac{3\theta}{2} + O(r^{1/2}) \tag{5.3}$$

and under Mode II loading:

$$\sigma_x = -\frac{K_{II}}{\sqrt{2\pi r}} sin\frac{\theta}{2}\left[2 + cos\frac{\theta}{2}cos\frac{3\theta}{2}\right] + \sigma_{x0} + O(r^{1/2}) \tag{5.4}$$

$$\sigma_y = \frac{K_{II}}{\sqrt{2\pi r}} sin\frac{\theta}{2}cos\frac{\theta}{2}cos\frac{3\theta}{2} + O(r^{1/2}) \tag{5.5}$$

$$\tau_{xy} = \frac{K_{II}}{\sqrt{2\pi r}} cos\frac{\theta}{2}\left[1 - sin\frac{\theta}{2}sin\frac{3\theta}{2}\right] + O(r^{1/2}) \tag{5.6}$$

Where θ and r are shown in Fig. 5.2.

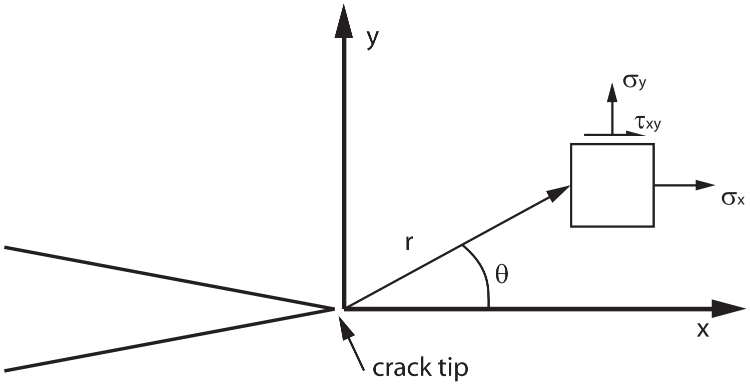

Figure 5.2: *Stress components in the crack tip stress field.*

Thus, considering no stress parallel to the crack ($\sigma_x = 0$) and no terms of the order of square root of r ($O(r^{1/2}) = 0$), the stresses can be described as:

$$\sigma_y = \frac{K_I}{\sqrt{2\pi r}} cos\frac{\theta}{2}\left[1 + sin\frac{\theta}{2} sin\frac{3\theta}{2}\right] + \frac{K_{II}}{\sqrt{2\pi r}} sin\frac{\theta}{2} cos\frac{\theta}{2} cos\frac{3\theta}{2} \tag{5.7}$$

$$\tau_{xy} = \frac{K_I}{\sqrt{2\pi r}} sin\frac{\theta}{2} cos\frac{\theta}{2} cos\frac{3\theta}{2} + \frac{K_{II}}{\sqrt{2\pi r}} cos\frac{\theta}{2}\left[1 - sin\frac{\theta}{2} sin\frac{3\theta}{2}\right] \tag{5.8}$$

The micro-cracks tend to develop in a region close to the crack tip plane, where $\theta \to 0$. Then, Eqs. 5.7 and 5.8 can be re-written as:

$$\sigma_y = \frac{K_I}{\sqrt{2\pi r}} \tag{5.9}$$

$$\tau_{xy} = \frac{K_{II}}{\sqrt{2\pi r}} \tag{5.10}$$

Similarly to the calculation of stresses, the calculation of stress intensity factors (K_I and K_{II}) in a layered material can present mathematical complexities. Therefore, the concept of Strain Energy Release Rate can be used to overcome this hindrance.

A structure stores potential energy in the form of elastic strain when loaded (Eq. 5.11). If the structure has a cracked area (A) and this crack extends by a small increment (dA), the structure stiffness diminishes resulting in less stored energy. The rate at which the energy stored diminishes (Fig. 5.3) for a crack increment is called SERR and denoted by G (Eq. 5.12).

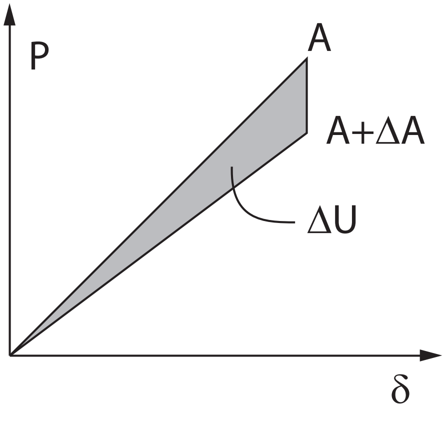

Figure 5.3: *Strain energy loss resulting from crack increment.*

$$U = \frac{1}{2} P\delta \tag{5.11}$$

$$G = \frac{\partial U}{\partial A} = \frac{P^2}{2}\frac{\partial C}{\partial A} \tag{5.12}$$

Where: P is the load, δ is the displacement at the loading point, A is the crack area and $C = \delta/P$ is the compliance of the structure. If the energy is absorbed only to create new surfaces, then this variable can be related to crack growth. If there are other mechanisms absorbing a large amount of energy, e.g. plasticity, this concept may not hold true.

Particularly to the disbond phenomenon, the use of SERR results in the requirement of no plastic deformation in the adherend. Small scale yielding on the adhesive, however, can not be avoided. But the amount of energy employed of adhesive yielding is much smaller compared to the energy employed for crack extension. Additionally, it can be argued that the small scale yielding is a stage of the failure mechanism, and thus, should be included in the energy required for failure.

The SERR can be related to the stress intensity factor through [18]:

$$\begin{aligned} G_I &= K_I^2/E^* \\ G_{II} &= K_{II}^2/E^* \end{aligned} \tag{5.13}$$

Where

$$\begin{aligned} &E^* = E \text{ (plane stress)} \\ &or \\ &E^* = E/(1-\nu^2) \text{ (plane strain)} \end{aligned} \tag{5.14}$$

Therefore, the stresses can be expressed as:

$$\sigma_y = \sqrt{G_I}\frac{\sqrt{E^*}}{\sqrt{2\pi r}} = \sqrt{G_I}.\beta \tag{5.15}$$

$$\tau_{xy} = \sqrt{G_{II}}\frac{\sqrt{E^*}}{\sqrt{2\pi r}} = \sqrt{G_{II}}.\beta \tag{5.16}$$

Once the stresses on the crack tip are available the Mohr's circle can be used to obtain the principal stress. The Mohr's circle is a geometrical method to easily calculate the stresses in any plane given the stresses on a particular plane [19]. For the disbond case ($\sigma_x = 0$) the circle is represented in Fig. 5.4. According to this method, the angle of the principal stress and the principal stress are given by:

$$\alpha = \frac{1}{2}atan\Big(\frac{2\tau_{xy}}{\sigma_y - \sigma_x}\Big) \tag{5.17}$$

$$\sigma_1 = \frac{\sigma_x + \sigma_y}{2} + radius \tag{5.18}$$

Where,

$$radius = \sqrt{(\tau_{xy})^2 + \Big(\frac{\sigma_y - \sigma_x}{2}\Big)^2} \tag{5.19}$$

As a result, applying Eqs. 5.15 and 5.16 on Eqs. 5.17 and 5.18 one can obtain:

$$\alpha = \frac{1}{2}atan\Big(\frac{2\sqrt{G_{II}}}{\sqrt{G_I}}\Big) \tag{5.20}$$

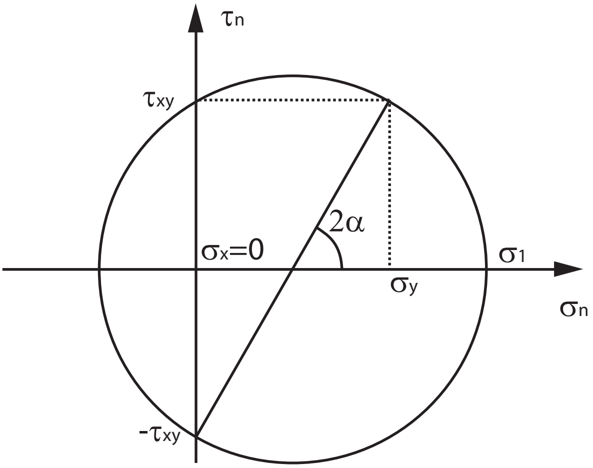

Figure 5.4: *Mohr's circle for $\sigma_x = 0$.*

$$\sigma_1 = \beta.\frac{\sqrt{GI}}{2} + \beta.\sqrt{G_{II} + \frac{G_I}{4}} \tag{5.21}$$

Equations 5.20 and 5.21 assume $\theta = 0$ (see Fig.5.2). For a pure Mode I loading, this assumption is reasonable as the crack should develop in the region of $\theta \to 0$. If, however, there is a Mode II component, the micro-cracks should grow in an angle and, therefore, $\theta \neq 0$.

If this assumption is ignored the principal stress and the principal stress angle are functions of θ and they can be obtained by substituting Eqs. 5.7 and 5.8 on Eqs. 5.17 and 5.18.

Figures 5.5 and 5.6, show the effect of the angle θ on the angle of the principal stress (α) and on the principal stress (σ_1). As can be seen in both figures, the influence of θ depends on the MR. The effect of θ on α is limited and in most cases inferior to 10^o.

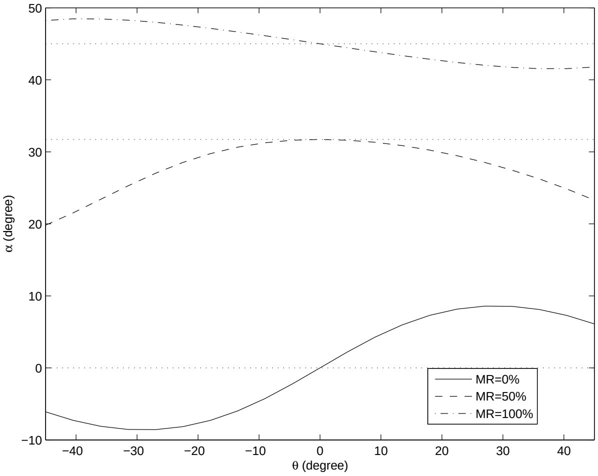

Figure 5.5: *Effect of the angle θ on the principal stress angle (α). The dotted line represents the expected value of α for $\theta = 0$.*

The effect of θ on σ_1 can be significant. Particularly for $\theta > 30^o$ and for $\theta < -20^o$ the error can be higher than 20% (Fig. 5.6). However, these higher angles do not occur on the nucleation and micro-crack growth phase, only at the coalescence phase (see Fig. 5.7). Thus, the errors caused by the assumption of $\theta = 0$ are limited.

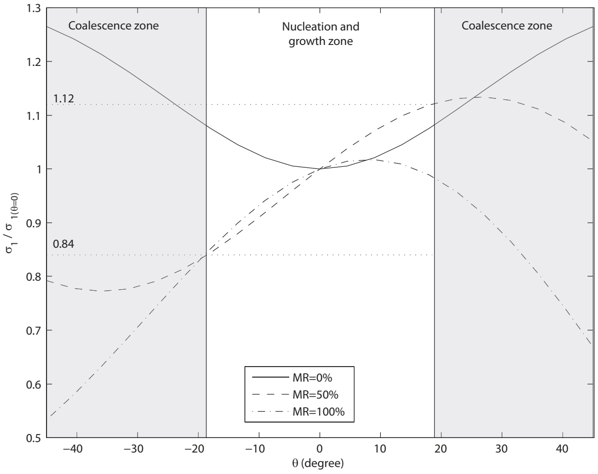

Figure 5.6: *Effect of the angle θ on the principal stress (σ_1).*

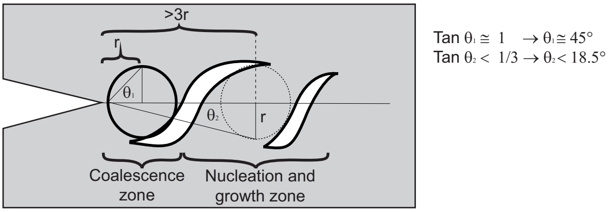

Figure 5.7: *Analysis of θ on the nucleation and growth zone and on the coalescence zone.*

Thus, with the principal stress described as a function of G_I and G_{II}, a Mode I SERR in the principal stress direction can be written as:

$$\sqrt{G_1^*} = \left[\frac{\sqrt{G_I}}{2} + \sqrt{\frac{G_I}{4} + G_{II}} \right] .\beta \tag{5.22}$$

As the Paris relation is represented as

$$\frac{da}{dN} = C^*.\Big((\sqrt{G_{1\_max}^*} - \sqrt{G_{1\_min}^*})^2 \Big)^m = C^*(\Delta\sqrt{G_1^*})^m \tag{5.23}$$

If an equivalent Mode I SERR in the principal stress direction is defined as:

$$\sqrt{G_{1\_eq}} = \frac{\sqrt{G_I}}{2} + \sqrt{\frac{G_I}{4} + G_{II}} \tag{5.24}$$

The Paris relation can be represented as:

$$\frac{da}{dN} = C.\Big((\sqrt{G_{1\_eq\_max}} - \sqrt{G_{1\_eq\_min}})^2 \Big)^m = C(\Delta\sqrt{G_{1\_eq}})^m \tag{5.25}$$

where:

$$C = C^*.\beta^{2.m} \tag{5.26}$$

Figure 5.8 shows the experimental results from Chap. 3 as a function of the principal stress. Observing this figure, one could argue that, as the principal stress is the driving force controlling the disbond process, the data from different MR ratios should collapse to a single trend. However, it must be remembered that the principal stress controls only a part of the process. And the energy required to coalesce the micro-cracks depends on the MR. This can explain the collapse between the 75% and 100% data. As, from Fig. 4.15 in Chap. 4, there is little difference between the fracture surface of 70%, 80%, 90% and 100%, indicating similar coalescence process at these MRs and, thus, a similar amount of energy required to coalesce the micro-cracks.

Figure 5.8 also indicates that the exponents of the Paris relation for all MRs are similar. Table 5.1 presents the Paris relation coefficients. From Tab. 5.1 one can confirm that the exponent m is indeed similar for the different MRs. The exception would be the pure Mode II data. However, the literature has reported that obtaining

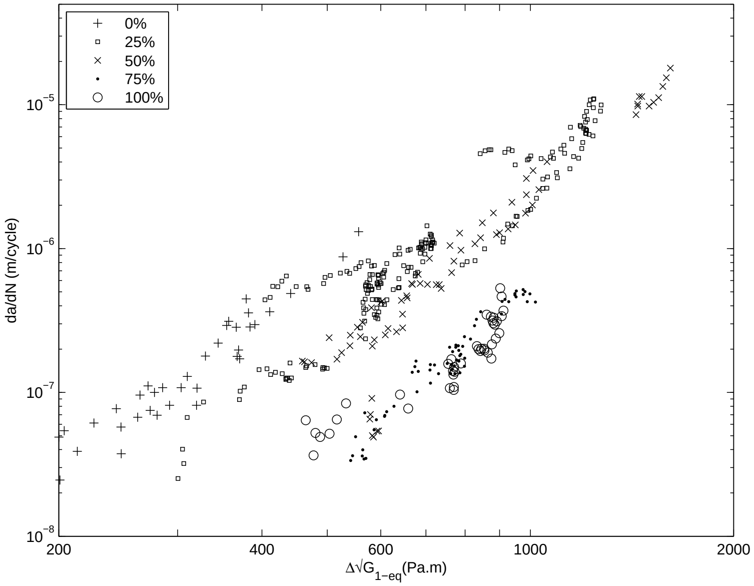

Figure 5.8: *Fatigue crack growth behavior as a function of principal stress.*

the Mode II data can be problematic [20]. Additionally, there are reports that different test setups can yield different results for static failure [20]. Consequently, they might also have an influence on the fatigue results.

Table 5.1: *Fit coefficients for experimental results from Chap. 3.*

MR	C	m
0%	$5.27\ 10^{-17}$	3.78
25%	$9.58\ 10^{-18}$	3.85
50%	$3.87\ 10^{-18}$	3.93
75%	$8.80\ 10^{-19}$	3.93
100%	$2.23\ 10^{-24}$	5.81

5.3.1 Principal stress projection

The use of the principal stress to describe the fatigue disbond growth also raises the question that the disbond increment per cycle (da/dN) is the projection of an inclined disbond increment (Fig. 5.9). I.e., the Paris relation would be a relation from $\Delta\sqrt{G_{1\_eq}}$ and an inclined da/dN, that is later projected in the direction of macro disbond growth generating the disbond growth that is measured.

$$\left.\frac{da}{dN}\right)_{inclined}.cos(\alpha) = \left.\frac{da}{dN}\right)_{projection} \tag{5.27}$$

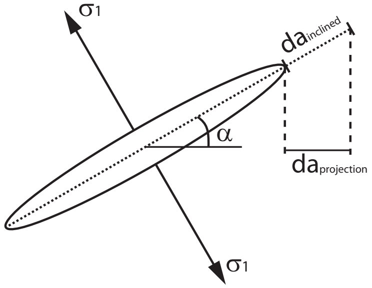

Figure 5.9: *Crack increment projection.*

$$\left.\frac{da}{dN}\right)_{inclined} = C.(\Delta\sqrt{G_{1\_eq}})^m \tag{5.28}$$

$$\left.\frac{da}{dN}\right)_{projection} \frac{1}{cos(\alpha)} = C.(\Delta\sqrt{G_{1\_eq}})^m \tag{5.29}$$

According to this principle, the correct description of the fatigue disbond growth behavior should be represented in a graph of $\Delta\sqrt{G_1}$ vs $da/dN/cos(\alpha)$, as in Fig. 5.10. Comparing Figs. 5.8 and 5.10, one can observe that there is nearly no differences between them and the α correction can not collapse the experimental points. Despite the reasoning for using this correction term, one must remember the different coalescence modes for different MRs, which requires different levels of energy. Additionally, one can argue that the parameter C already takes into account the value of $cos(\alpha)$. As a result, a model that includes C will indirectly consider the effect of α.

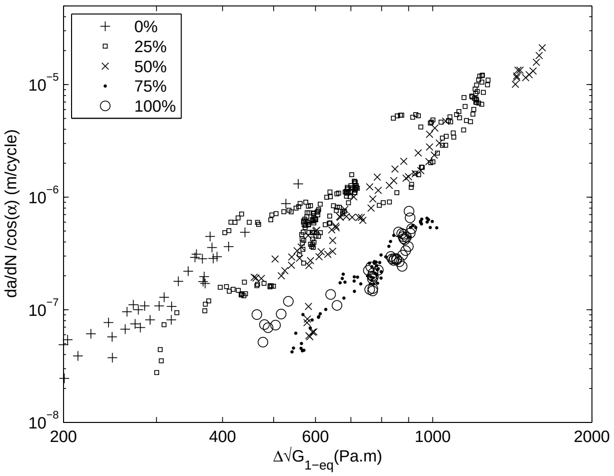

Figure 5.10: *Fatigue crack growth behavior as a function of principal stress with the correction for the angle α.*

5.4 Model Development

Observing the similarity between the exponents m in Tab. 5.1, one could consider that they assume a fixed value, independently of the MR. This would lead to a change in the coefficient C. But then, this coefficient would be a function only of the MR. If one fixes the exponent as $m = m_{0\%}$. The new coefficients C obtained are presented in Fig. 5.11 with a confidence interval of 95%. Details on the calculation of the coefficient C for a fixed m and the confidence intervals can be found in Appendix B.

Observing Fig. 5.11, one can obtain a good approximation of the coefficient C by interpolating the values of log(C) with a straight line between MR=0 and MR = 100%. Considering this approximation, one can predict the disbond crack growth for the entire range of MRs based only on pure Mode I and pure Mode II data.

Based on this assumption, the predictions for the set of experiments MM - FCG from Chap. 3 are presented in Fig. 5.12 and for the set of experiments MM - fracture surface are presented in Fig. 5.13.

Observing these predictions, one can notice the good agreement between the model predictions and the experimental values, particularly in the 20% - 50% MR range. For higher MRs, the model overpredicts the experimental results. The explanation for the overpredictions can be found in the in Fig. 5.11, where the model predicts with accuracy the value of C for MR=25% and 50% and it predicts a higher C for MR=75%. Moreover, Fig. 5.11 indicates a similar C for MR between 75% and 100%, which results in over predictions in this range, what is confirmed by Fig. 5.13.

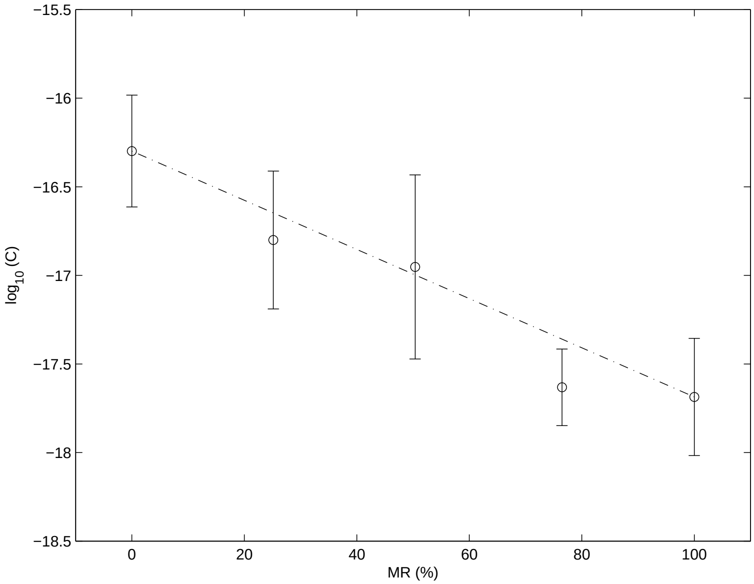

Figure 5.11: *Effect of a constant m on the coefficient C.*

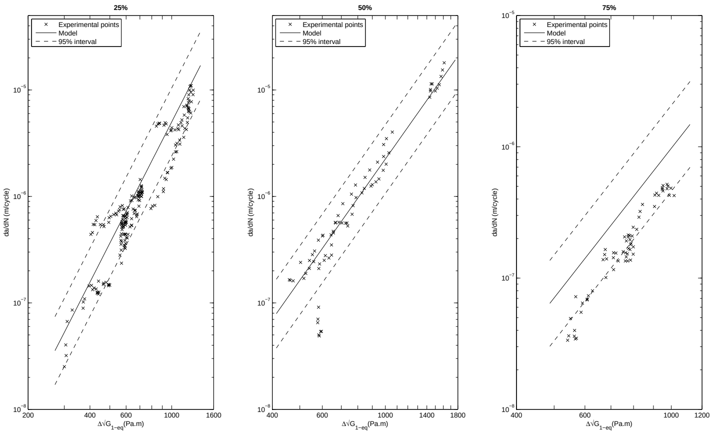

Figure 5.12: *Model predictions for the MM - FCG set of data.*

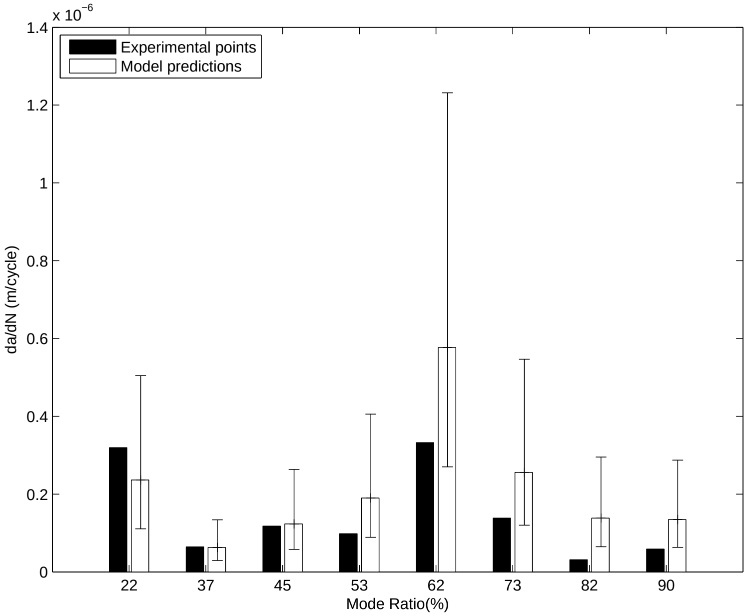

Figure 5.13: *Model predictions for the MM - fracture surface set of data.*

5.5 Model Summary

The implementation of the model can be done following the steps:

1. Calculation of the equivalent principal stresses in terms of SERR;

$$\sqrt{G_{1\_eq\_max}} = \frac{\sqrt{G_{I\_max}}}{2} + \sqrt{\frac{G_{I\_max}}{2} + G_{II\_max}} \tag{5.30}$$

$$\sqrt{G_{1\_eq\_min}} = \frac{\sqrt{G_{I\_min}}}{2} + \sqrt{\frac{G_{I\_min}}{2} + G_{II\_min}} \tag{5.31}$$

$$\Delta\sqrt{G_{\_eq1}} = (\sqrt{G_{1\_eq\_max}} - \sqrt{G_{1\_eq\_min}})^2 \tag{5.32}$$

2. Plot the da/dN vs $\Delta\sqrt{G_{1\_eq}}$ for the Mode I and the Mode II data;
3. Determination of the Mode I fit parameters ($C_{0\%}$ and $m_{0\%}$);
4. Determination of the Mode II fit parameter ($C_{100\%}$) considering $m = m_{0\%}$;
5. Interpolation of the C for the desired MR;

$$C(MR) = C_{100\%}^{MR}.C_{0\%}^{1-MR} \tag{5.33}$$

6. Prediction the da/dN.

$$\frac{da}{dN} = C(MR).(\Delta\sqrt{G_{1\_eq}})^{m_{0\%}} \tag{5.34}$$

5.6 Model Validation

The use of the model on different data sets can help to understand the limitations of it. Two different data sets were used to verify the model, the experimental results from the unsupported adhesive (Chap. 3) and the experimental results from Wan *et al* [21].

Figures 5.14 present the behavior of the coefficient C with a fixed exponent m and the model predictions for the unsupported adhesive. The prediction for MR=50% (see Fig. 5.15) showed a good agreement with the experiments. This result is not surprising as there was also a good agreement for this MR on the supported adhesive and the failure mechanisms for both adhesive versions are similar [22].

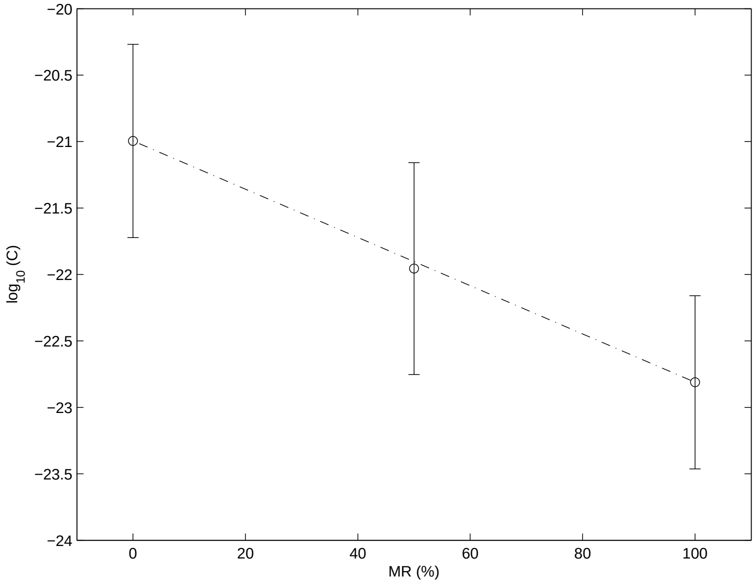

Figure 5.14: *Variation of C with a constant m for the unsupported data set.*

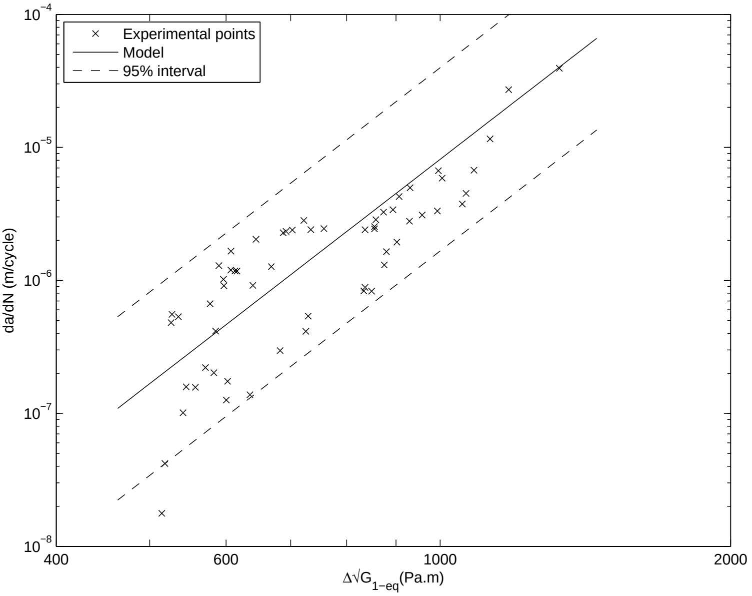

Figure 5.15: *Model predictions for the unsupported adhesive at MR=50%.*

Wan *et al* [21] studied the MM fatigue behavior of composite bonded joints. The adherents were laminates of 13 plies of carbon fiber-epoxy pre-preg (fiber G40-800-24k and matrix Cycon 5276-1, supplied by Cytec) with 0^o fiber orientation. The adherents were bonded with the film adhesive AF 163-2k with a knit carrier, supplied by 3M. They present the fatigue behavior for MR=0%, 20%, 40%, 60% and 80%. The authors will perform the tests at pure Mode II, however, this data is not available yet. As the pure Mode II data was not available, the model supposed a linear interpolation between $C_{0\%}$ and $C_{80\%}$. The relation between C and MR can be seen in Fig. 5.16.

On Fig. 5.16, one can see that the coefficients $C_{0\%}$, $C_{40\%}$, $C_{60\%}$ and $C_{80\%}$ follow almost a straight line. The exception would be the $C_{20\%}$. A deeper analysis on the reasons for this behavior is not possible, as the authors present only one fracture surface example for each MR. However, considering the examples presented, one possible explanation for this behavior is that from MR=40% and up the fracture does not happen only at the adhesive. A part of the fracture occurs within the adherent (delamination).

Consequently, at MR=40% an up, there is a mix of delamination and disbond. Additionally, the delamination fraction increases with a higher MR as there is more fibers exposed in the examples presented. This change in the failure mechanism would result in a shift of the FDG curves to the left, as, usually, the disbond fatigue resistance is higher than the delamination fatigue resistance. This behavior helps to explain the overlap of MR=0% and MR=60% and the overlap of MR=20% and MR=80% experimental points in the plot FDG vs G_{max} (Fig. 5.17).

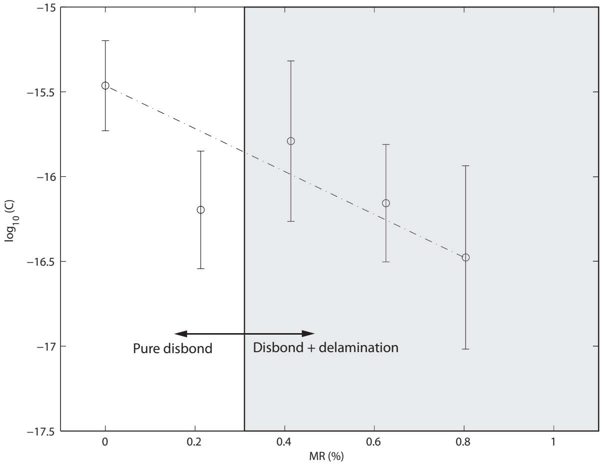

Figure 5.16: *Variation of C with a constant m for Wan et al [21] data set.*

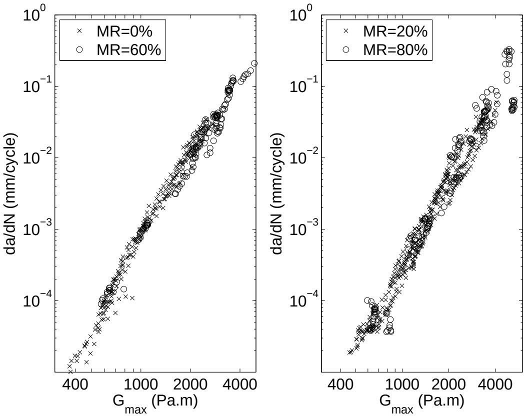

Figure 5.17: *Wan et al [21] data set. Due to a change in the failure mechanism, the fatigue behaviors of MR=0% and 60% and of MR=20% and 80% are similar.*

Despite the failure mechanisms discussed above, the model was applied to this data set and the predictions are presented in Fig. 5.18, 5.19 and 5.20. On these Figs. one can observe a good agreement between the model predictions and the experimental results for MR=40% and MR=60%. For MR=20%, the model overpredicts the experimental results, as was expected from Fig. 5.16. The overprediction is likely a result of the change in the failure mechanisms. However, the model assumption of a linear interpolation between the coefficients $C_{0\%}$ and $C_{100\%}$ (particularly for this case between $C_{0\%}$ and $C_{80\%}$) was able to capture accurately the change in the coefficient C for MR=40% and MR=60%.

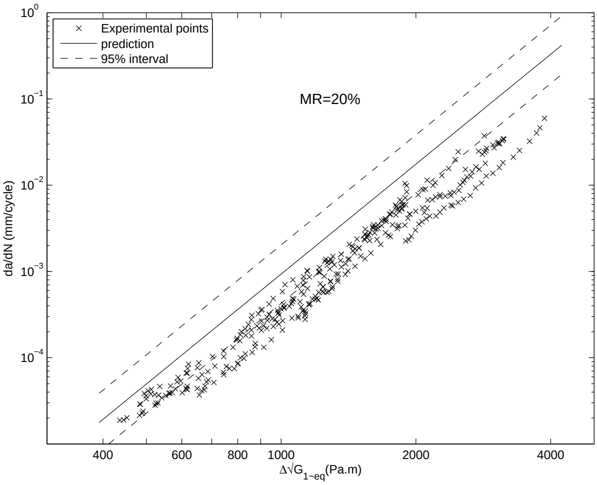

Figure 5.18: *Model predictions for Wan et al [21] data set at MR=20%.*

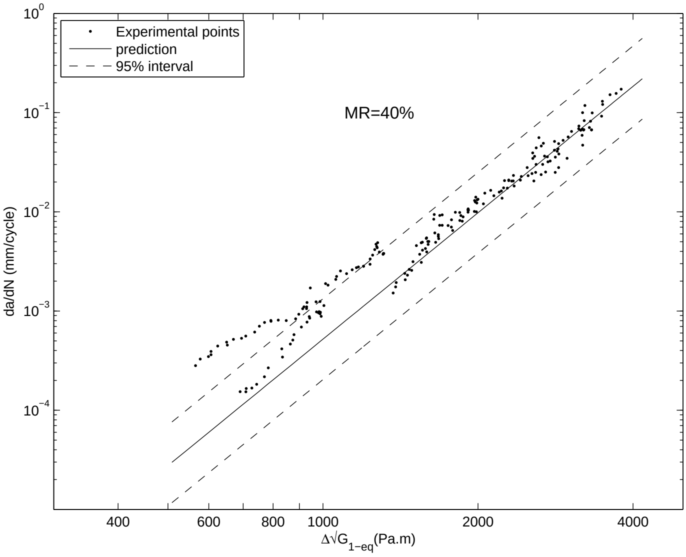

Figure 5.19: *Model predictions for Wan et al [21] data set at MR=40%.*

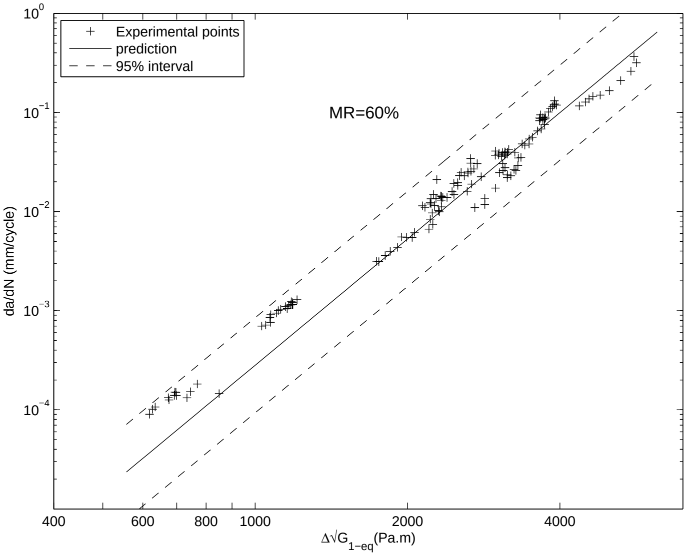

Figure 5.20: *Model predictions for Wan et al [21] data set at MR=60%.*

5.7 Model Discussion

The development of the model presented some assumptions. This section will discuss the implications of these assumptions and later discuss the methodology of the model applied with different functions of the SERR.

5.7.1 Model assumptions

The main model assumptions are listed below:

- The principal stress is the suitable parameter to describe disbond growth.
- The coefficient m is independent of the MR.
- There is a linear relation between $logC$ and MR.

As shown in Chap. 4, there is abundant evidence that the principal stress is the driving force of the disbond mechanism. Thus, the first assumption should not present further consequences.

The second assumption is strong and to some extension impossible to prove. The Paris relation is an experimental observation [23] and, as such, theoretical values for its coefficients are not available. Analysis of literature data does not reveal many data set where this assumption could be tested.

The literature presents some data sets for MM fatigue delamination [6, 13], where there is a large difference in the exponent m. However, fiber bridging may have an influence on the value of m [24]. Additionally, there are reports of no significant difference between the exponent m of pure Mode I and pure Mode II [20]. Experimental results on adhesive disbond on metallic bonded joints are scarce but the results from [25] show a trend with a small variation in the exponent m. However, one must remember that this experimental study [25] was conducted on a new specimen setup proposed by the authors and the results presented large scatter. On the other hand, the experimental data obtained in Chap. 3 and the results from Wan *et al* [21] suggest that this assumption may be true for MM fatigue disbond.

The third assumption suffer from the same problems of the second one, as it can not be theoretically confirmed and there are few data sets available to verify it. However, the failure mechanisms can supply some insights about the relation between $logC$ and MR.

The failure mechanisms indicate a continuous increase in the energy for crack growth as the MR increases. As a result, one should expect a monotonic behavior for this curve. Additionally, there should be a considerable difference between $logC$ for pure Mode I (MR=0%) and high Mode I. For both of these cases the failure mechanism is similar but the pure Mode I fracture occurs in the center of the adhesive and, because of it, it can easily find a less energy path. On the other hand, a fracture at high Mode I occurs close to the compressive adherent and, consequently, it has less room to find a less energy path. Lastly, the fracture at high Mode II seems similar to a pure Mode II fracture. Thus, one would expect similar coefficients as presented in Fig. 5.11.

Figure 5.21 presents the relation between the normalized $logC$ and the MR for the three data sets evaluated on this chapter. As the data set from Wan *et al* [21] does not present pure Mode II data, the $C_{100\%}$ was considered equal to $C_{80\%}$ (similarly to the data set from Chap. 3) in the Fig. 5.21. This figure also presents the model adopted and one possible function that describes more realistically this relation. This function was based on the effect of the failure mechanism (high Mode I and high Mode II parts, and the monotonic behavior) and the function also attempted to fit the experimental data.

Obtaining the real function that describes this relation is beyond the scope of this work, as it would demand the evaluation of several MRs and the final model could depend on some of these several MRs and not only on the pure Mode I and pure Mode II data. However, some conclusions can be drawn from Fig. 5.21. From this figure, one can conclude that the linear interpolation can result in good predictions for MR in

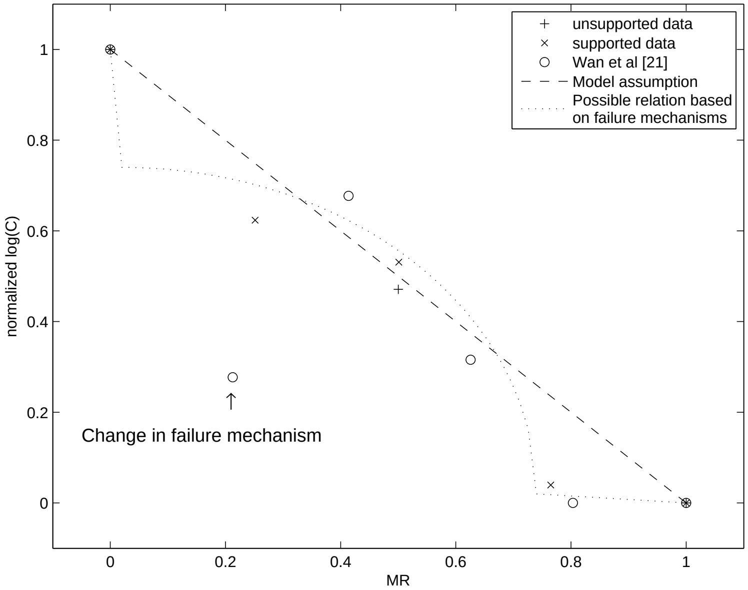

Figure 5.21: *Relation between logC and MR.*

the range of 30% to 60%. Additionally, for MR with a higher error (high Mode I and high Mode II regions) the model should predict a faster crack growth, being, then, a conservative model.

5.7.2 Model methodology

The model consists of three principal assumptions: the G_{1_eq} is the suitable parameter to describe disbond growth, the coefficient m is independent of the MR, and there is a linear relation between the *logC* and the MR. This section will explore the possibility of the last two assumptions coupled with the use of a common parameter used to describe the FCG.

The most common parameters used to describe the disbond and delamination are the G_{max}, $\Delta G = G_{max} - G_{min}$ and $\Delta\sqrt{G} = (\sqrt{G_{I-max}} - \sqrt{G_{I-min}})^2 + (\sqrt{G_{II-max}} - \sqrt{G_{II-min}})^2$ [23]. As all the experimental data evaluated on this work has the same load ratio (R=0.1), the first two parameters can be considered equivalent ($\Delta G = R^2.G_{max}$). As a result, only the last two parameters will be evaluated.

Table 5.2 presents the coefficient m obtained for the different parameters evaluated. Similarly to the results obtained using $\sqrt{G_{1\_eq}}$ only one m deviated from a constant value. For ΔG, $m_{75\%}$ was significantly different from the others and, for $\Delta\sqrt{G}$, $m_{100\%}$ was different.

Table 5.2: *Fit coefficients for the different G definitions.*

MR	m	
	ΔG	$\Delta\sqrt{G}$
0%	4.52	3.78
25%	3.98	3.88
50%	4.67	3.92
75%	3.33	3.96
100%	4.65	5.81

Considering $m = m_{0\%}$ and recalculating C one would obtain the results presented in Fig. 5.22. This figure indicates that a linear interpolation can be a good approximation of this relation. Additionally, the plots indicate that the linear interpolation should give good predictions for MR=25% and MR=75%. However, it should underestimate the crack growth for MR=50% (Fig. 5.22 and 5.23), being, therefore non-conservative.

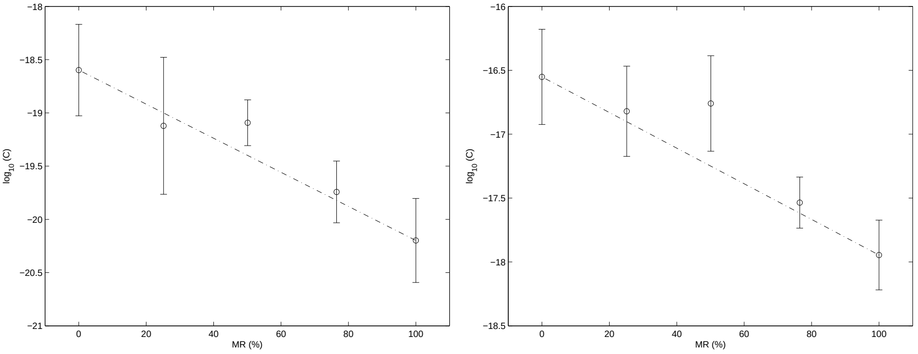

(a) MR vs log(C) for the parameter ΔG. (b) MR vs log(C) for the parameter $\Delta\sqrt{G}$.

Figure 5.22: *Mode I disbond surface example. Top right black arrow indicates the global crack growth direction.*

The predictions based on these parameters are presented in Fig. 5.23. As observed previously, the predictions for MR=25% and MR=75% are in good agreement with the experiments but for MR=50% the model underpredict the experimental results.

As stated in Sec. 5.7.1, obtaining the real function that describes the relation between MR and *logC* would demand the evaluation of several MRs and the function might depend on them, and not only on the pure Mode I and pure Mode II data. However, observing Fig. 5.22, the linear interpolation seems to not give a good estimative of the fatigue behavior for all MRs and it consistently underpredict the experimental results when applied to the other data sets evaluated in Section 5.6.

Therefore, the use of this methodology with a different parameter can yield good results under certain conditions. However, it can also underpredict the experimental results. Thus, this methodology should be avoided with other parameters, such as the ones evaluated in section.

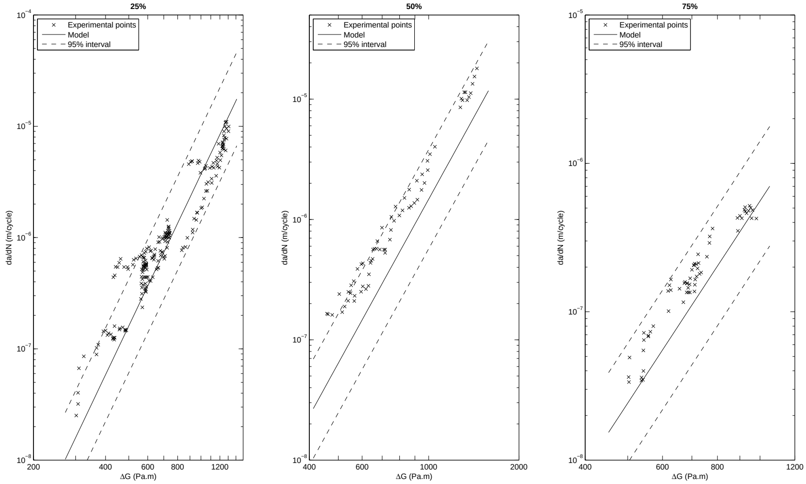

(a) ΔG

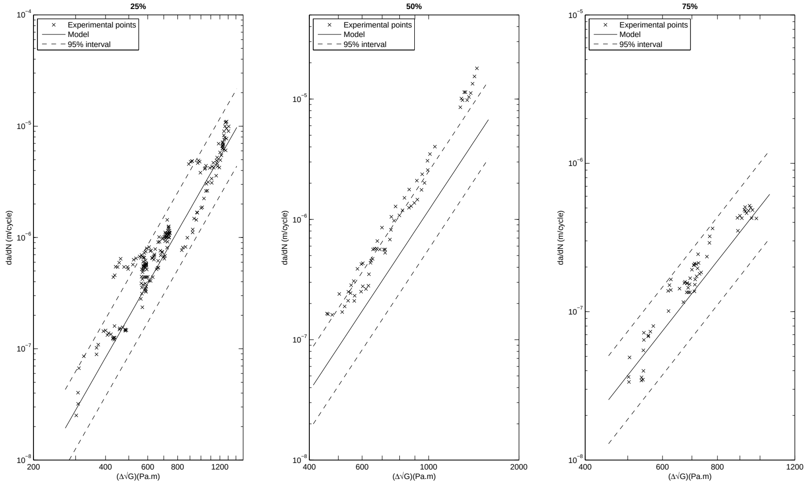

(b) $\Delta\sqrt{G}$

Figure 5.23: *FCG predictions for the different parameters.*

5.8 Conclusions

This chapter proposed and evaluated a new MM fatigue disbond model based on a parameter equivalent to the principal stress. The model inputs are only pure Mode I and Pure Mode II fatigue disbond growth data and the model evaluation was done in three different data sets. The model assumptions and simplifications were also discussed and their effects evaluated.

The simplifications proposed were shown to have a limited effect on the principal stress calculation and the model assumptions were in accordance with the experimental data available in the literature. The model was shown to give good predictions in the vicinity of MR=50% and to give conservative results for high Mode II but the difference in da/dN is smaller than one order of magnitude. An analysis of the failure mechanisms also indicated the conservativeness of the model for high Mode I and high Mode II.

Based on the discussed in this Chapter, the model developed has potential to accurately predict the fatigue disbond growth behavior on a Mixed-mode loading condition.

References

[1] R.L. Ramkumar and J.D. Whitcomb. Characterization of mode I and mixed-mode delamination growth in T300/5208 graphite/epoxy. pages 315–335. American Society for Testing and Materials, Philadelphia, 1985.

[2] C.G.Gustafson and M. Hojo. Delamination fatigue crack growth in unidirectional graphite/epoxy laminates. *Journal of Reinforced Plastics and Composites*, 6(1):36–52, 1987.

[3] A.J. Russel and K.N. Street. Predicting interlaminar fatigue crack rates in compressively loaded laminates. In *Delamination and Debonding of Materials ASTM STP 1012*, pages 162–178. American Society for Testing Materials, 1989.

[4] C. Dahlen and G.S.Springer. Delamination growth in composites under cyclic loads. *Journal of Composite Materials*, 28(8):732–781, 1994.

[5] G.A. Kardomateas, A.A. Pelegri, and B. Malik. Growth of internal delamination under cyclic compression in composite plates. *Journal of the Mechanics and Physics of Solids*, 43(6):847–868, 1995.

[6] M. Kenane and M.L. Benzeggagh. Mixed-mode delamination fracture toughness of unidirectional glass/epoxy composites under fatigue loading. *Composites Science and Technology*, 57(5):597–605, 1997.

[7] E. Sancaktar. Mixed-mode fatigue failure in structural adhesives. *ASTM Special Technical Publication*, (1332):764–785, 1999.

[8] J. Schön. A model of fatigue delamination in composites. *Composites Science and Technology*, 60(4):553–558, 2000.

[9] F. Ducept, P. Davies, and D. Gamby. Mixed mode failure criteria for a glass/epoxy composite and an adhesively bonded composite/composite joint. *International Journal of Adhesion & Adhesives*, 20(3):233–244, 2000.

[10] J. Andersons, M. Hojo, and S.Oschiai. Model of delamination propagation in brittle-matrix composites under cyclic loading. *Journal of Reinforced Plastics and Composites*, 20(5):431–450, 2001.

[11] P. T. Cheuk, L. Tong, C. H. Wang, A. Baker, and P. Chalkley. Fatigue crack growth in adhesively bonded composite-metal double-lap joints. *Composite Structures*, 57(1-4):109–115, 2002.

[12] M. M. Abdel Wahab, I. A. Ashcroft, A. D. Crocombe, and P. A. Smith. Numerical prediction of fatigue crack propagation lifetime in adhesively bonded structures. *International Journal of Fatigue*, 24(6):705–709, 2002.

[13] N. Blanco, E.K. Gamstedt, L.E. Asp, and J. Costa. Mixed-mode delamination growth in carbon-fibre composite laminates under cyclic loading. *International Journal of Solids and Structures*, 41(15):4219–4235, 2004.

[14] M. Quaresimin and M. Ricotta. Stress intensity factors and strain energy release rates in single lap bonded joints in composite materials. *Composites Science and Technology*, 66(5):647–656, 2006.

[15] H. Khoramishad, A. D. Crocombe, K. B. Katnam, and I. A. Ashcroft. Predicting fatigue damage in adhesively bonded joints using a cohesive zone model. *International Journal of Fatigue*, 32(7):1146–1158, 2010.

[16] P. A. Carraro, G. Meneghetti, M. Quaresimin, and M. Ricotta. Crack propagation analysis in composite bonded joints under mixed-mode (I+II) static and fatigue loading: Experimental investigation and phenomenological modelling. *Journal of Adhesion Science and Technology*, 27(11):1179–1196, 2013.

[17] P. A. Carraro, G. Meneghetti, M. Quaresimin, and M. Ricotta. Crack propagation analysis in composite bonded joints under mixed-mode (I + II) static and fatigue loading: A damage-based model. *Journal of Adhesion Science and Technology*, 27(13):1393–1406, 2013.

[18] H. Tada, P.C. Paris, and G.R. Irwin. *The stress analysis of cracks handbook: by Hiroshi Tada, with the cooperation of Paul C. Paris and George R. Irwin.* Paris Productions & (Del Research Corp.), 1985.

[19] C. Niu and M.C.Y. Niu. *Airframe Stress Analysis and Sizing.* Hong Kong Conmilit Press, 1997.

[20] A. J. Brunner, S. Stelzer, G. Pinter, and G. P. Terrasi. Mode II fatigue delamination resistance of advanced fiber-reinforced polymer-matrix laminates: Towards the development of a standardized test procedure. *International Journal of Fatigue*, 50:57–62, 2013.

[21] Z. Wan, T. Teng, and C. Li. Fatigue and fracture of adhesively bonded composite joints under mixed mode I/II loading. Technical report, National Research Council Canada, 2013.

[22] D. Bürger, C. D. Rans, and R. Benedictus. Influence of fabric carrier on the fatigue disbond behavior of metal-to-metal bonded interfaces. *The Journal of Adhesion*, 90(5-6):482–495, 2014.

[23] J. A. Pascoe, R. C. Alderliesten, and R. Benedictus. Methods for the prediction of fatigue delamination growth in composites and adhesive bonds - A critical review. *Engineering Fracture Mechanics*, 112-113:72–96, 2013.

[24] Yao L., R. Alderliesten, M. Zhao, and R. Benedictus. Bridging effect on mode I fatigue delamination behaviour in composite laminates. *Composites Part A: Applied Science and Manufacturing*, 63:103–109, 2014.

[25] T.A. Hafiz, M.M. Abdel-Wahab, A.D. Crocombe, and P.A. Smith. Mixed-mode fatigue crack growth in FM73 bonded joints. *International Journal of Adhesion and Adhesives*, 40(0):188 – 196, 2013.

6 Disbond Growth Behavior on a bonded Single Lap Joint under fatigue loading

This Chapter is a reproductions of [1].

The fatigue disbond behavior on a bonded Single Lap Joint (SLJ) was evaluated. Fatigue disbond tests were conducted and the Strain Energy Release Rate (SERR) was obtained through Hart-Smith [2] and FE simulations. Afterwards, the SERR from both methods was used, coupled with a Mixed-Mode (MM) fatigue disbond model based on the Mode I SERR in the principal stress direction to predict the Fatigue Disbond Growth (FDG). Additionally, a new method for disbond length measurement was applied using a Rayleigh Backscattering (RB) distributed sensing system for measuring strain on the SLJ. The approach employed estimates conservatively the FDG for SLJ and the RB system was found to be in good agreement with the results from visual inspection.

6.1 Introduction

Structural adhesives have long been considered a promising alternative to mechanical fasteners in the aerospace industry [3]. The load is transfered smoothly through the adhesive resulting in reduced stress concentrations and better fatigue performance of the joint. However, there is still a lack of confidence in the long term response of the adhesive, which prevents a wider use of adhesives in the aerospace industry. Different environmental [4–9] and cyclic loading conditions (loading spectra, mode ratio and stress ratio) [10–12] can substantially change the predicted life of a bonded joint.

One of the most important parameters to predict fatigue failure on adhesively bonded joints is the loading mode. On a bonded joint, the disbond usually occurs due to a combination of Mode I (opening) and Mode II (sliding shear) loading [13], as observed in a Single Lap Joint (SLJ). Due to the eccentric load, the disbond tip experiences both Mode I and II (see Fig. 6.1) and the Mode Ratio ($MR = G_{II}/G_{total}$) depends on several parameters: adherend length, thickness and mechanical properties; adhesive thickness and mechanical properties; and bonded length. As a result, the MR changes as the disbond extends.

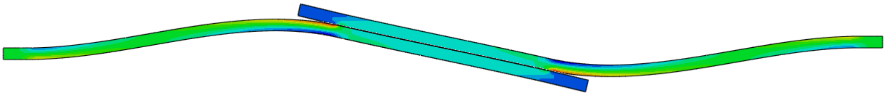

Figure 6.1: *SLJ example. The eccentric load generates Mode I loading at crack tip. The deformations are scaled to aid in visualization.*

In the past, some attempts have been made to predict disbond on a SLJ using only the Mode I component of the Strain Energy Release Rate (SERR) [14–17] as Mode I loading has been shown to be more detrimental [18]. Later, the effect of Mode II was also incorporated in order to increase the accuracy of the models [19, 20]. However, obtaining the Mode I and Mode II contribution in a SLJ is not straightforward.

The literature presents few analytical models for obtaining the SERR in a SLJ. They are usually an extension of models that obtain the stresses in the adhesive layer and later they convert these stresses (Eq. 6.1 and 6.2) [21] or the bending moment factor (k, defined in Eq. 6.5) (Eq. 6.3 and 6.4) [22] into SERR. The second approach (Eq. 6.3 and 6.4) avoids the use of stresses (σ_a and τ_a), which would require the bulk adhesive properties (E_a and G_a) that are difficult to measure experimentally [23].

$$G_I = \sigma_a^2 \frac{t_a}{2E_a} \tag{6.1}$$

$$G_{II} = \tau_a^2 \frac{t_a}{2G_a} \tag{6.2}$$

$$G_I + G_{II} = \frac{(P/w)^2}{16.E.t}(84k^2 + 12k + 1) \tag{6.3}$$

$$\frac{G_{II}}{G_I} = \left[\frac{1}{2\sqrt{3}}\left(\frac{1}{2k} + 3\right)\right]^2 \tag{6.4}$$

Papini *et al.* [24] and Fernlund *et al.* [25] developed one of the few analytical models that focus on the SERR. However, they supposed the SLJ extremes were free to rotate (pinned). Even though this method was shown to be useful, this boundary condition was shown to lead to erroneous results if the SLJ extremes were encastred.

Silva *et al.* [23] evaluated several models to predict static failure on SLJ, and, the model proposed by Hart-Smith (HS) [2] presented one of the best performances. Hart-Smith expanded the analysis of Goland and Reissner [26] by adding the effect of the adhesive thickness on the bending moment factor. The simplified bending moment factor obtained is presented in Eq. 6.5.

$$\frac{M}{P.t} = k = \frac{1}{2}.\frac{1 + \frac{t_a}{t}}{1 + \xi c + \frac{(\xi c)^2}{6}} \tag{6.5}$$

Where:

$$\xi^2 = \frac{P}{w} : \frac{E.t^3}{12(1-\nu^2)} \tag{6.6}$$

Alternatively, Quaresimin and Ricotta [20] used Finite Element (FE) simulations and the Virtual Crack Closure Technique (VCCT) to obtain the SERR. Later, they used the SERR coupled with Fatigue Disbond Growth (FDG) data from SLJ with different overlap lengths [27] to estimate the fatigue life of similar SLJs [28].

This paper attempts to predict the FDG on a SLJ using a model based on the Mode I SERR in the principal stress direction. The model inputs are Pure Mode I and Pure Mode II FDG data obtained with a Double Cantilever Beam test (DCB) and with an End Notched Flexure test (ENF). The SERR used on the MM FDG model will be obtained through FEA, which will be considered the real value, and it will also be estimated through the HS analytical model. Later both predictions will be compared with experimental results.

6.2 Experimental Description

6.2.1 Specimen Fabrication

Aluminum (2024-T3) adherends, with 6mm thickness were used. The aluminum sheets were cleaned with acetone, followed by a NaOH bath for 5 minutes, and then Chromic Acid Anodized (CAA) for 40 minutes at 40^{o}C. After the CAA, the primer BR 127, supplied by Cytec, was applied on the aluminum sheets to preserve the surface treatment. Prior to stacking, a thin film of Teflon (15mm width and 0.06mm thick) was positioned close to one of the overlap edges to create an initial disbond. The other edge was filled with extra adhesive to create an adhesive fillet in order to prevent or retard FDG on that end of the specimen. The bond plates were prepared with one adhesive layer.

The adhesive employed was FM-94, supplied by Cytec and it was supplied in a supported (with a fabric carrier) with a nominal thickness of 250μm. The cure cycle was followed according to the supplier instructions [29] and consisted of: heating up the specimen to 120^{o}C at 2^{o}C/min; held it at 120^{o}C for 60 minutes with a pressure of 0.4MPa; followed by a cooling of 30^{o}C at 4^{o}C/min. After cure, the bonded plate was machined in the final dimensions of the samples (Fig. 6.2).

6.2.2 Test Details

Prior to the fatigue test, tabs were attached to the ends of the SLJ to reduce the eccentric load as shown in Fig. 6.2. During the fatigue test the maximum and minimum loads were kept constant and the load applied was 14kN. The load ratio was set to R=0.1 at a frequency of 5Hz. Disbond growth was monitored visually by observing the location of the disbond tip at the side of the specimen. The specimen side received a thin thin layer of white paint prior to testing in order to improve the contrast between the specimen and the disbond, used to locate the disbond tip. Every 1,000 cycles the test was stopped, a picture was taken and the test was resumed until final failure. Later, the pictures were analyzed and the disbond tip determined. Once the disbond lengths were determined, the disbond growth rate was calculated using the Incremental Polynomial

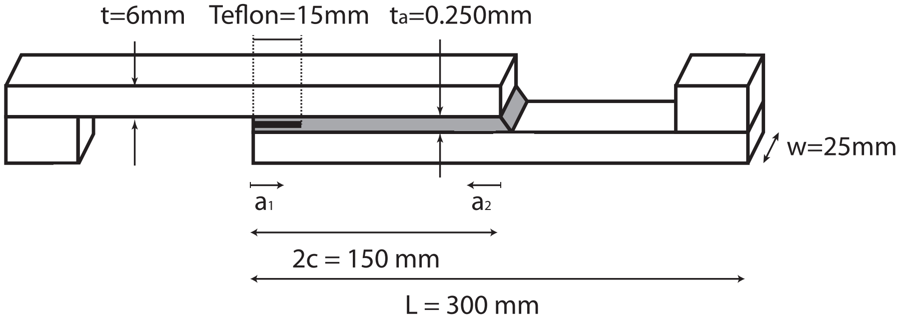

Figure 6.2: *Specimen details.*

Method [30] with seven successive data points and a second order polynomial equation. Three specimens were tested to assure the repeatability of the results.

Additionally to the visual inspection, the strains on the side of one specimen were monitored in an attempt to detect the disbond tip. In order to measure the location of the disbond in our experiment; a low bend loss Optical Fiber Sensor (OFS) was utilized. The OFS required no gratings, and it was adhesively bonded to the side of the coupon in order to monitor the changes in strain of the SLJ specimen. The strain measurement was performed utilizing a distributed sensing technique based on Rayleigh Backscattering [31].

In Rayleigh Backscattering, the backscattering phenomenon is based on a specific form of light wave reflection, were the light wave traveling through the fiber is reflected back from its source in a diffuse manner. In contrast, a specular reflection, which is commonly observed in a mirror, causes the light wave to be reflected from a single incoming direction into a single outgoing direction. This distributed strain measurement technique allows for spatial resolutions of strain at every 1.3mm at a maximum data acquisition frequency of 23.8Hz over a 10-meter fiber length.

A comparison study between this technique and strain gauges was performed by Martinez *et al.* [32] which showed that strain measurement with an accuracy of approximately 6 to 32 microstrain was obtainable when measuring strain fields between 109 and 764 microstrain respectively. The data acquisition system used in our strain measurement, is based on a commercially off the shelf Optical Frequency Domain Reflectometry (ODISI-B) produced by Luna Technologies Inc. [33]. A sketch of the OFS arrangement on the SLJ and the expected strain are presented in Fig. 6.3.

6.2.3 FE Simulations

A FE model was simulated in order to obtain the SERR of a SLJ for different crack lengths and the strains close to the bond line. A 2D model was used on Abaqus/Standard ®. The SERR was calculated using the Virtual Crack Closure Technique, a capability available in Abaqus. As boundary conditions, the region close to the ends (20mm) was prevented to rotate, simulating the grips, and on one end the displacements were restrained while the force was applied on the opposite end. The SLJ was modeled using elastic and geometrical linear behavior and the element type CPS4R. The mesh size was as follows: rectangular elements of 1mm x 3 mm on the non-overlap region and 1mm square elements on the overlap region. A convergence analysis

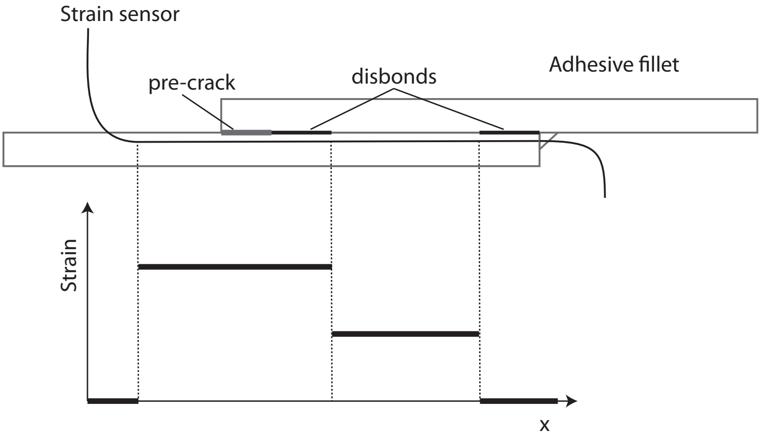

Figure 6.3: *Optical fiber arrangement and expected strain measurements.*

was performed and reducing the element size further has shown an effect smaller than 2% on the SERR. The Double Cantilever Beam and the Mixed-Mode Bending test geometries were also simulated in a similar procedure and the good agreement between the FEM results and the analytical equations for Mode I and II SERR [34, 35] indicates that this procedure can yield good predictions for SERR.

Once the model was ready, several combinations of crack lengths were simulated. Different disbond lengths were used, varying the disbond length in 10mm increments while the SERRs were recorded. Later, the results were interpolated to provide the SERR as a function of disbonds length. The results were interpolated using a second order polynomial as shown in Eq. 6.7. Where i refers to the opening mode (I or II) and j refers to the disbond side (1 for the pre-crack edge or 2 for the adhesive fillet edge).

$$G_{i}\_a_j = c_0 + c_1.a_1 + c_2.a_2 + c_3.a_1^2 + c_4.a_2^2 \tag{6.7}$$

6.3 Test results

The analysis of the post failure specimens revealed no evidence of interfacial failure, so none of the specimens were discarded. The results for the three specimens are presented in Fig. 6.4. The experimental procedure adopted presented repetitive results, as the final failure for the three samples was similar. In this figure, the effect of the adhesive fillet is clear, as the first signs of disbond growth were observed only at 30,000 cycles for specimens a and c while, on the pre-crack edge, the disbond is detected shortly after the test beginning.

In Fig. 6.5, one can observe some oscillation in the disbond growth rate, specially in the disbond growing from the pre-crack edge. This oscillation may be related with the development of the disbond. During the first stages, the disbond may suffer an influence of the teflon used as disbond starter or from the adhesive fillet.

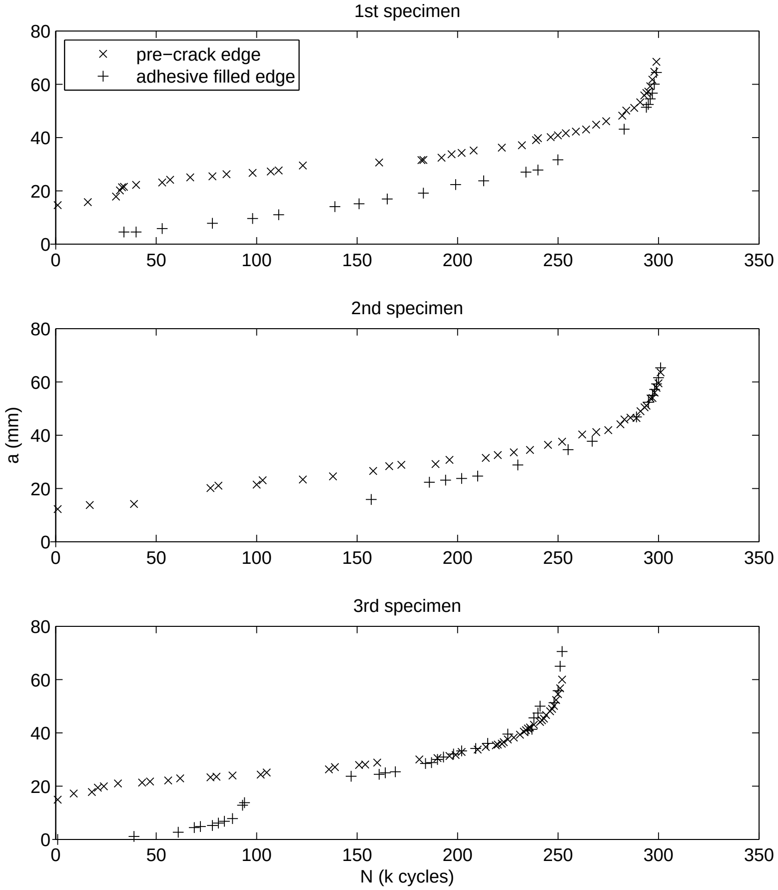

Figure 6.4: *Fatigue disbond growth results. Disbond length vs cycle number.*

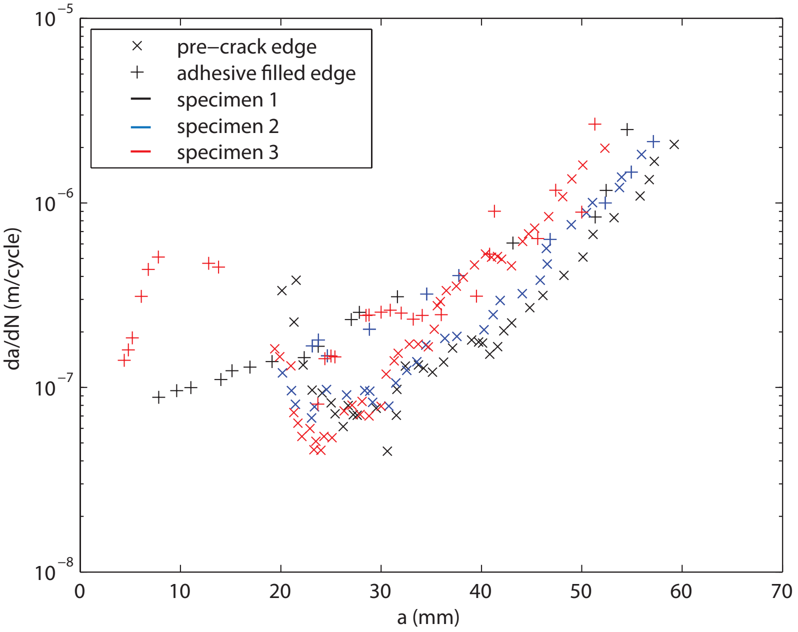

Figure 6.5: *Fatigue disbond growth rate results.*

6.3.1 Strain measurements

An example of the strains along the overlap region obtained using the OFS is present in Fig. 6.6. On the same figure, the strains obtained with a FEM are presented. One can see good agreement of the experimental results and the FEM, specially in the bonded region.

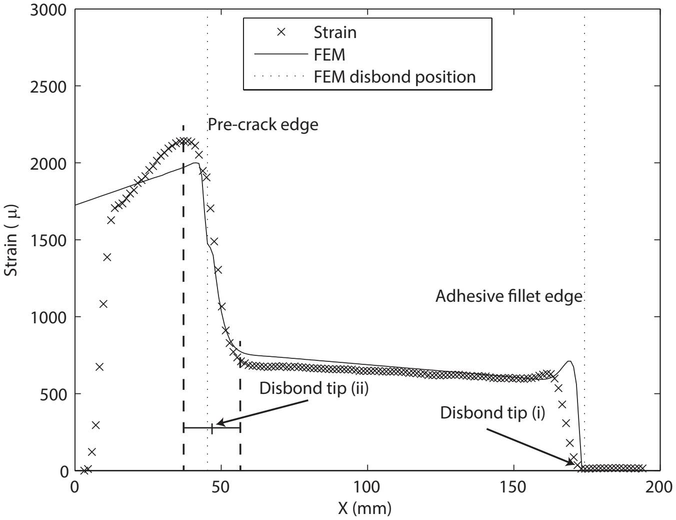

Figure 6.6: *Strain measurements close to the bond line (N=1000 cycles) and the definition of disbond tips.*

The worst agreement occurs close to the ends of the bonded region. However, close to the adhesive fillet edge, both curves show an increase in the strain before the strains diminish to zero. In addition, close to the pre-crack edge, the FEM was able to capture a similar strain distribution. A deeper analysis on the FEM results revealed that the strain levels on both edges vary significantly with distance to the bond line: the further the distance, the smaller the strain peaks are. In the example present in Fig. 6.6 the distance in the FEM was 2mm (Fig. 6.7). Additionally, the distance to the bond line does not alter significantly the strains in the bonded region. The distance from the optical fiber to the bondline was not recorded but was estimated to be between 1-2mm.

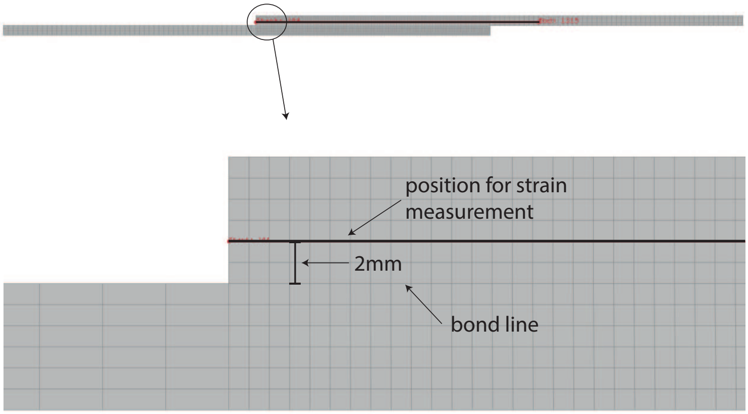

Figure 6.7: *Position for strain measurement on the FEM.*

6.3.2 Crack tip detection using a distributed strain measurement technique

Based on the good correlation between the strain measurements and the FEM, the strain was used to locate the disbond tip. At the disbond tip (i) (Fig. 6.6) the strain gradient is large, thus, the disbond position was considered the first point with zero strain. On the opposite side, the disbond tip (ii), the strain gradient is smaller. As a result, the disbond tip was considered the mid point between the maximum strain and the beginning of the strain plateau.

Based on these assumptions, the fatigue growth results are presented in Fig. 6.8 (a) and (b). One can observe the good agreement between the disbond tip detected by the strain measurements and the visual inspection, particularly for the disbond growing from the pre-crack edge. On the adhesive fillet edge, one can notice that at N=0 cycles the disbond is not 0mm. As the disbond at this edge must be 0mm at N=0 cycles, this point can be used to calibrate the curve. Thus, if the whole curve is shifted to match this point one would obtain the result presented in Fig. 6.8 (c).

Figure 6.8 indicates that the optical fiber distributed sensing system is a promising technique for disbond detection and a possible alternative to automate the disbond tip measurements for research applications. Additionally, this result also indicates OFS has potential to be used as a failure detector in a Structural Health Monitoring system.

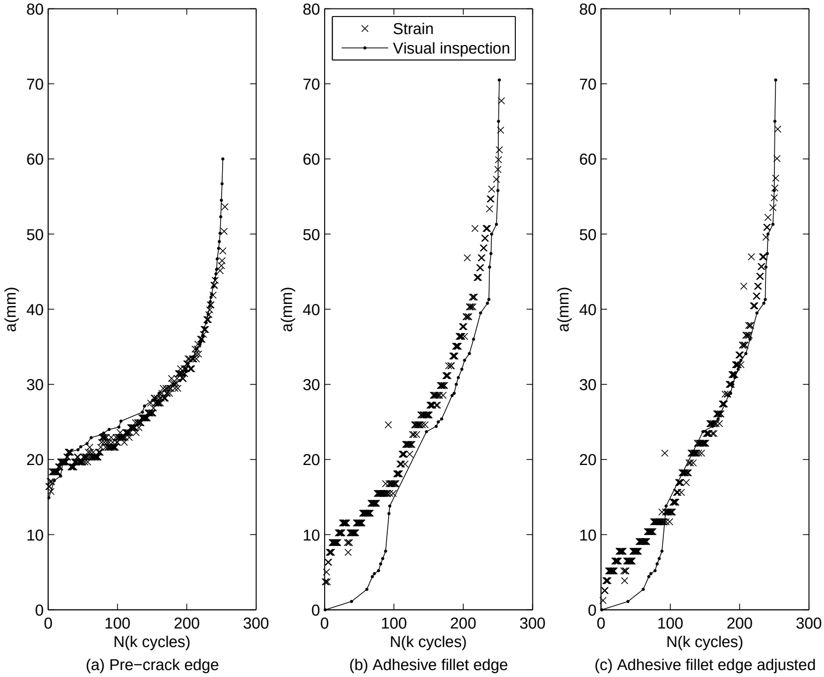

Figure 6.8: *Disbond tip detected using strain measurements from the OFS versus visual inspection.*

6.4 Disbond Growth Predictions

The use of a FDG model for SLJ requires the evaluation of the SERR as a function of the disbond lengths. Two methods were used to obtain the SERR: FEM and the analytical model developed by Hart-Smith (HS) [2]. HS model uses as inputs geometric and material values and it has as output the bending moment factor. This bending moment factor is then converted to SERR using Eqs. 6.3 and 6.4. As HS model does not obtain the SERR directly, Fig. 6.9 compares the SERR for the HS model and the FE model.

Observing Fig. 6.9, one can see that despite the good agreement between FEM and HS for G_{max} and MR, the HS model underpredicts the G_{Max} and the MR. The HS model estimates the G_{max} consistently 100 to 200 J/m^2 lower than the FEM. The MR range for the FEM goes from 50% to 65%, while from the HS model it goes from 60% to 70%. Thus, the difference goes from 5% to 10% in absolute values. Therefore, as a first approximation, the HS model can be used to estimate the values of SERR but the results might be non-conservative.

Based on the SERR estimated in Fig. 6.9, one can estimate the FDG for the SLJ. The FE was developed for different disbond lengths, then, both disbond lengths were used to predict the FDG. The HS model was developed for symmetrical SLJ, i.e., the disbond lengths should be the same. To overcome this issue, the disbond length was

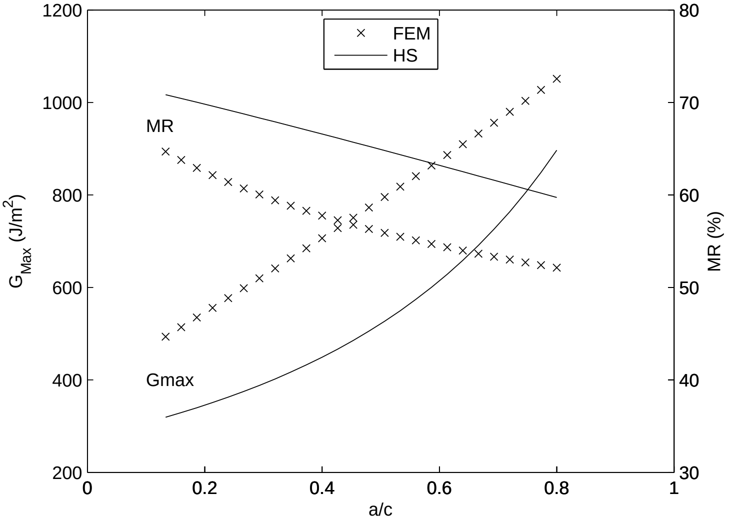

Figure 6.9: *Comparison of the total SERR and the MR obtained on a SLJ through FE and HS models. a/c indicates the disbond length divided by half of the initial overlap length.*

assumed to be the average of both disbond lengths.

Applying the above assumptions on the Mixed-Mode fatigue disbond model developed in Chap. 5 one can predict the FDG for the different specimens. The model coefficients were assumed to be the same as in Chap. 5, as the materials and bond procedure were identical.

The model assumes that the Paris relation exponent is independent of the MR if the similitude parameter chosen for the Paris relation is related to the principal stress (Eq. 6.8). Afterwards, the Paris coefficient C is obtained by a linear interpolation of the log of the coefficients $C_{0\%}$ and $C_{100\%}$ (see Fig.6.10).

$$G_{1\_eq} = \frac{\sqrt{G_I}}{2} + \sqrt{\frac{G_I}{4} + 4} \tag{6.8}$$

Figure 6.11 presents a typical prediction for the FDG of both disbonds on a SLJ. Only one specimen was chosen for brevity, as the other specimens had shown a similar trend. The predictions for the remaining specimens can be seen in Appendix C.

In Fig. 6.11 one can observe the better agreement between the experimental points and the predictions using the HS model for SERR. However, the HS model predicts non-conservative FDG rates. On the other hand, the predictions using the FEM for SERR are conservative and most experimental points fall below the lower 95% confidence boundary.

On the SLJ under analysis the MR ranges from 50% to 70%. Analyzing Fig. 6.10, this MR range seems to be overpredicted by the linear interpolation. As a result, one would expect conservative predictions. The predictions using FEM for SERR met those expectations and the effect of a variable MR as the disbond extends seems to not affect

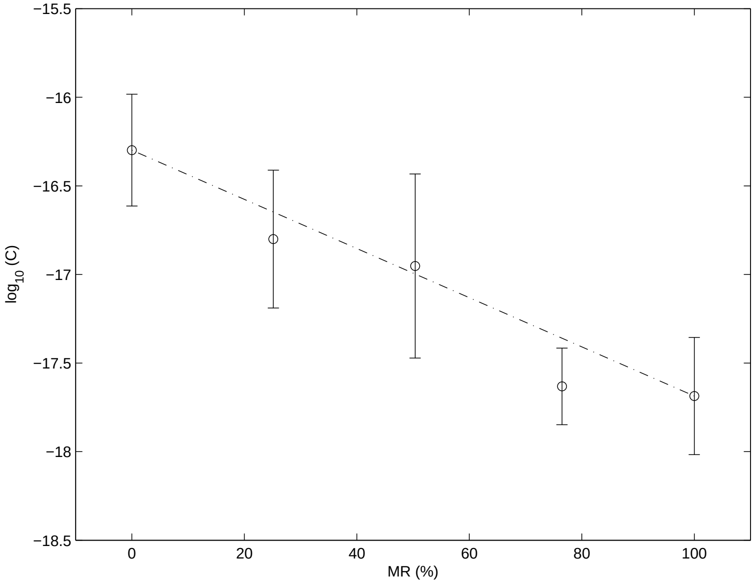

Figure 6.10: *Variation of the coefficient C as a function of the MR.*

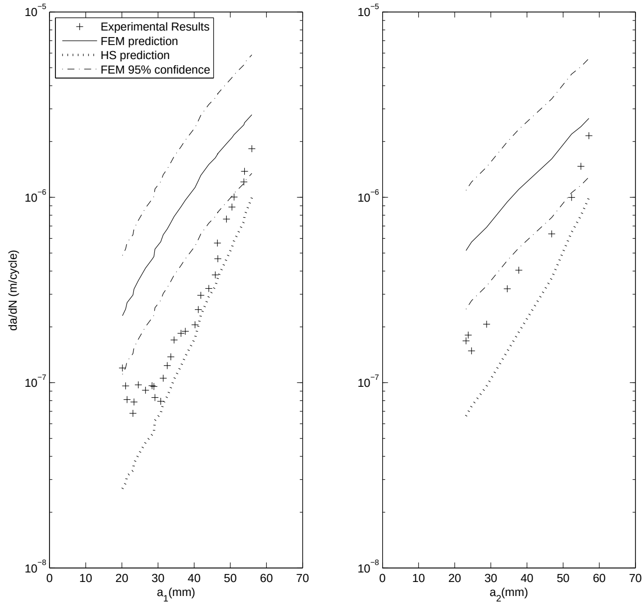

Figure 6.11: *FDG prediction for both disbond tips of a SLJ.*

these predictions. However, the predictions using the HS model were not expected.

It is likely that the smaller values predicted by the HS model for SERR (Fig. 6.9) resulted in slower FDG predictions. Therefore, the smaller values predicted by the HS model for SERR were counterbalanced by the conservative results expected from the FDG model on the MR under analysis. Therefore, the better predictions presented by the HS model are the effect of two errors canceling each other, resulting in an artificial good prediction.

For other SLJ configurations (different thickness, length or material) the MR may change and the FDG predictions using the HS model may deteriorate. However, the predictions using the FEM are expected to follow the model behavior, i.e., a good correlation in the MR range of 0% to 50% and conservative predictions in the range 50% to 100% (see Fig. 6.10).

6.5 Conclusions

This paper investigates the disbond growth behavior on a bonded SLJ. The main conclusions are listed below.

- The OFS can be used for disbond detection and it seems to be a promising technique to avoid the use of compliance methods or visual inspection.
- The HS model for SLJ can be extended to determine SERR but the values obtained (G_{max} and MR) underestimate the results obtained from FEM.
- Coupling the HS model with the MM FDG model from Chapter 5 can give a good estimative of the fatigue behavior for a SLJ but the results might be non-conservative.
- Coupling the MM FDG model from Chapter 5 with FEM resulted in predictions in accordance with the expected for the MM model, i.e., conservative results.
- The MM FDG model was able to capture the FDG behavior in a condition of variable MR.

Therefore, the FDG rate of a SLJ can be estimated using the MM model developed in Chap.5. Thus, the model has the potential to predict FDG in a condition of variable MR such as adhesive joints or bonded repairs.

References

[1] D. Bürger, C. D. Rans, and R. Martinez, M.and Benedictus. Fatigue disbond growth behavior on a bonded single lap joint. *to be submitted*, (xx).

[2] L.J. Hart-Smith, Douglas Aircraft Company, McDonnell Douglas Corporation, and Langley Research Center. *Adhesive-bonded Single-lap Joints*. NASA-CR-112236. National Aeronautics and Space Administration, 1973.

[3] Willard D. Bascom and Robert L. Cottington. Air entrapment in the use of structural adhesive films. *The Journal of Adhesion*, 4(3):193–209, 1972.

[4] N. Su, R. I. Mackie, and W. J. Harvey. The effects of ageing and environment on the fatigue life of adhesive joints. *International Journal of Adhesion and Adhesives*, 12(2):85–93, 1992.

[5] M. R. Bowditch. The durability of adhesive joints in the presence of water. *International Journal of Adhesion and Adhesives*, 16(2):73–79, 1996.

[6] W. K. Loh, A. D. Crocombe, M. M. A. Wahab, J. F. Watts, and I. A. Ashcroft. The effect of moisture on the failure locus and fracture energy of an epoxy-steel interface. *Journal of Adhesion Science and Technology*, 16(11):1407–1429, 2002.

[7] A. Baldan. Review adhesively-bonded joints in metallic alloys, polymers and composite materials: Mechanical and environmental durability performance. *Journal of Materials Science*, 39(15):4729–4797, 2004.

[8] L. F. M. da Silva and R. D. Adams. Joint strength predictions for adhesive joints to be used over a wide temperature range. *International Journal of Adhesion and Adhesives*, 27(5):362–379, 2007.

[9] K. T. Tan, C. C. White, D. L. Hunston, C. Clerici, K. L. Steffens, J. Goldman, and B. D. Vogt. Fundamentals of adhesion failure for a model adhesive (PMMA/Glass) joint in humid environments. *Journal of Adhesion*, 84(4):339–367, 2008.

[10] I.A. Ashcroft. A simple model to predict crack growth in bonded joints and laminates under variable-amplitude fatigue. *Journal of Strain Analysis of Engineering Design*, 39(6):707–716, 2004.

[11] E.A. Nolting, P.R. Underhill, and D.L. DuQuesnay. Variable amplitude fatigue of bonded aluminum joints. *International Journal of Fatigue*, 30(1):178–187, 2008.

[12] T.A. Hafiz, M.M. Abdel-Wahab, A.D. Crocombe, and P.A. Smith. Mixed-mode fatigue crack growth in FM73 bonded joints. *International Journal of Adhesion and Adhesives*, 40(0):188 – 196, 2013.

[13] F. Ducept, P. Davies, and D. Gamby. Mixed mode failure criteria for a glass/epoxy composite and an adhesively bonded composite/composite joint. *International Journal of Adhesion & Adhesives*, 20(3):233–244, 2000.

[14] A.J. Kinloch and S.O. Osiyemi. Predicting the fatigue life of adhesively-bonded joints. *Journal of Adhesion*, 43(1-2):79–90, 1993.

[15] A. J. Curley, H. Hadavinia, A. J. Kinloch, and A. C. Taylor. Predicting the service-life of adhesively-bonded joints. *International Journal of Fracture*, 103(1):41–69, 2000.

[16] H. Hadavinia, A. J. Kinloch, M. S. G. Little, and A. C. Taylor. The prediction of crack growth in bonded joints under cyclic-fatigue loading I. Experimental studies. *International Journal of Adhesion and Adhesives*, 23(6):449–461, 2003.

[17] H. Hadavinia, A. J. Kinloch, M. S. G. Little, and A. C. Taylor. The prediction of crack growth in bonded joints under cyclic-fatigue loading II. analytical and finite element studies. *International Journal of Adhesion and Adhesives*, 23(6):463–471, 2003.

[18] Y. . Jen and C. . Ko. Evaluation of fatigue life of adhesively bonded aluminum single-lap joints using interfacial parameters. *International Journal of Fatigue*, 32(2):330–340, 2010.

[19] G. Hu. Mixed mode fracture analysis of adhesive lap joints. *Composites Engineering*, 5(8):1043–1050, 1995.

[20] M. Quaresimin and M. Ricotta. Stress intensity factors and strain energy release rates in single lap bonded joints in composite materials. *Composites Science and Technology*, 66(5):647–656, 2006.

[21] K. Shahin and F. Taheri. The strain energy release rates in adhesively bonded balanced and unbalanced specimens and lap joints. *International Journal of Solids and Structures*, 45(25-26):6284–6300, 2008.

[22] M. S. Kafkalidis and M. D. Thouless. The effects of geometry and material properties on the fracture of single lap-shear joints. *International Journal of Solids and Structures*, 39(17):4367–4383, 2002.

[23] L. F. M. da Silva, P. J. C. das Neves, R. D. Adams, A. Wang, and J. K. Spelt. Analytical models of adhesively bonded joints-part II: Comparative study. *International Journal of Adhesion and Adhesives*, 29(3):331–341, 2009.

[24] M. Papini, G. Fernlund, and J. K. Spelt. The effect of geometry on the fracture of adhesive joints. *International Journal of Adhesion and Adhesives*, 14(1):5–13, 1994.

[25] G. Fernlund, M. Papini, D. McCammond, and J. K. Spelt. Fracture load predictions for adhesive joints. *Composites Science and Technology*, 51(4):587–600, 1994.

[26] M. Goland and E. Reissner. The stresses in cemented joints. *Journal of Applied Mechanics*, 11:A17–A27, 1994.

[27] M. Quaresimin and M. Ricotta. Fatigue behaviour and damage evolution of single lap bonded joints in composite material. *Composites Science and Technology*, 66(2):176–187, 2006.

[28] M. Quaresimin and M. Ricotta. Life prediction of bonded joints in composite materials. *International Journal of Fatigue*, 28(10 SPEC. ISS.):1166–1176, 2006.

[29] Cytec Engineered Materials. *FM 94 Adhesive Film - Technical Data Sheet*, 2010.

[30] Standard test method for measurement of fatigue crack growth rates, 2000.

[31] Mark Froggatt and Jason Moore. High-spatial-resolution distributed strain measurement in optical fiber with rayleigh scatter. *Appl. Opt.*, 37(10):1735–1740, 1998.

[32] M. Martinez, A. Beltempo, M. Yanishevsky, R. Rutledge, and B. Rocha. Load monitoring on shm platform 1a using luna technologies, distributed sensing fibre optic system. Technical Report LTR-SMPL-2012-0047, National Research Council Canada, 2012.

[33] http://www.lunainc.com/. Last Accessed June 18-2014.

[34] Standard test method for Mode I interlaminar fracture toughness of unidirectional fiber-reinforced polymer matrix composites, 2007.

[35] Standard test method for mixed Mode I-Mode II interlaminar fracture toughness of unidirectional fiber reinforced polymer matrix composites, 2006.

7 Conclusions and Closing Remarks

This thesis presented the work carried out to develop a damage tolerance model to predict Mixed-Mode (MM) fatigue disbond in a metallic bonded joint. In order to achieve this goal, an experimental study was carried out (Chapter 3), followed by the identification of the disbond failure mechanisms (Chapter 4). Meanwhile, the effect of an adhesive supporting system on the MM fatigue disbond behavior was also evaluated (Appendix A). Afterwards, the failure mechanism identified were used in the development of a damage tolerance model (Chapter 5). This model was, then, evaluated in fix Mode Ratio (MR) (Chapter 5) and variable MR (Chapter 6) conditions.

The main conclusions are listed in the following section.

7.1 Conclusions

In order to obtain a MM disbond model first the failure mechanisms were analyzed. The main conclusions related to the MM disbond mechanisms are listed below.

Failure Mechanisms - Chapter 4

- The disbond failure mechanisms are similar to the ones present in delamination, the main differences arise from the lack of fibers and fiber bridging.
- The local principal stress controls micro-crack nucleation and micro-crack growth.
- The Mode ratio controls micro-crack coalescence and, thus, the energy required for micro-crack coalescence.
- The Mode II component controls the crack path.

During the analysis of the failure mechanisms, a possible influence of the carrier on MM fatigue disbond behavior was detected. Thus, a study was conducted on the effect of the carrier on the failure mechanisms and on the fatigue behavior under MM conditions. The main conclusions obtained from this study are presented below.

Carrier effect - Appendix A

- The presence of a carrier adds new failure mechanisms.

- For the carrier under analysis, the new mechanisms were present only in the Mode II component and they were carrier fiber bridging and a different crack path.
- The new mechanisms resulted in a small reduction of the Mode II component.
- As a consequence, the Mode ratio also present a small reduction.
- And the fatigue behavior presented a small improvement.

Based on the mechanisms identified in Chap. 4, a new MM disbond model based on the principal stress was developed depending only on pure mode I and II fatigue disbond data. The model was tested on 2 data sets produced by the author and on 1 data set from the literature. To further verify the model, it was used to predict the fatigue disond growth behavior on a Single Lap Joint (SLJ), a situation of variable MR.

Model - Chapter 5 and 6

- The model was proved to present good predictions specially in the MR range from 25% to 50% if there are no sudden change in the failure mechanisms.
- Even with a change in the failure mechanisms (disbond + delamination), the model still presented good predictions for the case evaluated in Chapter 5.
- For high Mode II the model proved conservative. This conclusion was also supported by a comparison between failure mechanisms and the model assumption.
- The MR of the SLJ was around 60%, thus, the model predictions were conservative.

7.2 Closing Remarks

Model shortcomings

The model developed on this thesis is based on a series of assumptions. The assumptions and its consequences will be reiterated here.

A single disbond: Several models in the literature [1–4] assume a single disbond that grows by an increment (da) every cycle. However, Chapter 4 has showed evidence of the nucleation and grow of multiple cracks and a later coalescence of some of these micro-cracks forming the main disbond. A possible solution for this incoherence is the use of damage mechanics and a damage variable that quantifies the micro-cracks density/size. Damage mechanics is a powerful tool and it has the potential to account for Mixed-Mode, stress ratio, Variable Amplitude, among other effects. However, the development of a damage evolution law can be difficult, specially if this law attempts to account for all the parameters affecting the fatigue disbond. Thus, most of the research still assumes a singe disbond tip and ignores the damaged zone ahead of the disbond tip.

Paris relation exponent is independent of MR: As state previously, the Paris relation is an empirical observation and, as such, it does not allow a theoretical estimation of its coefficients. Additionally, there is not many data sets available in the literature to verify this assumption. The data sets evaluated [5, 6] and the experimental results obtained (Chapter 3) seems to be in accordance with this assumption. Additionally, it was observed a strong dependence between the Paris relation coefficients, with more than 20% of difference if distinct regression methods are used and a small difference in the resulting regression curve (see Table 3.1 and Fig. 3.14). Thus, part of the variation in the Paris relation exponent reported in the literature [5] can be attributed to the dependence between the coefficients and the regression method used.

Linear relation between the log of the Paris relation coefficient and the MR: Similarly to the previous assumption, this can not be theoretically proven as the Paris relation is an empirical observation. Additionally, the analysis in Chapter 5 has showed that a linear function does not describe accurately this relation. However, the linear function can be used to approximate the relation with a good agreement near 50% and it estimates conservatively for high Mode II.

Model Applicability

Despite the shortcomings listed above, the model developed in this thesis represents an improvement in mechanistic modeling of mixed-mode disbond growth. Although specific empirical aspects remain (non-physical based power law fit of experimental data sets) and engineering approximations are applied (assumption of a single disbond front despite evidence of a damage zone), the model greatly reduces the amount of empirical data necessary and attempts to link behavior to observed fracture mechanisms. In presenting this model, effort has been made to expose potential shortcomings and dangers in applying the model. It is not claimed that all aspects of predicting the complexities of mixed-mode disbond growth have been captured in this work. Instead, by studying the phenomenon of mixed mode disbond growth in this thesis, it is hoped that:

a) a greater understanding and appreciation of the complexities of the phenomenon are gained,

b) a more convenient and easier semi-empirical engineering model for disbond growth has been developed which can be applied using the above understanding.

Practical limitations to applying damage tolerance philosophy to bonded joints

In order to apply the damage tolerance approach for bonded joints in the AE industry, some problems still need to be solved. One of the main problems is related to inspection and damage detection. Currently, there is still no reliable inspection technique that can assure the integrity of a bond line. Failures such as adherends contact (kissing bond) and weak bond still pose as one of the main challenges to be overcome before damage tolerance can be used in adhesives. Additionally, polymers are known to be greatly affected by temperature, water and other chemicals. As a result, the effect of these parameters on the fatigue disbond behavior must also be addressed.

Additionally, the use of damage tolerance usually requires a load that is then converted to crack growth rate through a power function (Paris relation). The exponent of the power function normally ranges between 2 and 3 for metals [7]. This means that a 10% increment in the load would result in a 33% increment in the crack growth rate. However, for the adhesive evaluated in this thesis, the exponent is 7.5, when related directly to the stress intensity factor, and it can be larger than 10 for other adhesives [5]. Thus, the same 10% load increment can result in a 160% ($n = 10$) increment in the crack growth rate. This large uncertainty is one of the reasons for the no growth requirement for composite delamination and, certainly, it will affect similarly adhesive bonding certification. Even adhesives regarded as "good in fatigue resistance", as the FM ®300 [8], can present exponents close to 8 [9]. Thus, the use of the damage tolerance philosophy on adhesive bonding also requires the development of adhesives with better fatigue performance.

References

[1] R.L. Ramkumar and J.D. Whitcomb. Characterization of mode I and mixed-mode delamination growth in T300/5208 graphite/epoxy. pages 315–335. American Society for Testing and Materials, Philadelphia, 1985.

[2] M. Kenane and M.L. Benzeggagh. Mixed-mode delamination fracture toughness of unidirectional glass/epoxy composites under fatigue loading. *Composites Science and Technology*, 57(5):597–605, 1997.

[3] N. Blanco, E.K. Gamstedt, L.E. Asp, and J. Costa. Mixed-mode delamination growth in carbon-fibre composite laminates under cyclic loading. *International Journal of Solids and Structures*, 41(15):4219–4235, 2004.

[4] P. A. Carraro, G. Meneghetti, M. Quaresimin, and M. Ricotta. Crack propagation analysis in composite bonded joints under mixed-mode (I + II) static and fatigue loading: A damage-based model. *Journal of Adhesion Science and Technology*, 27(13):1393–1406, 2013.

[5] T.A. Hafiz, M.M. Abdel-Wahab, A.D. Crocombe, and P.A. Smith. Mixed-mode fatigue crack growth in FM73 bonded joints. *International Journal of Adhesion and Adhesives*, 40(0):188 – 196, 2013.

[6] Z. Wan, T. Teng, and C. Li. Fatigue and fracture of adhesively bonded composite joints under mixed mode I/II loading. Technical report, National Research Council Canada, 2013.

[7] R. Jones, S. Pitt, A. J. Bunner, and D. Hui. Application of the Hartman-Schijve equation to represent mode I and mode II fatigue delamination growth in composites. *Composite Structures*, 94(4):1343–1351, 2012.

[8] *FM 300 Epoxy film adhesive - Technical Data Sheet.*

[9] S. Mall and W. S. Johnson. Characterization of mode I and mixed-mode failure of adhesive bonds between composite adherends. Technical report, National Aeronautics and Space Administration, 1985.

A Influence of Fabric Carrier on the Fatigue Disbond Behavior of Metal-to-Metal Bonded Interfaces

The effect of an adhesive support on the Mixed-Mode fatigue properties of a metal-to-metal bonded interface was evaluated. Pure Mode I, pure Mode II and Mixed-Mode fatigue disbond tests were conducted on supported and unsupported bonded samples. The fracture surfaces were observed and related to the fatigue disbond growth rate. The supporting system analyzed was found to not affect the fracture surface under Mode I loading, resulting in similar disbond growth rates for both supported and unsupported bonds. However, under Mixed-Mode and Mode II loading the supporting system improved the fatigue resistance. The improvement was related to different failure mechanisms caused by the supporting system such as Mode II load bearing and a change in the disbond path.

This appendix is a reproduction of [1].

A.1 Introduction

Adhesive bonded joints offer numerous performance advantages over their mechanically fastened counterparts, including a more distributed load path that can reduce stress concentrations and improve fatigue performance. The performance of bonded joints, however, is sensitive to numerous processing parameters that can be difficult to control in practice. Adherend surface preparation, for example, is a critical parameter for joint performance and poses challenges for applications such as in-field bonded aircraft structural repairs [2]. Bond line thickness is another example of a critical parameter that can influence joint performance [3–11].

The sensitivity of adhesive bonded joint performance to various processing parameters generates uncertainty in the quality and performance of a given bonded interface.

Although strict process control coupled with non-destructive inspection techniques provide some basis for qualifying as-manufactured joints and assessing in-service degradation, sufficient uncertainty currently remains. As a result, safety-critical joining applications, such as primary aircraft structures, primarily use mechanically fastening due to its predictable, yet typically inferior, performance. Conversely, in instances where bonding is used, a mechanically fastened backup is typically present and sized to accommodate failure on the bonded interface. Indeed, increasing the usage of adhesive bonding for safety-critical structures requires improvements in reliability and robustness through increased process control, improved inspection techniques, and improved predictive capabilities for performance and degradation.

As mentioned above, bond line thickness is known to be a critical parameter that influences the strength and durability of adhesive joints. A common strategy to control bond line thickness with film adhesives is the use of a fabric carrier, or microspheres which act as a spacer between the adherends during curing. Although these strategies are effective at controlling bond line thickness, they also can influence the behavior of the bonded joint. Understanding these effects is critical to improving the reliability and robustness of bonded interfaces.

Relatively few studies have investigated the influence of a fabric carrier, or scrim cloth, on the behavior of adhesively bonded interfaces. A comparative study by Zheng and Ashcroft [12] found that the presence of a nylon carrier fabric in joints containing Hysol Dextes's (Dsseldorf, Germany) EA9628 epoxy film adhesive increased tensile joint stiffness by approximately 10%, although it was noted that manufacturing/batch differences may also contribute to this difference. Butkus et al. [13] studied the bulk properties of cured sheets of film adhesive with and without a carrier fabric. Overlapping confidence intervals on their results for material stiffness suggested only a weak influence on the carrier fabric on this property. Mode I fracture toughness of the adhesive, however, was decreased by 15-30% by the presence of the fabric carrier. Da Silva and Adams [14] observed concluded that the adhesive with a carrier is similar to a composite material with the carrier fibers influencing on tension properties but not on shear properties. With respect to the joint strength, studies by Sancaktar et al. [15], Dixon et al. [16] and Gouri et al. [17], found that the presence of a carrier fabric increased peel strength, shear strength, and Mode I critical strain energy release rate (SERR). Da Silva and Adams [14], and da Silva et al [18] observed that the carrier does not affect the adhesive failure load on a single lap joint. Studies by Sancaktar [19] and Jablonski [20] also demonstrated an influence on disbond growth behavior and disbond growth mechanisms under Mode I fatigue loading. No studies in the literature were found on the influence of a fabric carrier on Mode II and Mixed-Mode (MM) fatigue behavior.

This paper investigates the influence of a fabric carrier on the fatigue disbond behavior of a metal-to-metal bonded interface. The commercial epoxy film adhesive, FM-94 from Cytec (Woodland Park, USA), with a nylon fabric carrier (supported) and without (unsupported) is used for this study. A detailed study of Mode I, Mode II and MM fatigue disbond growth behavior is undertaken using a combination of disbond growth monitoring and post-fracture fractography.

A.2 Experimental Procedure

An experimental study to characterize the effect of a fabric carrier on the fatigue disbond growth of a metal-to-metal interface was carried out. Both disbond growth rate and post-fracture fractography were employed to investigate any influence of the fabric carrier on the fatigue disbond behavior. Fatigue tests were conducted in pure Mode I, pure Mode II and MM at 50% ($\frac{G_{II}}{G_I+G_{II}}$, where G_I and G_{II} stands for strain energy release rate due to Mode I and Mode II loading, respectively). Additional tests in the supported adhesive were conducted varying the mode ratio from 20% to 90% in 10% increments. After the fatigue tests, the fracture surfaces were observed in a Scanning Electron Microscope (SEM).

The adhesive employed was FM-94, supplied by Cytec, and it was supplied in the supported (with a fabric carrier) and unsupported versions. Both versions had a nominal thickness of 250 μm. Aluminum (2024-T3) adherends, with 6mm thickness, were used. The aluminum sheets were cleaned with acetone, followed by a NaOH bath for 5 minutes, and then Chromic Acid Anodized (CAA) for 40 minutes at 40^{o}C. After the CAA, the primer BR 127, supplied by Cytec, was applied on the adherends to preserve the surface treatment. Afterwards, the aluminum sheets were stored from 3 to 15 months. According to the primer and adhesive data sheet [21], primed adherends can be stored for long periods without degradation of the final bonding. Prior to stacking, a thin film of Teflon (50mm width and 0.06mm thickness) was positioned close to the edge of the metal sheets to create an initial disbond.

The bonded plates were prepared with one layer of adhesive, and no extra technique was used to control the bond line thickness. The cure cycle followed the supplier's instruction [21], and consists of: heating up to 120^{o}C at 2^{o}C/min; holding at 120^{o}C for 60 minutes with a pressure of 0.4MPa; cool down to 30^{o}C at 4^{o}C/min. After cure, the bonded plate was machined in the final dimensions of the samples in Fig. A.1. The specimens were stored at 20 - 25^{o}C, relative humidity of 50-70%, for one to six months before testing and prior testing the thickness was measured.

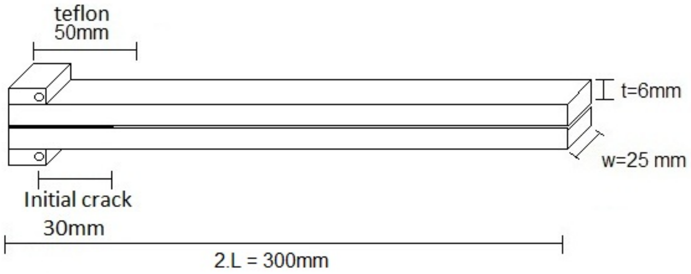

Figure A.1: *Specimen details.*

The tests performed were based on the Double Cantilever Beam (DCB) and on the Mixed-Mode Bending Test (MMB) [22, 23] standards (see Fig. A.2). The Mode II test was performed at a particular arrangement of the MMB setup. In the condition where C (lever length) is equal to L/3 (half-span length), the Mode I contribution is equal to zero, thus the test is in pure Mode II. For the Mode I data reduction, the three methods (Modified Beam theory, Compliance Calibration and Modified Compliance Calibration) presented in the standard [23] showed similar results and the Compliance Calibration Method was chosen to reduce the data. For the MM and Mode II data reduction, the equations proposed (Eq. A.11 and A.2) in the standard [22] were used, as they take into account delamination/disbond length corrections and the lever arm weight. The crack length correction parameter χ was calculated according to the standard [22], using the properties of the adherend (Aluminum).

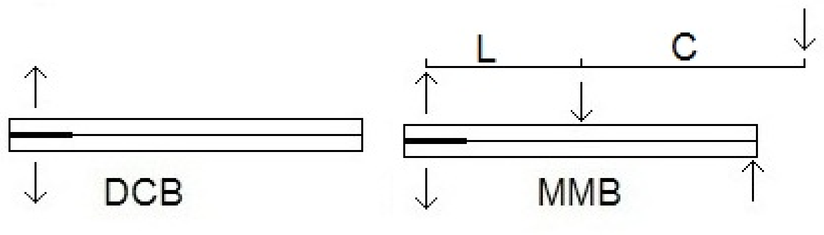

Figure A.2: *Test details.*

$$G_I = \frac{12[P(3C-L)+P_g(3C_g-L)]^2}{16w^2t^3L^2E}(a+\chi t)^2 \tag{A.1}$$

$$G_{II} = \frac{9[P(C+L)+P_g(C_g+L)]^2}{16w^2t^3L^2E}(a+0.42\chi t)^2 \tag{A.2}$$

Piano hinges were fastened to the adherends for the specimen loading (see Fig. A.1). During the fatigue test, the maximum and minimum displacement were kept constant, the load ratio was set as R=0.1 and the frequency was 5 Hz. The fatigue tests were conducted in the region II of the crack growth rate, usually described by the Paris relation or a variant of it. Prior to the fatigue loading, Mode I loading was applied to increase the crack length. This procedure guarantees a sharp crack tip and reduces the influence of the Teflon film. For the fatigue tests, the initial crack length was between 50mm and100mm.

A minimum of three samples was tested in each of the mode ratios evaluated. Disbond growth was monitored visually by observing the location of the disbond tip at the side of the specimen. After a certain number of cycles the test was stopped, a picture was taken and the test was continued. Subsequently, the pictures were analyzed and the crack tip determined. A compliance method to determine the crack length was not used because the crack length points acquired visually were sufficient to obtain the crack growth curve, and also to avoid the use of a transfer function. A thin layer of white paint was added to the side of the specimen prior to testing to improve the contrast between the specimen and disbond, aiding in visual detection (e.g. in Fig. A.3). The disbond growth rate was calculated using the Incremental Polynomial Method [24] with seven successive data points and a second order polynomial equation. After the fatigue test, the specimens were dismantled, coated with gold and observed in the Scanning Electron Microscope (SEM) with magnification from 50x to 10.000x.

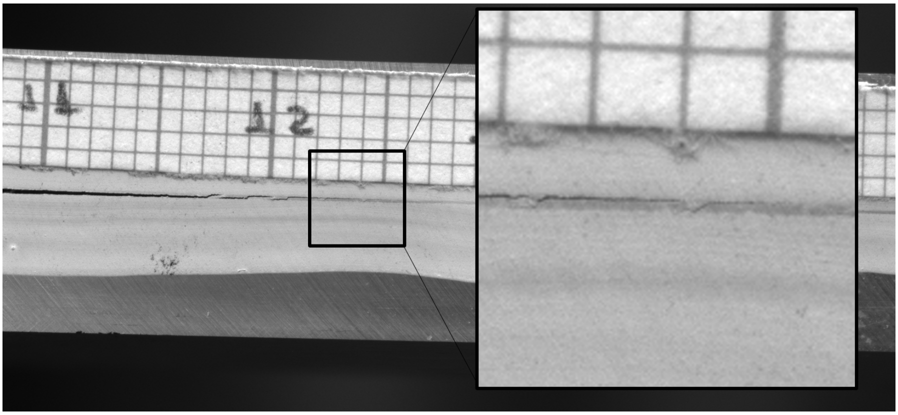

Figure A.3: *Example of white paint use to enhance the contrast between the specimen and disbond tip.*

A.3 Results and discussion

The total average thickness of the samples was 12.24±0.03 mm for the supported adhesive and 12.25±0.03 mm for the unsupported adhesive. As the adherends thickness is 2 x (6.01±0.01)mm and came from the same sheet, the thickness of the adhesive layer is approximately 220 μm and 230 μm, for the supported and the unsupported adhesives, respectively. So, the bond line thickness in both cases measures approximately the same as the nominal thickness of the adhesive film. Consequently, the manufactured specimens achieved sufficient similarity for comparison.

The critical strain energy release rate in Mode I measured was $G_{Ic} = 1780 \pm 200$N/m. G_{IIc} and G_c for MM conditions were not possible to obtain due to plasticity in the adherends.

A.3.1 Mode I fracture behavior

The Mode I fatigue results are presented in Fig. A.4. The data is displayed in a semi logarithmic scale and not in the generally used log-log scale for fatigue results. The semi logarithmic scale was chosen to highlight differences that would seem minimal in the log-log scale, particularly in MM and Mode II. Additionally, the graph presents the data as a function of $(\sqrt{G_{max}} - \sqrt{G_{min}})^2$. This parameter was chosen to remove the dependency of the mean load and maintain the dependency only of the load amplitude [25]. As can be seen in Fig. A.4, there is no significant difference between the disbond growth rate of the supported and the unsupported adhesive.

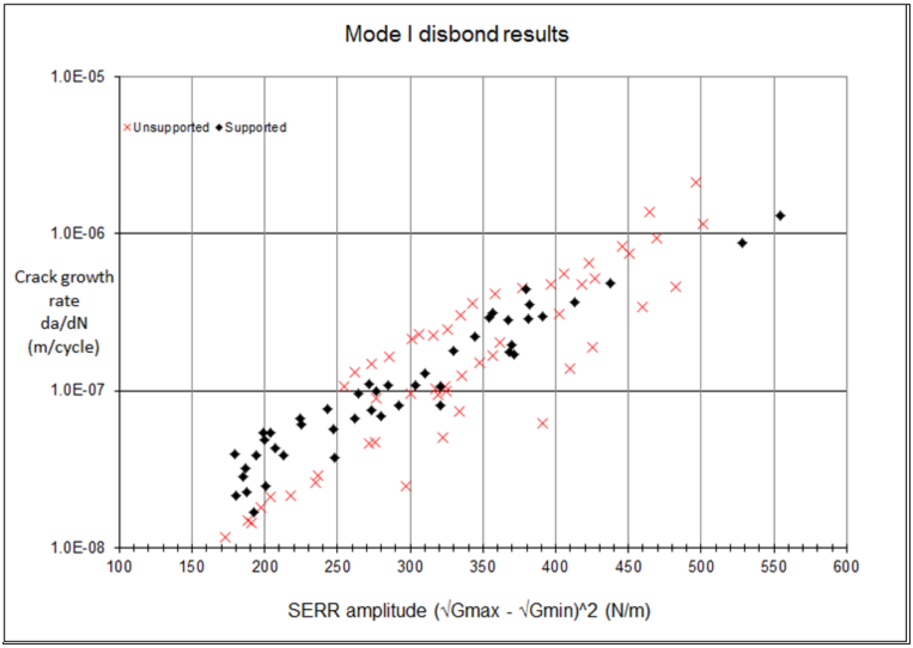

Figure A.4: *Fatigue disbond growth results for Mode I loading. The supported and the unsupported adhesives present similar results.*

Mode I disbond, similarly to Mode I delamination, is characterized by the coalescence of micro cracks ahead of the crack tip. The micro cracks can grow in different directions and they coalesce, forming the main crack. The different manners the micro cracks coalesce form different features as scarps or feather pattern [26].

Figure A.5 shows the fracture surface of the supported and unsupported samples where both features can be observed. The fracture surfaces show similar features and the main difference is in the carrier region, which results in an imprint on the surface. These observations indicate that the carrier does not significantly affect the fracture mechanisms on the bonded area. However, the carrier could reduce the effective bonded area, as the imprints indicate a discontinuity in the contact between the adhesive and the adherend. The smaller bonded area would result in a reduced fatigue resistance for the supported adhesive. However this effect may be too small to be observed in the present test.

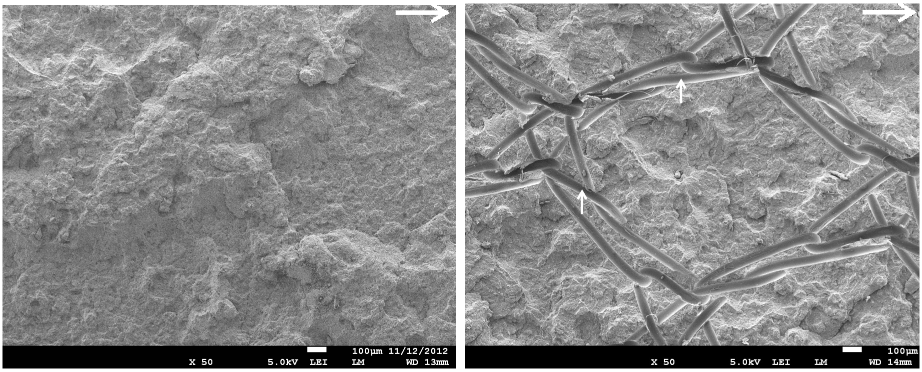

(a) Unsupported 50x

(b) Supported 50x White arrows indicate the carrier imprint.

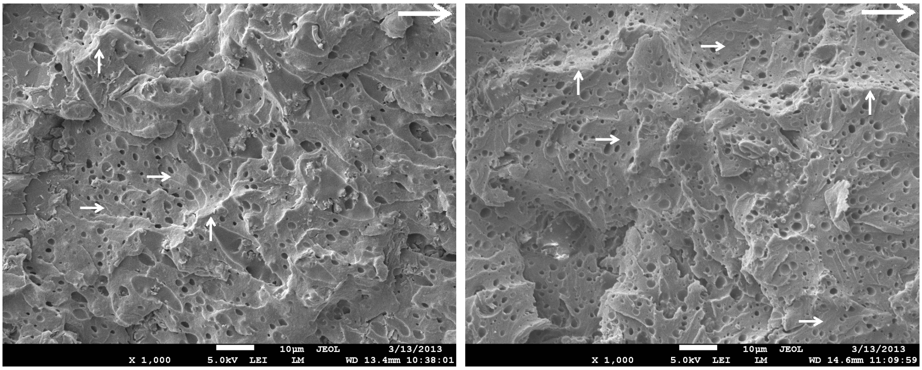

(c) Unsupported 1000x Vertical white arrows indicate scarps and horizontal white arrows indicate feather pattern.

(d) Supported 1000x Vertical white arrows indicate scarps and horizontal white arrows indicate feather pattern.

Figure A.5: *Comparison between the Mode I fracture surfaces. Top right black arrows indicate the main disbond growth direction.*

After the fatigue test, the carrier was almost detached from the adhesive, leaving few fragments on the surface. On the fragments observed, one can notice damage on the carrier fibers (see Fig. A.6) with transverse cracks and parts of the carrier fiber that were pulled apart. Similar cracks were reported by Jablonski [20] and they were related to the cyclic load the fibers bear while they are bonded to both sides of the sample. These new failure mechanisms should increase the fatigue resistance, helping to explain the higher fatigue resistance observed by Sancaktar [19] on the supported adhesive. However, for the adhesive system under investigation, the effect of the reduced bonded area is probably counterbalanced by the effect of the new failure mechanisms added by the carrier presence, resulting in similar disbond growth rates (Fig. A.4).

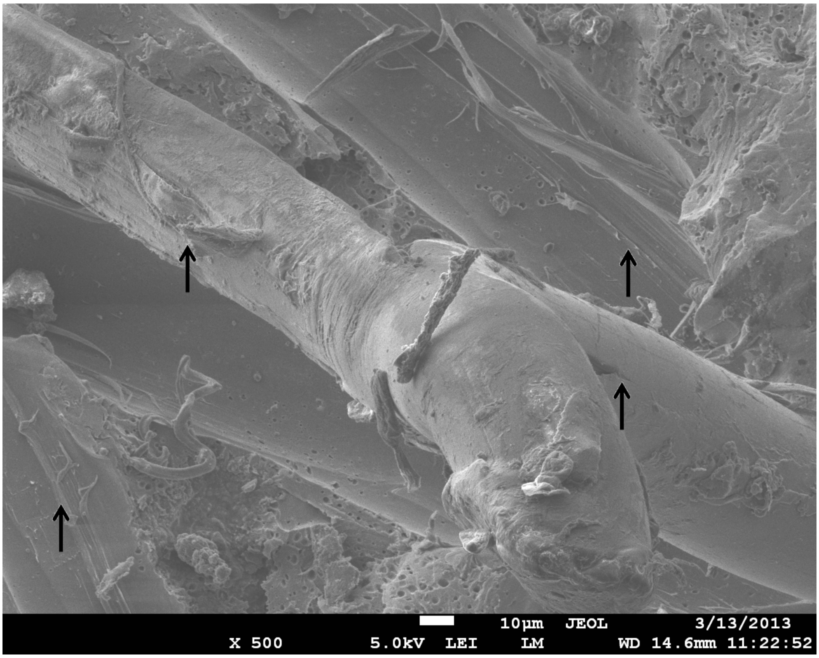

Figure A.6: *Carrier fiber failure - Arrows indicate cracks on the carrier fiber and parts of the fiber that were pulled apart..*

A.3.2 Mode II fracture behavior

Figure A.7 presents the fatigue results for Mode II loading. From these results one can conclude that for higher load amplitudes ($(\sqrt{G_{max}}-\sqrt{G_{min}})^2 > 800$N/m) the supported adhesive has a greater resistance to fatigue loading.

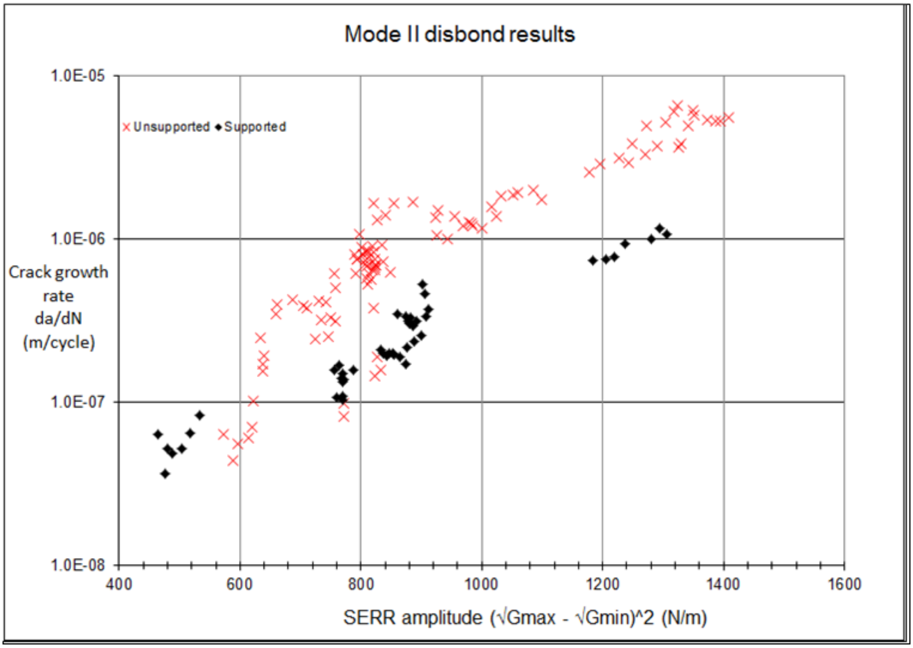

Figure A.7: *Fatigue disbond growth results - Mode II loading.*

Similarly to Mode I failure, Mode II disbond is characterized by the coalescence of micro cracks ahead of the crack tip. The main difference is the plane in which the micro cracks initiate. While for Mode I they initiate parallel to the bond line, for Mode II the micro cracks grow in planes inclined 45^o from the bond line plane. These inclined planes can be found by resolving the principal stresses on the adhesive [27]. Under static loading the inclined planes can coalesce forming cusps and under fatigue loading they can form rollers [28]. In addition, vertical cracks can also be observed [26].

The fracture surfaces are presented in Fig. A.8 and rollers and vertical cracks can be observed in both supported and unsupported adhesives. So, the carrier does not seem to affect the mechanism proposed for the rollers and vertical cracks formation (Fig. A.9) [26].

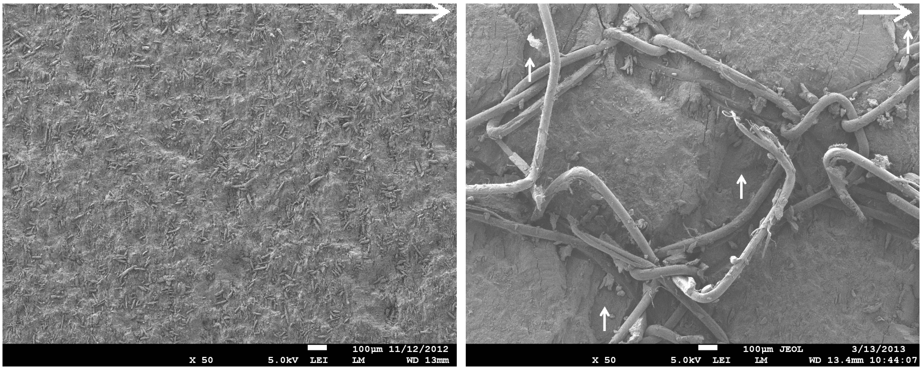

(a) Unsupported 50x

(b) Supported 50x White arrows indicate crack jumps.

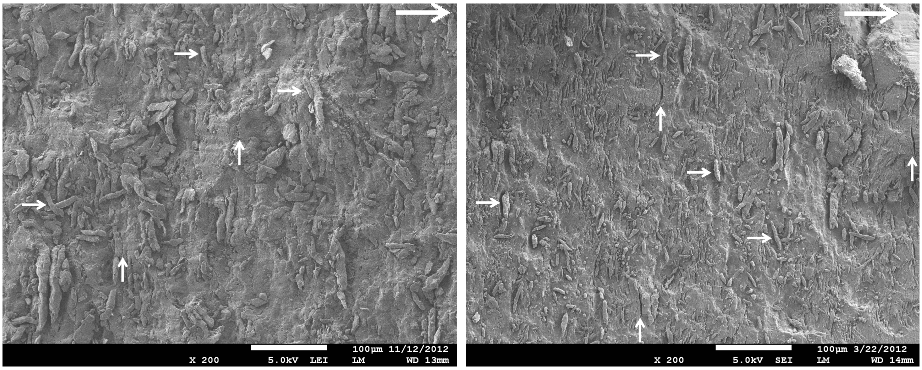

(c) Unsupported 200x Vertical white arrows indicate vertical cracks and horizontal white arrows indicate rollers.

(d) Supported 200x Vertical white arrows indicate vertical cracks and horizontal white arrows indicate rollers.

Figure A.8: *Comparison between the Mode II fracture surfaces. Top right black arrows indicate the main disbond growth direction.*

However, the carrier may induce a new failure mechanism, as the observed crack jump. The shear stresses, produced by Mode II and MM loading, results in a principal stress that is inclined in relation to the adhesive plane. The micro-cracks are created and tend to extend in a direction perpendicular to principal stress [27]. So, in the presence of Mode II, the main crack deviates from the center of the adhesive layer, until it reaches a complex stress state close to the adherent, where the crack deviates and grows parallel to the adherent. Specifically, in a MMB test they extend in the upper right direction until they reach the vicinity of the upper adherend. In the post-mortem examination this results in a significant difference between the upper and lower adherend. One adherend (the lower in a MMB) has a thick layer of adhesive, and the other (the upper in a MMB) has a thin layer of adhesive [27]. Figure A.8(b) shows the lower surface of the sample and it exemplifies this feature. Most of the surface presented is covered by a thick layer of adhesive. However, when the main crack gets close to the carrier the crack jumps to the lower surface (Fig. A.11). At the lower surface the crack

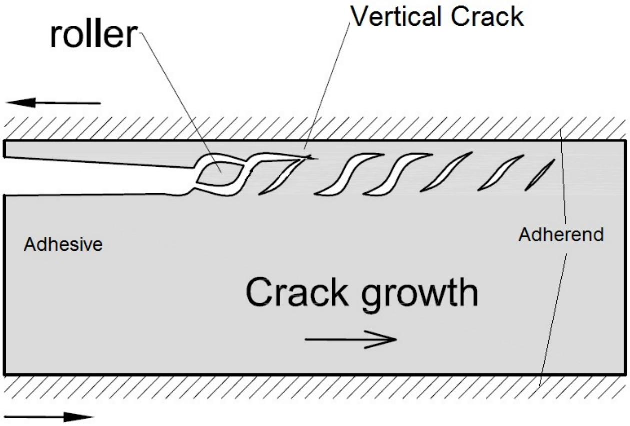

Figure A.9: *Roller and vertical cracks formation model for Mode II fatigue loading [26]. The shear stress produces tilted cracks close to the main crack. The main crack grow competes with the tilted crack grow, forming either rollers or vertical cracks.*

presents locally both Mode I and Mode II failure characteristics (Fig. A.10) but it is not possible to determine if the rollers were generated at that specific location or if they were generated in different areas and moved during the fatigue process. Consequently, the carrier is probably inducing Mode I locally, thus modifying the failure mechanism.

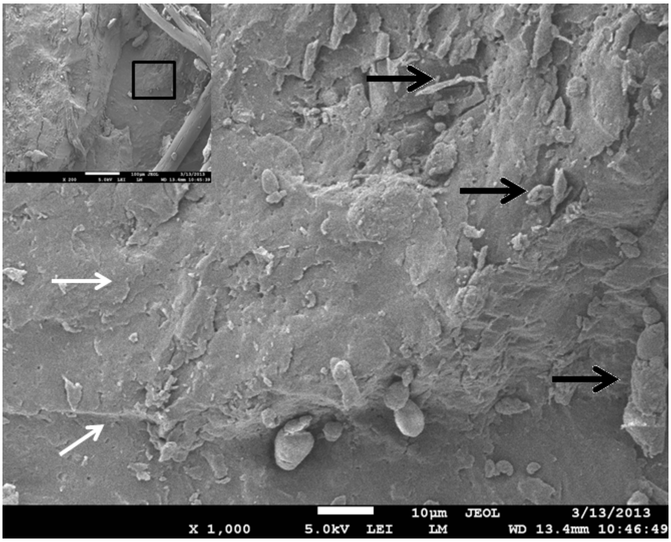

Figure A.10: *Crack jump detail. White arrows indicate local Mode I features and black arrows indicate local Mode II features.*

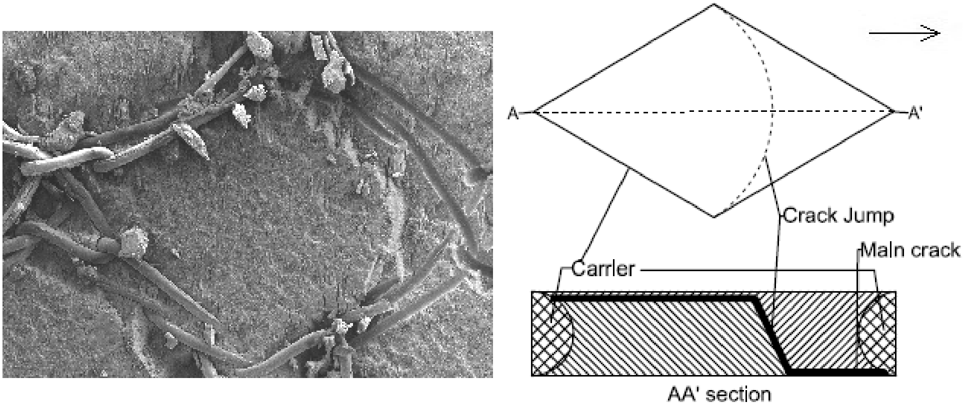

Figure A.11: *Crack jump Model - top right arrow indicates the main crack growth direction.*

This new failure mechanism helps to explain the difference in the fatigue disbond rate. At the crack jump, a larger area is created than it would be without the crack jump. So, the crack requires more energy, reducing the crack growth rate. Additionally, the carrier fibers are usually broken in Mode II (see Fig. A.8(b)). This indicates the fibers bear loads when the adhesive is subjected to Mode II loading, reducing the load applied on the adhesive and reducing the disbond growth rate.

A.3.3 Mixed-Mode fracture behavior

Figure A.12 presents the fatigue results for MM loading. As in Mode II, for higher loads the supported adhesive presents a higher resistance to fatigue loading.

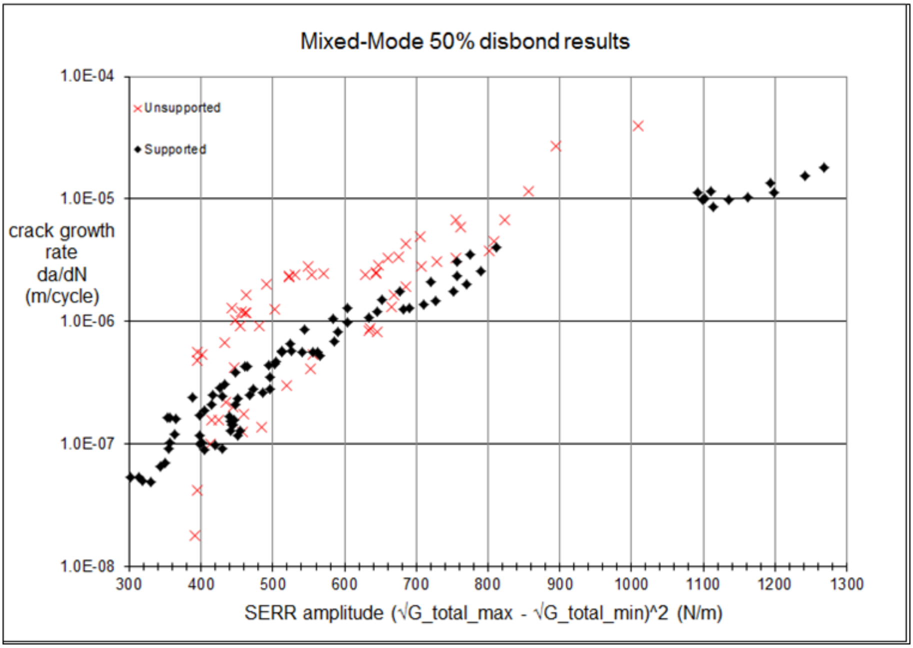

Figure A.12: *Fatigue disbond growth results - MM 50% loading.*

Mixed-Mode disbond is characterized by a mix of Mode I and Mode II features, the amount and the presence of each depending on the mode ratio [26]. The angle at which the micro cracks grow depends on the mode ratio and it varies from 0^o to 45^o. Close to 45^o (high Mode II) rollers and vertical cracks are expected and close to 0^o scarps and feather pattern are expected.

At a MM of 50%, the supported adhesive presents a fracture surface that is mostly similar to a Mode I fracture, with only a few rollers in an initial formation stage and some vertical cracks (Fig. A.13(d)). The crack jumps seen for Mode II were also observed in MM loading. Crack jumping occurred for all mode ratios evaluated (from 20% to 90%).

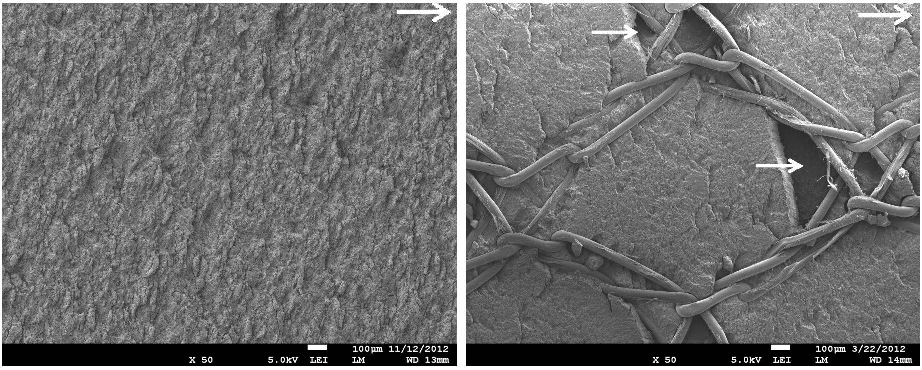

(a) Unsupported 50x

(b) Supported 50x White arrows indicate crack jumps.

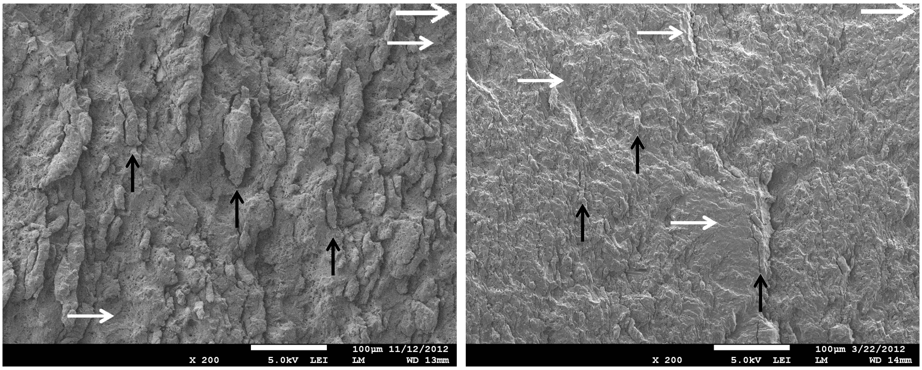

(c) Unsupported 200x White arrows indicate Mode I features and vertical black arrows indicate Mode II features.

(d) Supported 200x White arrows indicate Mode I features and vertical black arrows indicate Mode II features.

Figure A.13: *Comparison between the MM fracture surfaces. Top right black arrows indicate the main disbond growth direction.*

Apart from the presence of the crack jump, the unsupported adhesive surface presents another major difference from the supported one. The amount of rollers and vertical cracks is higher in the unsupported adhesive. This observation supports the hypothesis that the carrier bears Mode II loads. At a MM of 50% of Mode II the carrier supports a part of the Mode II load applied to the adhesive layer, resulting in a reduced Mode II component on the adhesive itself. This results in a smaller mode ratio observed by the adhesive itself than the mode ratio imposed to the sample, and it also explains the reduced amount of Mode II features in the supported adhesive.

A.4 Conclusions

This study investigated the effect of a nylon scrim cloth as a supporting system on Mode I, Mode II and Mixed-Mode fatigue failure properties of FM-94. The major conclusions are listed below.

- Under Mode I, the carrier did not show any significant influence on the disbond growth rate and on the fracture surface but a new failure mechanism - carrier fibers failure - was introduced;
- Under Mode II, the carrier reduced the disbond growth rate by introducing two failure mechanisms, the crack jump and carrier fiber failure;
- Under Mode II, the carrier bears part of the load, reducing the load applied to the adhesive and reducing the crack growth rate;
- Under Mixed-Mode, the carrier reduced the disbond growth rate and the fracture surface presented the same new failure mechanisms observed in supported Mode II sample;
- Under Mixed-Mode, the carrier bears part of the Mode II loading, reducing the mode ratio and the load applied on the adhesive itself.

Therefore, additionally to the thickness control, the presence of the carrier has a positive influence in bonded joints under fatigue loading as it either improves or doesn't modify the fatigue disbond growth properties of a metal-to-metal bonded interface.

Acknowledgement
The work presented in this paper was sponsored by the Netherlands Organization for Scientific Research (NWO) and Technical Science Foundation (STW) under the Innovational Research Incentives Scheme Veni grant.

References

[1] D. Bürger, C. D. Rans, and R. Benedictus. Influence of fabric carrier on the fatigue disbond behavior of metal-to-metal bonded interfaces. *The Journal of Adhesion*, 90(5-6):482–495, 2014.

[2] M. Fernando, W.W. Harjoprayitno, and A.J.Kinloch. A fracture mechanics study of the influence of moisture on the fatigue behaviour of adhesively bonded aluminium-alloy joints. *International Journal of Adhesion & Adhesives*, 16(2):113–119, 1996.

[3] H. Chai. Shear fracture. *International Journal of Fracture*, 37(2):137–159, 1988.

[4] D.L. Hunston, A.J. Kinloch, and S.S. Wang. Micromechanics of fracture in structural adhesive bonds. *Journal of Adhesion*, 28(2-3):103–114, 1989.

[5] H. Chai. Deformation and fracture of particulate epoxy in adhesive bonds. *Acta Metallurgica Et Materialia*, 43(1):163–172, 1995.

[6] L. F. M. da Silva, T. N. S. S. Rodrigues, M. A. V. Figueiredo, M. F. S. F. de Moura, and J. A. G. Chousal. Effect of adhesive type and thickness on the lap shear strength. *Journal of Adhesion*, 82(11):1091–1115, 2006.

[7] M. Hojo, T. Ando, M. Tanaka, T. Adachi, S. Ochiai, and Y. Endo. Modes I and II interlaminar fracture toughness and fatigue delamination of CF/epoxy laminates with self-same epoxy interleaf. *International Journal of Fatigue*, 28(10):1154–1165, 2006.

[8] L. F. M. Da Silva, F. A. C. R. G. De Magalhães, F. J. P. Chaves, and M. F. S. F. De Moura. Mode II fracture toughness of a brittle and a ductile adhesive as a function of the adhesive thickness. *Journal of Adhesion*, 86(9):889–903, 2010.

[9] S. Marzi, A. Biel, and U. Stigh. On experimental methods to investigate the effect of layer thickness on fracture behavior of adhesively bonded joints. *International Journal of Adhesion & Adhesives*, 31(8):840–850, 2011.

[10] T.T. Khoo and H. Kim. Effect of bondline thickness on mixed-mode fracture of adhesively bonded joints. *Journal of Adhesion*, 87(10):989–1019, 2011.

[11] T.A. Hafiz, M.M. Abdel-Wahab, A.D. Crocombe, and P.A. Smith. Mixed-mode fatigue crack growth in FM73 bonded joints. *International Journal of Adhesion and Adhesives*, 40(0):188 – 196, 2013.

[12] S. Zheng and I. A. Ashcroft. A depth sensing indentation study of the hardness and modulus of adhesives. *International Journal of Adhesion and Adhesives*, 25(1):67–76, 2005.

[13] L. M. Butkus, P. D. Mathern, and W. S. Johnson. Tensile properties and plane-stress fracture toughness of thin film aerospace adhesives. *Journal of Adhesion*, 66(1-4):251–273, 1998.

[14] L. F. M. Da Silva and R. D. Adams. Measurement of the mechanical properties of structural adhesives in tension and shear over a wide range of temperatures. *Journal of Adhesion Science and Technology*, 19(2):109–141, 2005.

[15] E. Sancaktar, H. Jozavi, and R. M. Klein. Effects of cure temperature and time on the bulk tensile properties of a structural adhesive. *Journal of Adhesion*, 15(3-4):241–264, 1983.

[16] D. G. Dixon, W. Unger, M. Naylor, P. Dublineau, and C. C. Figgures. Physical modifications for improved peel strength in a high-temperature epoxy adhesive. *International Journal of Adhesion and Adhesives*, 18(2):125–130, 1998.

[17] C. Gouri, R. Ramaswamy, and K. N. Ninan. Studies on the adhesive properties of solid elastomer-modified novolac epoxy resin. *International Journal of Adhesion and Adhesives*, 20(4):305–314, 2000.

[18] L. F. M. Da Silva, R. D. Adams, and M. Gibbs. Manufacture of adhesive joints and bulk specimens with high-temperature adhesives. *International Journal of Adhesion and Adhesives*, 24(1):69–83, 2004.

[19] E. Sancaktar. Fracture aspects of adhesive joints: material, fatigue, interphase, and stress concentration considerations. *Journal of Adhesion Science and Technology*, 9(2):119–147, 1995.

[20] D. A. Jablonski. Fatigue crack growth in structural adhesives. *Journal of Adhesion*, 11(2):125–143, 1980.

[21] Cytec Engineered Materials. *FM 94 Adhesive Film - Technical Data Sheet*, 2010.

[22] Standard test method for mixed Mode I-Mode II interlaminar fracture toughness of unidirectional fiber reinforced polymer matrix composites, 2006.

[23] Standard test method for Mode I interlaminar fracture toughness of unidirectional fiber-reinforced polymer matrix composites, 2007.

[24] Standard test method for measurement of fatigue crack growth rates, 2000.

[25] C.D. Rans, R. Alderliesten, and R. Benedictus. Misinterpreting the results: How similitude can improve our understanding of fatigue delamination growth. *Composites Science and Technology*, 71(2):230–238, 2011.

[26] D. Bürger, C. D. Rans, and R. Benedictus. Characterization of mixed-mode fatigue failure on metallic bonded joints. In *ICAF 2013 Symposium - Proceedings of the 27th Symposium of the International Committee on Aeronautical Fatigue*, pages 751–760, 2013.

[27] S. Singh and E. Greenhalgh. Micromechanics of interlaminar fracture in carbon fibre reinforced plastics at multidirectional ply interfaces under static and cyclic loading. *Plastics, Rubber and Composites Processing and Applications*, 27(5):220–226, 1998.

[28] F. Heutling, H. E. Franz, and K. Friedrich. Microfractographic analysis of delamination growth in fatigue loaded - carbon fibre/thermosetting matrix composites. *Materialwissenschaft und Werkstofftechnik*, 29(5):239–253, 1998.

B Paris relation coefficients and confidence interval calculations

B.1 Determining the coefficient C with a fixed m for the Paris Relation

As developed in Chap. 3, in order to find the parameters of a function that will fit experimental data a parameter must be minimized, usually the sum of the squared errors. So, for a linear function ($f(x) = a.x + b$), where the a is fixed:

$$R = \sum_n [(y_i - f(x_i))^2] = \sum_n [(y_i - (a.x_i + b))^2] \tag{B.1}$$

So, the minimum R is obtained when:

$$\frac{\partial R}{\partial b} = 0 \tag{B.2}$$

$$\frac{\partial R}{\partial b} = \sum_n -2.[y_i - a.x_i - b] = 0 \tag{B.3}$$

$$\sum_n y_i - a.\sum_n x_i - \sum_n b = 0 \tag{B.4}$$

$$b = \frac{\sum_n y_i - a.\sum_n x_i}{n} \tag{B.5}$$

Similarly, for a power function with a fix m:

$$R = \sum_n [(y_i - f(x_i))^2] = \sum_n [(y_i - C.x_i^m)^2] \tag{B.6}$$

$$\frac{\partial R}{\partial C} = \sum_{n} -2.x_i^m.[(y_i - C.x_i^m)] = 0 \tag{B.7}$$

$$\sum_{n} x_i^m.y_i - \sum_{n} C.x_i^m.x_i^m = 0 \tag{B.8}$$

$$C = \frac{\sum_n x_i^m.y_i}{\sum_n x_i^{2.m}} \tag{B.9}$$

B.2 Prediction interval of a new of a future experimental point with a fixed *m*

In order to obtain the prediction intervals in these work, one must first linearize the experimental values for fatigue crack growth, i.e., apply the log. So, the experimental points can be approximate by a linear regression. The prediction interval of a new experimental point (y_0) can be determined in a linear regression by [1]:

$$\hat{y_0} - \Delta \leq y_0 \leq \hat{y_0} + \Delta \tag{B.10}$$

Where $\hat{y_0}$ is the expected value from the regression analysis, $\hat{y_0} = f(x_0) = a.x_0 + b$, and Δ is defined by the function:

$$\Delta = t_{\alpha/2,n-2}\sqrt{MS_{Res}.\left(1 + \frac{1}{n} + \frac{(x_0 - \bar{x})^2}{S_{xx}}\right)} \tag{B.11}$$

α is the confidence interval, n is the number of experimental points, $t_{\alpha/2,n-2}$ is the percentage point of the t-Distribution, $\bar{x}$ is the average value of the experimental points x_i, and S_{xx} and MS_{Res} are given by:

$$S_{xx} = \sum_{n}(x_i^2) - \left(\sum_{n} x_i\right)^2/n \tag{B.12}$$

$$MS_{Res} = \frac{\sum_n (y_i - f(x_i))^2}{n-2} \tag{B.13}$$

In a case where one of the coefficients is fixed, e.g. the slope (a), the degree of freedom is reduced from 2 to 1, so, Eq. B.11 and B.13 must be adjusted as:

$$\Delta = t_{\alpha/2,n-1}\sqrt{MS_{Res}.\left(1 + \frac{1}{n} + \frac{(x_0 - \bar{x})^2}{S_{xx}}\right)} \tag{B.14}$$

$$MS_{Res} = \frac{\sum_n (y_i - f(x_i))^2}{n-1} \tag{B.15}$$

The use of Eq. B.10 gives an interval for an expected y_0 for an input x_0. If one applies this equation to a range of x values, one would obtain two curves that limit the range of expected values for y. Figure B.1 presents an example of the use of this method. The data used in this example refer to the MR=50% from Chap. 3.

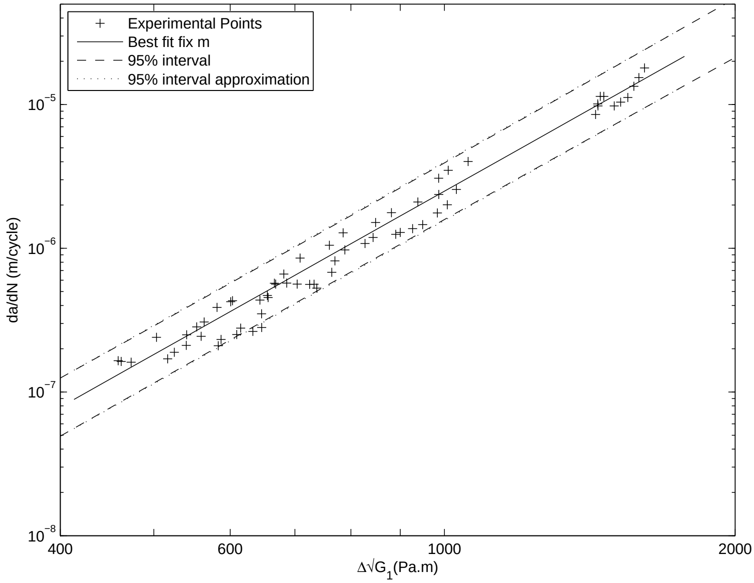

Figure B.1: *Fatigue crack growth behavior as a function of principal stress.*

The limits of the 95% interval can not be represented as a straight line in a graph log-log, i.e., the function describing the interval is not a power function. However, it can be approximated by a power function. If one fix the exponent of the power function, to the same value as the one used to fit the data, a maximum and a minimum value of C can be obtained.

References

[1] D.C. Montgomery, E.A. Peck, and G.G. Vining. *Introduction to linear regression analysis.* Wiley series in probability and statistics: Texts, references, and pocketbooks section. Wiley, 2001.

C Fatigue disbond growth predictions for the SLJ specimens

This appendix presents the fatigue disbond growth (FDG) predictions for the remaining specimens presented in Chapter 6.

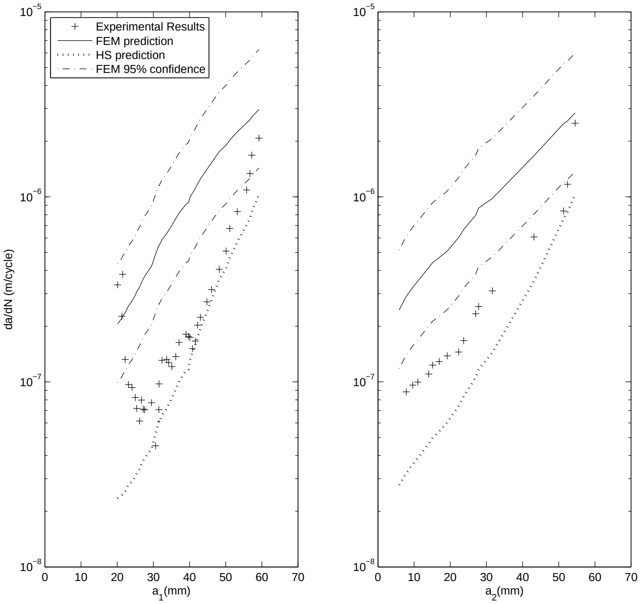

Figure C.1: *FDG prediction for both disbond tips of a SLJ - specimen 1.*

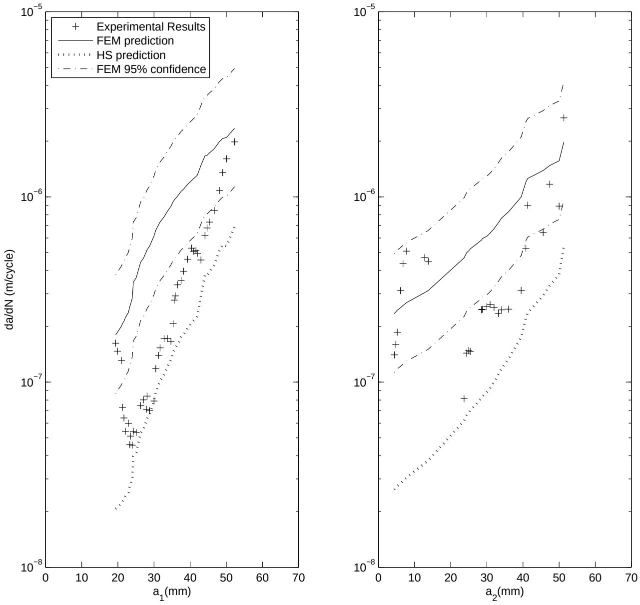

Figure C.2: *FDG prediction for both disbond tips of a SLJ - specimen 3.*

Acknowledgments

And finally the journey has come to an end. After several good and some challenging moments, now is an opportune time to express the appreciation for those who shared this journey with me.

First of all, I would like to thank my supervisors: Rinze Benedictus and Calvin Rans. Pursuing a Ph.D. at TU Delft has many challenges. And they made the challenges at times look trivial, and other times worth achieving. Thank you both for trusting and helping me during this period. Along with them, I would also like to thanks René, Marcias and Sofia for the helpful discussions and ideas to improve this work.

As a researcher, I was financially supported by the Brazilian Air Force. Thus, I would like to thank Col. Alberto Walter da Silva Mello Jr.

A special thank should be extended to Gemma. She was always efficient in keeping the non-research related problems away from the Ph.D. students. Her efficiency in achieving it is commendable. She was always solving the problems so quickly that we didn't even noticed them.

As this was an experimental research, I depended a lot on the lab staff. For their support in helping set up the machines and coupons, for the lessons on how to do it and how to do it better, I would like to thank Bob, Berthil, Hans, Frans, Kees, Ed, Johan and the others.

Arriving in a foreign country, surrounded by a different culture, can be challenging. I would like to thank my office mates, Maria Luiza, Freddie, Gustavo, Wandong and Nikos, for smoothing this experience. A special thank also goes to the former and current TU Delft colleagues: Bea, Eduardo, Konstantin, Marcelo, Mayank, Greg W., Greg R., Cory, Patricio, Ilham, Fabrício, John-Alan, Riccardo, Milan, Marw, Freek, Adrian L., Adrian F., Maria, Huajie, Lucas, Nick, FX, Helena, Ilias, Yao, Marcos, Derek, Jaret, Hari, Niels and Tian. And also the friends that made my life easy and made me felt at home: Alejandra, Elta, Germana, Bianca, Marie, Daniel, Eduardo, Jairo, Debora, Aline, Antonia, Romain, Rafael and Juliana. Without you this experience would have been worse, there would be no light or fun.

Last, but certainly not least, I would like to thank my family for their support.

About the author

Daniel Bürger

The Author was born on the 6th of September 1982 in Jaraguá do Sul - Santa Catarina state, Brazil. He graduated from high school at Escola Preparatória de Cadetes do Ar, Barbacena, in 2000. Later, he moved to São José dos Campos, where he obtained a Bachelor in Aeronautical Engineering degree in 2006 at Instituto Tecnológico de Aeronáutica (ITA) and was commissioned as an officer in the Brazilian Air Force (FAB) in December 2006. In January 2010 he completed his Master of Science degree in Mechanical and Aeronautical engineering at ITA with a dissertation entitled “Ballistic impact simulation on ceramic/composite armor”. In October 2010 he moved to TU Delft as a FAB-sponsored Ph.D. student under the supervision of Prof. Dr. ir. R. Benedictus as promoter and Dr. C. D. Rans as daily supervisor.

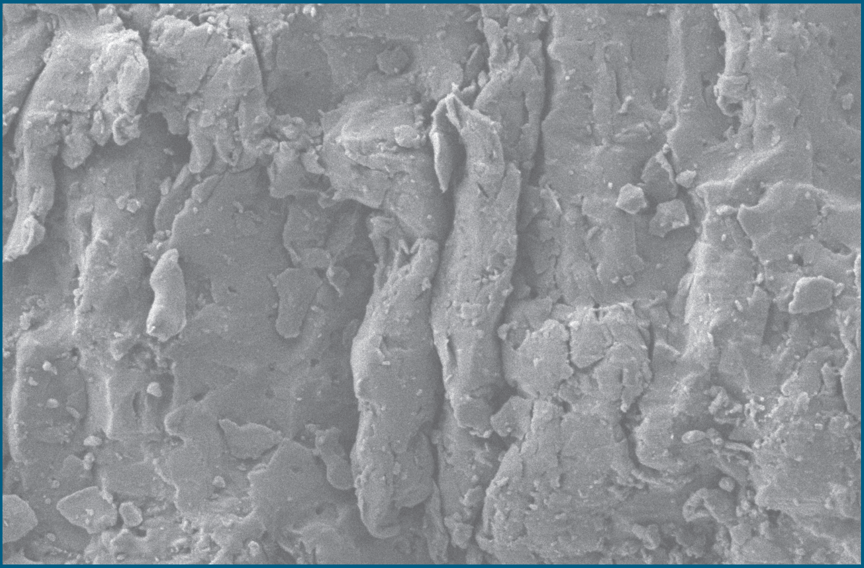

Engineers are increasingly attempting to reduce the weight of aerospace structures. More efficient materials and joining techniques can offer a similar performance for a lighter structure. In this scenario, adhesively bonded metallic parts can significantly improve the fatigue behavior of the joint over mechanical fasteners.

This research seeks to contribute to the knowledge on Mixed-Mode fatigue disbond failure mechanisms and, based on the mechanisms identified, develop a model to predict fatigue disbond.

Delft University of Technology